

USING REMOTE SENSING AND GEOGRAPHIC INFORMATION SYSTEMS FOR  
FLOOD VULNERABILITY MAPPING OF THE C-111 BASIN IN SOUTH MIAMI-  
DADE COUNTY

By

WILLIAM ANDREW WEBB

A THESIS PRESENTED TO THE GRADUATE SCHOOL OF THE UNIVERSITY OF  
FLORIDA IN PARTIAL FULFILLMENT FOR THE REQUIREMENTS FOR THE  
DEGREE OF MASTER OF SCIENCE

UNIVERSITY OF FLORIDA

2006

Copyright 2006

by

William Andrew Webb

This paper is dedicated to my parents Frank R. Webb and Brenda Y. Webb.

## ACKNOWLEDGMENTS

I would like to acknowledge my department professors Dr. Wendy Graham, Dr. Carol Lehtola and Dr. Jack Jordan for their guidance and hard work in this project. I would like to thank Dr. Clint Slatton for providing his expertise in Airborne Laser Swath Mapping. I would like to thank Don Pybas for his contribution and cooperation. I would like to thank Charles Brown for his assistance during the development process.

## TABLE OF CONTENTS

	<u>page</u>
ACKNOWLEDGMENTS .....	iv
LIST OF TABLES .....	vii
LIST OF FIGURES .....	ix
GLOSSARY OF TERMS .....	xii
ABSTRACT .....	xv
CHAPTER	
1 INTRODUCTION .....	1
Background .....	1
Flood Management .....	1
Objectives .....	3
Project Area .....	4
2 LITERATURE REVIEW .....	7
Active and Passive Remote Sensing .....	7
Spectral Signature of Water .....	8
Sensor Performance .....	9
Normalized Differential Vegetation Index (NDVI) .....	10
Water Detection .....	11
Cloud Detection .....	12
Airborne Laser Swath Mapping .....	13
ALSM Accuracy .....	15
ALSM Point Removal .....	16
ALSM Applications .....	18
Geographic Information Systems .....	20
Spatial Modeling .....	21
Inundation Mapping with GIS .....	24
3 DATA RESOURCES AND METHODOLOGY .....	26

Introduction.....	26
Surface Water Data.....	26
Digital Elevation Model Construction.....	27
Landsat 7 Enhanced Thematic Mapper .....	28
Vegetative Index Methodology .....	28
Unsupervised Classification .....	29
Bare Earth Modeling.....	30
Aerial Color Infrared Analysis .....	31
Ground Control Point Analysis .....	32
Topographic Spatial Modeling.....	34
Surface Water Elevation Map Methodology .....	35
Surface Water Elevation Map Interpolation.....	37
Surface Water Inundation Map Methodology.....	39
4 RESULTS AND DISCUSSION.....	49
Cloud Detection.....	49
Vegetation Index Two and Vegetation Index Three.....	51
NDVI .....	55
Topographic Analysis.....	60
Classified ALSM DEM .....	61
Surface Water Elevation Map Analysis.....	68
Surface Water Inundation Map.....	93
5 CONCLUSION.....	114
Image Analysis .....	114
Bare Earth Modeling.....	114
SWEM .....	115
SWIM .....	115
Conclusion.....	116
6 RECOMMENDATIONS FOR FUTURE STUDIES.....	117
LIST OF REFERENCES.....	119
BIOGRAPHICAL SKETCH .....	123

## LIST OF TABLES

<u>Table</u>	<u>page</u>
2.1 Specifications of a commercial Lidar system. ....	13
3.1 Area 2 static GPS points. ....	39
3.2 Inverse distance weighting search parameters for topography. ....	40
3.3 Global polynomial search parameters for topography. ....	41
3.4 Local polynomial search parameters for topography. ....	41
3.5 Radial based function search parameters for topography. ....	41
3.6 Kriging search parameters for topography. ....	42
3.7 Projection Parameters for ALSM. ....	42
3.8 Universal kriging search parameters for SWEM. ....	43
3.9 Simple kriging search parameters for SWEM. ....	44
3.10 Ordinary Kriging search parameters for SWEM. ....	45
3.11 Disjunctive kriging search parameters for SWEM. ....	47
3.12 Universal Kriging for SWEM. ....	48
4.1 Radial based functions statistics for topography. ....	106
4.2 Inverse distance weighting statistics for topography. ....	106
4.3 Global polynomial statistics for topography. ....	107
4.4 Local polynomial statistics for topography. ....	107
4.5 Kriging statistics for topography. ....	108
4.6 Universal Kriging statistics for SWEM. ....	108
4.7 Universal kriging statistics for SWEM, 10/12-22/1999. ....	108

4.8 Simple kriging statistics for SWEM, 10/12-22/1999.....	109
4.9 Ordinary kriging statistics for SWEM.....	109
4.10 Disjunctive Kriging statistics for SWEM.....	111
4.11 SWEM surface water values for October 12-22, 1999.....	112
4.12 Vulnerability index classes used for SWIM.....	113
4.13 Calculated inundation statistics for the study area.....	113

## LIST OF FIGURES

<u>Figure</u>	<u>page</u>
1.1 Map of Miami-Dade County and the project area. ....	4
1.2 Map of the study area.....	5
2.1 Illustration of a Lidar infrared beam.....	14
3.1 Color infrared aerial photos of the study area.....	33
3.2 Map of measurement sites. ....	36
4.1 Map of the Frog Pond with Band 8.....	50
4.2 Vegetation index two map of south Florida, October 16, 1999.....	52
4.3 Vegetation index two map of the study area, October 16, 1999.....	54
4.4. October 16, 1999, NDVI map of the south Florida. ....	56
4.5. October 16, 1999, NDVI map of the study area. ....	58
4.6 Planar view of the NAD 27 study area DEM. ....	62
4.7 Graph of surface water elevation values.....	70
4.8 SWEM.....	71
4.9 Prediction error for SWEM.....	82
4.10 SWIM.....	95

## GLOSSARY OF TERMS

ACIR	Aerial Color Infrared	ACIR is aerial color infrared imagery that is not referenced with a coordinate system.
ALSM	Airborne Laser Swath Mapping	ALSM is a mapping technology that uses a laser to map land or bathymetric topography.
BEM	Bare earth model	A bare earth model is a DEM with artifact or unwanted points removed.
DEM	Digital Elevation Model	A DEM is a 3D representation of a surface than may be represented with raster cells or a TIN.
	Deterministic Interpolation	Deterministic interpolation uses deterministic functions to predict values of a spatially distributed field at unmeasured locations.
DOQQ	Digital Orthographic Quarter Quadrangle	A DOQQ is similar to an aerial photograph except it is referenced with a coordinate system and is used for general GIS mapping applications.
DSM	Digital Surface Model	A DSM is a 3D representation of a surface with objects and man made features removed.
DTM	Digital Terrain Model	A DTM is a 3D representation of a surface that uses a TIN to connect points.
FEMA	Federal Emergency Management Agency	FEMA is the disaster management and relief agency of the federal government.
GIS	Geographic Information Systems	GIS is software that captures, stores, retrieves, manipulates and displays geographically referenced spatial tabular data.

Glossary of terms continued

GPS	Global Positioning Systems	GPS is a constellation of 24 satellites that provides latitudinal and longitudinal data collected by a receiver.
	Kriging	Kriging is geostatistical interpolation technique that uses the spatial correlation of a distributed field to predict its value of unmeasured locations.
Landsat 7 ETM+	Landsat 7 Enhanced Thematic Mapper	Landsat 7 ETM + is the seventh USGS satellite in a series of satellites designed to capture environmental data with visible, near infrared, mid-infrared, low and high gain thermal sensor bands.
Lidar	Light Detection and Ranging	Light Detection and Ranging is the enabling laser technology used for ALSM flight operations.
NAD 83	North American Datum 1983	NAD 83 is the current horizontal datum used by the National Geodetic Survey.
NAD 27	North American Datum 1927	NAD 27 is the predecessor horizontal datum to NAD 83.
NDVI	Normalized Differential Vegetation Index	NDVI is a vegetative index that is calculated as the difference between the red and near infrared bands divided by the sum of the red and near infrared bands.
NGVD 29	National Geodetic Vertical Datum 1929	NGVD 29 is the predecessor vertical datum to NGVD 88.
NGVD 88	National Geodetic Vertical Datum 1988	NGVD 88 is the current vertical datum used by the National Geodetic Survey.
NPS	National Park Service	The National Park Service is controlled by the U.S. Department of Interior and is responsible for the management of all national parks.
	Raster	A raster is a thematic map layer represented with a grid.
	Remote Sensing	Remote sensing refers to the capture of data without a physical collection of the data.

Glossary of terms continued

SCDS	South Dade Conveyance System	The SDCS is the southern extension of the Central and Southern Flood Control Project and is located in south Miami-Dade County.
SFWMD	South Florida Water Management District	The SFWMD is one of five water management districts in Florida, and its district authority covers all of southeast Florida.
SWEM	Surface Water Elevation map	The Surface Water Elevation Map is a representation of the surface water for elevation over project areas of interest.
SWIM	Surface Water Inundation Map	The Surface Water Inundation Map is a representation of the surface water elevation measured in elevation above mean sea level with respect to NGVD 88. The Surface Water Inundation Map is the result of subtracting land surface elevation grids from surface water elevation, and represents depth of water on the land surface.
TIN	Triangulated Irregular Network	A TIN is a three dimensional representation of a surface created by using triangles to link points.
USGS	U.S. Geological Survey	The USGS is a multi-disciplinary science organization that studies biology, geography, geology, geospatial information, and water.
	Vector	Vector is a thematic map layer represented by points, lines and polygons.
VI2	Vegetative Index Two	Vegetative Index Two is calculated as the product of the green band and low gain thermal band divided by the high gain thermal band.
VI3	Vegetative Index Three	Vegetative Index Three is calculated as the low gain thermal band divided by the sum of the mid-infrared and red bands.

Abstract of Thesis Presented to the Graduate School  
of the University of Florida in Partial Fulfillment of the  
Requirements for the Degree of Master of Science

USING REMOTE SENSING AND GEOGRAPHIC INFORMATION SYSTEMS FOR  
FLOOD VULNERABILITY MAPPING OF THE C-111 BASIN IN SOUTH MIAMI-  
DADE COUNTY

By

William Andrew Webb

May 2006

Chair: Wendy D. Graham

Major Department: Agricultural and Biological Engineering

The hydrologic cycle of south Florida frequently produces rain events that include thunderstorms, tropical depressions and hurricanes. During 1999-2000, south Miami-Dade was struck by two intense rain events that severely inundated local agricultural operations for over a week. In the final assessment, agricultural losses sustained from these storms totaled to nearly \$430 million.

Flood hazard mapping has traditionally relied on paper maps that display the flood extent with only polygon boundaries. Unfortunately, paper maps are greatly limited in use, because they fail to show the extent, magnitude and duration of flooding. Recent advances in airborne laser swath mapping, ALSM, and satellite sensor technology have provided alternative types of data needed to more accurately map flood vulnerability. The general scope of this project is to improve mapping flood vulnerability in the southern C-111 basin by combining a variety of remotely sensed data sets.

The procedure for mapping a severe flood condition following Hurricane Irene involved the combination of ALSM, Landsat7 ETM+ and Geographic Information Systems (GIS). Band 8, vegetation index two and vegetation index three derived from the Landsat 7 ETM+ image were useful for mapping cloud cover, and the normalized differential vegetation index (NDVI) was useful for mapping inundation produced by Hurricane Irene. The primary limitations of vegetation index maps include the 30 meter spatial resolution, and the obstruction of the spectral signature of water caused by vegetation and clouds. Project inundation maps created with regional surface water and airborne laser swath mapped (ALSM) data displayed the flood duration, magnitude and extent of the flood condition resulting from Hurricane Irene.

## CHAPTER 1 INTRODUCTION

### **Background**

For nearly a century, south Miami-Dade's subtropical climate has provided a suitable environment for consistent annual production of agricultural commodities. Agricultural production heavily depends upon the regional climate that is characterized by a high mean annual rainfall, warm temperatures and extremely mild winters. Hurricanes and tropical storms often produce flood conditions that can remain for weeks.

During 1999-2000, south Miami-Dade was struck by two intense rain events. The first event, Hurricane Irene, passed over South Florida on October 15, 1999 and the second event, the October 2000 No Name Event (NNE), struck almost one year later on October 4, 2000. The impact of both storms on the agricultural economy of south Miami-Dade resulted in losses of nearly \$430 million.

### **Flood Management**

Flood control for south Florida became a federal priority in 1947 after back-to-back hurricanes left most local communities and the newly created Everglades National Park (ENP) inundated for weeks. In 1948, Congress authorized construction of the Central and Southern Florida Flood Control Project (CS&F) to regulate flooding and mitigate damage. The current system contains 1,800 miles of canals, 25 major pumping stations and other conveyance structures that stretch from Orlando to south Miami-Dade.

The South Dade Conveyance System (SDCS) is the Miami-Dade County extension of the CS&F and is governed in a three party agreement between ENP, the United States

Army Corps of Engineers, and the South Florida Water Management District (South Florida Water Management District 2000). Canals C-111 and L31W provide flood relief for agricultural lands and discharge water into Taylor Slough and Florida Bay.

The frequency and magnitude of flood events in South Miami-Dade have increased the demand for high-resolution flood maps that are capable of displaying the extent, magnitude and duration of a specific flood event. In 1997, a University of Florida Hydrologic Sciences Task Force (HSTF) addressed the major issues surrounding flood management for agricultural areas in south Miami-Dade (Graham et al., 1997, pp.34),

Flooding in the agricultural area has intensified in frequency, duration and depth . . . the lack of documentation concerning the negative impact of the experimental water deliveries has hindered progress by the USACOE and SFWMD to address these concerns.

The hydrologic and geographic databases in the agricultural area east of the C-111 canal should be enhanced. Installation of additional monitoring stations, development of new geographic information, and further historical and statistical evaluations of the existing data bases is necessary to accurately assess the impact of canal operations on groundwater levels in the agricultural area.

A local-scale, event based hydrologic model is needed to define the risk of flooding to the agricultural community associated with alternative structural and operational plans for the C-111 project...such a model could be used to produce maps of flooding probability in the agricultural area associated with alternative structural and operational plans for the C-111 project, which would allow local producers to better plan for the future.”

The development of a multi-hazard database currently is the highest priority for the Department of Homeland Security and the Federal Emergency Management Agency, FEMA (Lowe 2002). FEMA’s Multi-Hazard Flood Map Modernization initiative involves the expansion of the current geo spatial hazard data base including the Multi-Hazard Flood Map Modernization. The modernization project is designed to produce a more accurate geospatial flood vulnerability database that is accessible to the general public. Furthermore, the National Flood Insurance Program has charged FEMA to head

the Coordination of Surveying, Mapping, and Related Spatial Data Activities. The action mandates that flood hazard mapping becomes FEMA's top priority among all natural disasters. Part of the effort additionally includes the initiative to acquire geo-referenced spatial data and micro-topographic Airborne Laser Swath Mapped data for advanced hydrologic models and maps. In 1999, FEMA and NASA sponsored ALSM flight operations of the C-111 basin and Everglades National Park, ENP, for future flood mapping projects. Modern FEMA flood maps are required to meet the standard of a 5 meter spatial resolution (Maune 2001).

Recently, FEMA and the Harris County Flood Control District developed the Tropical Storm Allison Recovery Project to assess flood vulnerability in response to the aftermath of tropical storm Allison ([www.hcfdc.org/tsarp.asp](http://www.hcfdc.org/tsarp.asp), April 2006). The project methodology featured the integration of ALSM and GIS for creating digital flood insurance rate maps, DFIRMS.

### **Objectives**

The research objective of this project was to develop a method for assessing flood vulnerability in the C-111 basin by integrating Landsat7 sensory data, regional surface water elevation data and airborne laser scanned topographic data. Secondary objectives included the creation of a bare earth model for agricultural fields, modeling regional surface water elevation prediction grids and detecting clouds with vegetative indices. The featured map product is the surface water inundation map (SWIM). SWIM is an inundation map capable of displaying the magnitude, duration and extent of flooding with a 3 meter spatial resolution. October 12-22, 1999, is the study period used for generating surface water grids and inundation maps.

## Project Area

The study area lies in the southern area of the C-111 basin and is comprised of agricultural fields and protected wetland areas in ENP, Figure 1.1. The Frog Pond is a fertile tract of land in the C-111 partitioned into twenty-two parcels and leased by the Federal government; however flood protection is not guaranteed for the Frog Pond. Parcels 14, 15, 16, 17, 18 and 19 are located within the study area; however only 16 and 18 are completely displayed, (see Figure 1-2).

The three major land cover types that dominate the study area are wetland forest, wetland marsh and agricultural row crop fields. Fiducial land features are permanent geomorphological features in the study area and they include the soil mound and the L-31W canal, Figure 1.2. The S175 culvert is also located on the L31W canal inside the study area.

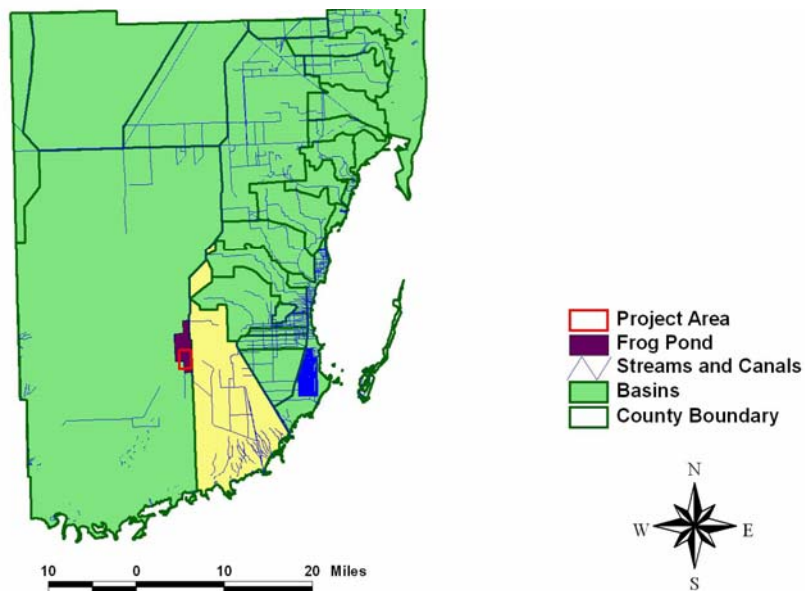


Figure 1.1 Map of Miami-Dade County and the project area.



Figure 1.2 Map of the study area. Leased parcels are numbered 14-21. The S175 culvert is represented with a red circle on the L31W canal.

The sub-surface hydrology of south Florida, including Miami-Dade, is characterized by an unconfined, highly permeable system called the Biscayne Aquifer (Fetter 1998). The Biscayne aquifer is recharged by precipitation, and water table levels fluctuate with the amount of precipitation. Below the Biscayne is a clastic semi-confining unit, the gray limestone aquifer and a lower clastic unit (Graham et al. 1997). Canals penetrate the most permeable part of the aquifer. The thickness and hydraulic conductivity of the Biscayne in the southern C-111 basin are approximately 46ft. and

25,000 ft. /day, respectively (Graham et al. 1997). Water levels in the Biscayne conform to the land surface with the highest levels occurring in the high elevation areas, and lowest levels in the low elevation areas.

## CHAPTER 2 LITERATURE REVIEW

Photogrammetry is the science of analyzing photographs and images to determine the size, shape, and spatial attributes of the features in an image acquired with remote sensing (Bethel and Cheng 1995). Remote sensing refers to the inferring of target or media characteristics by the reception of energy from the target or media. The energy may be electromagnetic, acoustic, subatomic particles, scattered energy originally transmitted from an active system sensor or originating from the sun.

### **Active and Passive Remote Sensing**

All remote sensing applications use either active or passive sensors. Passive remote sensing is usually dependent on reflected solar illumination or the emission or transmission of black body radiation. Active remote sensing involves sending a signal at a specific wavelength to the earth surface, detecting a return signal and assigning a pixel value to the received signal.

Emitted energy, an earth surface feature, is optimally sensed in the near infrared to the far infrared bands and reflectance properties are optimally sensed in the visible through the mid-infrared bands. For this reason, most passive sensor studies of planetary surfaces are conducted in the visible and infrared regions. Madden et al. (1998) used 1994 color infrared imagery to identify wetland vegetation in Everglades National Park. Doren, Rutchey and Welch (1998) used color infrared imagery to classify vegetation in the southern Everglades. Welch, Madden and Doren (1998) used color infrared imagery as ground control to classify vegetation in the Everglades.

The major applications of visible and infrared remote sensing include detecting surface chemical compositions, vegetative cover and biological processes. Although, visible and color infrared sensory data are useful for environmental studies, wave matter interactions produce noise in the received signal.

### **Spectral Signature of Water**

Variations in emitted and reflected radiation are used to measure, classify and verify the spectral signature characteristics of the land surface. Similar surfaces will share similar signature values within the electromagnetic spectrum for a specific wavelength, and different surfaces typically possess different spectral signatures. Scatter, emittance, reflectance and absorption of specific bands produce a unique “spectral signature” or curve that is characteristic for a particular surface property. The remotely sensed spectral signature is related to an associated curve obtained from laboratory measurements of wavelength versus reflectance for the visible and infrared regions of the electromagnetic spectrum for a library of materials.

Water has a low spectral signature reflectance in the visible and infrared region compared to all other major land cover types. Water, vegetation and exposed ground are the main ground cover types in the C-111, and the ability to recognize these ground cover types with remotely sensed images is dependent on separating and distinguishing their spectral characteristics. Water with sediment and debris will produce a higher reflectance spectral signature than that of pure water.

Albedo is the reflectivity of a surface, and water possesses a low albedo in the near infrared band. Vegetation possesses a high reflectance in the infrared spectrum due to plant microstructure. Vegetation has a relatively low reflectance in the red band compared with soil and turbid water, while wet soil and water have similar reflectance in

the red band. The ratio of red and infrared bands is used to distinguish between water (pure and turbid) and land (vegetation and soil).

Because of sediment and debris, flood water will produce a maximum reflectance peak in the red band. This signature is particularly useful for flood detection; however, the presence of dense clouds may interfere with the signature of the land surface. No verifiable method can be expected to eliminate cloud contamination to obtain visible and near infrared based flood information under thick cloud formation, (Sheng, Su and Xiao 1998).

Active and passive signal errors are primarily attributed to absorption or scatter of atmospheric noise components. Absorption is caused by the presence of water vapor and gases, while scatter is caused by the presence of vapor, gases, dust and atmospheric turbulence.

### **Sensor Performance**

Four measures of sensor performance are used for determining the quality of the resolution of an image. These measures include spectral resolution, spatial resolution, radiometric resolution and temporal resolution.

Spectral resolution refers to the specific wavelength intervals in the electromagnetic spectrum that the sensor records. A decrease in the wavelength interval results in an increase in the resolution of the image.

Spatial resolution is the measure of the smallest feature that a sensor can detect or the area on the ground represented by each pixel for a nadir view. Nadir is the point diametrically opposed to the zenith, which is the point in the sky directly overhead. An azimuth is an arc from the horizon to the zenith. Nadir can also be taken to mean "lowest point" in the sense that zenith can be taken to mean "highest point."

Spatial resolution can also be described in the form of the instantaneous field of view (IFOV) or the measure of the cone angle (radius) viewed by a single detector at a specific point in time. The scale at which an image is captured provides useful information about spatial resolution, and spatial resolution may vary for different sensory bands in an image. For example, the panchromatic band of Landsat 7 possesses a 15 meter spatial resolution while the other bands possess a 30 meter resolution. Objects that are smaller than the IFOV can be detected if they contrast strongly against the background of surrounding pixels. Conversely, objects larger than the pixel may not be detected if their reflectance does not dominate the surrounding pixels.

Radiometric resolution or dynamic range is the number of possible data values in each band or the number of bits into which the remotely sensed energy is divided. For example, when the Landsat7 ETM+ sensor records the electromagnetic radiation in its IFOV, the total intensity of the energy is divided into 256 brightness values for 8 bit data. Data file values or digital numbers for 8 bit data range from 0 to 255 for each pixel.

Temporal resolution is a measure of how often the sensor records imagery for a particular area, and for satellites, this is generally defined by its path or orbital cycle.

### **Normalized Differential Vegetation Index (NDVI)**

Vegetation indices are created by combining data from sensor bands into a specified algorithm. They are particularly useful for identifying features by enhancing certain reflectance properties. NDVI is commonly used to visualize properties of land cover that are elusive with only raw band imagery.

NDVI is most useful for mapping land cover including urban areas, water, soils, dying and healthy vegetation. A value near 1 represents high near infrared reflectivity and a value near -1 indicates strong near infrared absorption. NDVI is calculated as the

difference between near infrared and red divided by the sum of red and near infrared.

Melesse and Jordan (2003) calculated NDVI as

$$NDVI = \frac{Band4 - Band3}{Band4 + Band3} \quad (1)$$

Todd and Hoffer (1998) used mid-infrared with Landsat 5 near infrared data to map land surface moisture. NDVI increased with an increase in healthy vegetative cover. Inundated surfaces possess extremely low NDVI values, because of high infrared absorption and low infrared reflectance properties. The study investigated NDVI for targets with specific vegetation cover amounts and varying soil backgrounds. Although vegetation indices were less sensitive to soil background, they were effective for determining vegetation biomass and vegetation cover for small areas. The relationship between NDVI and vegetative land cover showed that NDVI was higher for moist soils than the drier soils at the same percent vegetation. NDVI increased substantially as moisture increased for the same vegetation cover.

### **Water Detection**

Lunetta and Balog (1999) used multi temporal Landsat 5 data for identifying wetland land cover including water bodies. The results showed that sensor data in the mid-infrared, Band 5, best discriminated between dry and wet areas. Frazier and Page (2000) successfully used visible and infrared bands from Landsat 5 to detect water bodies in the floodplain of the Murrumbidgee River in central Australia.

Song, Duanjun and Wesely (2003) researched the short wave spectral signature of water bodies. The signature of water is unique among signatures for most natural surfaces, because of its low reflectance throughout the electromagnetic spectrum. The reflectance of water bodies showed a decrease in reflectance with an increase in

wavelength. The signature of water produced a negative value with NDVI, and pixels in satellite images with the most negative NDVI values were correlated with water bodies. The shape of the spectral surface reflectance and its value in the red band greatly depended on the relative amounts of suspended minerals, chlorophyll and dissolved organic matter in the water. Under clear water conditions, the reflectance was found to decrease linearly with wavelength.

### **Cloud Detection**

Cloud contamination alters or sometimes completely obstructs the spectral signature of the land surface. The significant difference in spectral reflectance between clouds and the earth makes the process of distinguishing clouds from the Earth's surface difficult due to the high variability in cloud expression. Sheng Su and Xiao (1998) used thermal, infrared and visible channels of Advanced Very High Resolution Radiometer (AVHRR) to distinguish cloud cover from land cover. The spatial variance of cloud top temperature was noted to be greater than that of the Earth's surface, and the contextual feature of surface temperature was also used for cloud screening. Image analysis showed that cloud shadow caused a reduction in solar irradiance, and cloud shadow and water bodies were difficult to distinguish in the near infrared channel.

Melesse and Jordan (2003) used visible, short-wave infrared and thermal infrared bands from Landsat 5 to develop two vegetative indices for detecting clouds, cloud buildup and water in the Econ Basin, Florida. Clouds were detected and classified by using the simplified Plank constant to convert Band 6 digital number values to temperature. Image data was used to enhance dense clouds and urban features for visual analysis. For Landsat 7 ETM+, vegetative index two and vegetative index three are calculated as,

$$VI2 = \frac{Band2 * Band6}{Band7} \quad (2)$$

$$VI3 = \frac{Band6}{Band5 + Band3} \quad (3)$$

where Band 2 is the green band, Band 6 is the thermal infrared band, Band 7 is the middle infrared band and Band 3 is the red band. These indices were found to be effective for mapping dense cloud cover and partial clouds.

### **Airborne Laser Swath Mapping**

Airborne Laser Swath Mapping (ALSM), or light detection and ranging, Lidar, remote sensing utilizes a laser, detector, scanning system and Global Positioning Systems for topographic mapping. The complete process involves planning, collection, processing, filtering and editing echo points from the return signal data. Elevation post spacing is a function of flying height, speed, pulse rate and scan angle. Specifications of a commercial ALSM system generally describe laser, scanning, GPS, INS and flying operations and information concerning error and delivery (Table 2.2).

Table 2.1 Specifications of a commercial Lidar system.

Specification	Typical Value
Wavelength	1,064 $\mu$ m
Pulse Repetition Rate	5 – 33 kHz (50 kHz max)
Pulse Energy	100s $\mu$ J
Pulse Width	10 ns
Beam Divergence	0.25 – 2 mrad
Scan Angle	40 ° (75 ° Maximum)
Scan Rate	25 – 40 Hz
Scan Pattern	Zig-Zag, Parallel, Elliptical, Sinusoidal
GPS Frequency	1 – 2 times per second
INS Frequency	50 (200 maximum)
Operating Altitudes	100 – 1,000 m (6,000 m max)
Footprint	0.25 – 2 m (from 1,000 m)
Multiple Elevation Capture	1 – 5
Grid Spacing	0.5 – 2m
Vertical RMSE	15+ cm

Table 2.1 Continued

Horizontal RMSE	10 – 100 cm
Post-Processing Software	Proprietary

Topographic ALSM lasers use an infrared light beam (1064 nm) that is invisible, absorbed by water and strongly reflected by healthy vegetation and concrete. The laser is sent at a narrow dispersion angle ( $0.3 \mu\text{rad}$ ), and laser spot size or footprint is determined by flying height. The infrared beam reflects strongly off healthy vegetation, concrete and dry soils, however any presence of water will absorb and warp the beam path. It is important to note that birds and other airborne objects will reflect the infrared beam and produce an exceptionally high elevation value. Figure 2.1 shows how the beam reflects off of and penetrates a tree canopy to produce an elevation point.

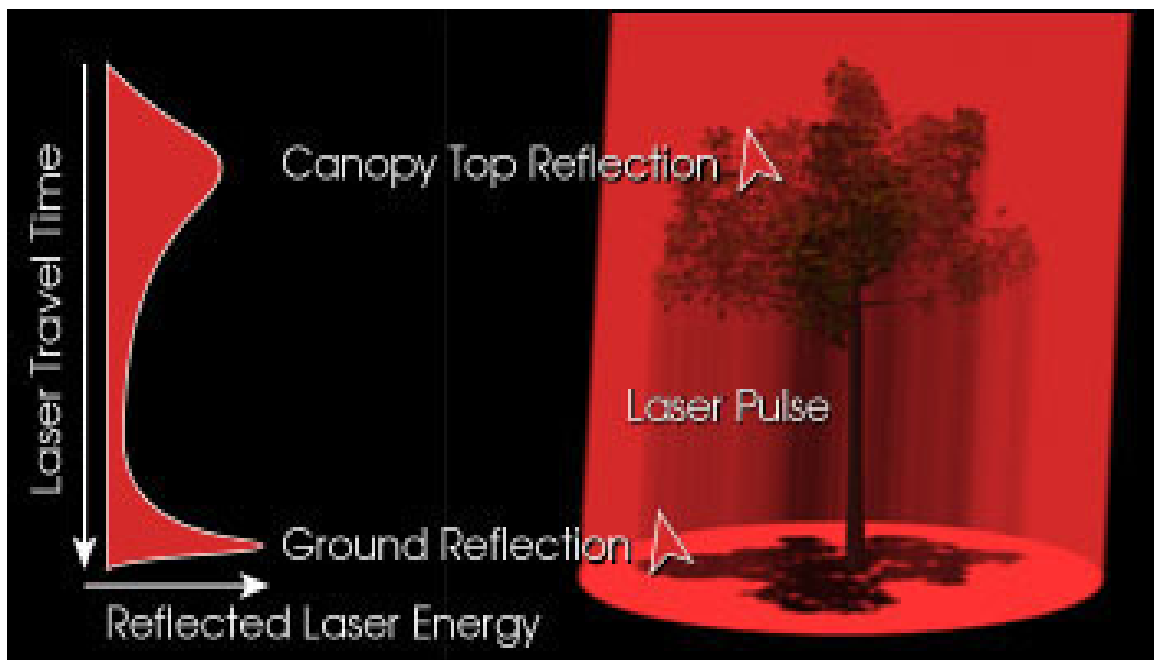


Figure 2.1 Illustration of a Lidar infrared beam. The actual beam diameter is smaller than what is shown in the figure. Source <http://earthobservatory.nasa.gov>

Intensity is the measure of the energy reflected from an object. Detecting return intensity involves recording the reflected or return beam energy from the earth surface. Objects possessing high reflectivity properties show a higher return energy than objects

possessing low reflectivity properties. Objects such as metal roofs and sand possess high reflectivity values, while water and black tar pavement possess low reflectivity values.

Different sensors have been developed to record multiple returns and reflected intensity. Multiple return signals occur when part of a distended beam strikes an above ground object and the remaining portion strikes the ground. When this occurs, the recorded signal will then display multiple elevation values from a single pulse. The above ground signal is the “first return” and the ground signal is the “last return”. Multiple returns are found in high, dense canopy areas, because the first and middle returns provide elevations for the top and intermittent growth. The last return usually reflects from the ground, however extremely dense canopy will prevent full penetration.

Kraus and Pfeifer (1998) noted if the beam strikes canopy or branches then the measured ground elevation value might be overestimated. This can lead to an asymmetric distribution error of laser scanner points. The research results emphasized the necessity to remove vegetation without deleting ground points for areas possessing low penetration rates.

### **ALSM Accuracy**

Post processing of ALSM data is performed to satisfy two requirements for product delivery. The first requirement derives accurate results based on GPS stations to provide a frame of reference for the airborne operation (Maune 2001). The second requirement is to solve a bare earth condition by removing irrelevant points, and this is accomplished with automatic or manual post processing methods. Automatic processing uses software algorithms to view neighborhood points and weigh them before removal. Manual processing is necessary, because automated algorithms may produce anomalies not characteristic of the bare earth condition. Occasionally, some apparent data anomalies

appear in files and the analyst may review aerial photography, digital imagery or videotape to identify anomalies (Maune 2001).

Few empirical studies exist for assessing the accuracy of digital elevation models created with ALSM. Under ideal conditions, absolute vertical accuracy for grass and pavement may be within 15 centimeters, but vertical accuracy cannot be obtained within 10 centimeters (Maune 2001). Daniels (2001) evaluated datum conversion issues and accuracy of ALSM by comparison of real time kinetic GPS sample points and lidar spot elevations. Base station, local orthometric height and regional offset corrections used to isolate potential datum offsets in lidar were necessary for mapping dynamic geomorphological surfaces.

Hodgson et al. (2003) found elevation root mean square error with ALSM was 33 centimeters for low grass and 153 centimeters for shrub/scrub land cover. In general, vertical errors with low grass and high grass were much smaller than in areas of heavy vegetation canopies. Hodgson and Bresnahan (2004) also noted that variation in land surface elevation was strongly correlated with a change in vegetation. Root mean square error values ranged from a low of 17-19 centimeters for low grass and pavement.

Shrestha et al. (2000) performed an accuracy assessment for surveying and mapping applications with ALSM. The results showed that elevation values for bare earth ground were accurate to within +/- 5 – 10 centimeters. The authors noted that ALSM technology was an innovative approach for high resolution flood plain and drainage mapping.

### **ALSM Point Removal**

Automated post processing of ALSM data attempts to model a bare ground condition by using software to identify and remove artifacts. Automated methods for

point removal are based on neighborhood operators that iteratively identify the lowest points within a defined search neighborhood. The operator then adds them to a candidate set of ground returns. Subsequent iterations select the candidate set by adding returns that are low or exhibit some angular deflection from a surface modeled by the current candidate set of points.

The details of search neighborhood operators and parameters vary by lidar mapping vendor. Generally, the analyst will examine a candidate set of ground returns to further improve the accuracy of labeling features. The procedure also requires an analysis of small areas as a three dimensional cloud of ALSM points overlain on available digital orthophotography. Thus, the process of point removal may contain errors, because removal is both adaptive and subjective.

Krabill et al. (2000) used ALSM to study changes in beach morphology. The research showed that post processing remained problematic for removing artifacts including near ground vegetation. Okagawa (2002) assessed multiple automatic filters to extract artifacts from digital surface models. The author concluded that image information was indispensable for identifying artifacts during post processing. Kampa and Slatton (2004) used a multiscale filter to segment bare ground from artifact points in ALSM data. To compute the mean square error for performance, the adaptive filter was initially applied to simulated ground data. The ground surface was distinguishable from artifact points for a point density of twelve points per 25 square meter grids.

Raber et al. (2002) used an adaptive filter to minimize the overall error by applying different vegetation point removal parameters based on vegetation type. The study involved extracting vegetation land cover type information using only ALSM multiple

return data. The study showed that land cover information could be used adaptively in ALSM vegetation point removal for the production of accurate elevation models. Land cover observations involved analysis of color infrared imagery, ground control points and vegetation land cover. Histogram analysis showed that monoculture canopies were characterized by a dampened bimodal histogram. A statistical analysis further showed that among all land cover types, low and high grass possessed the lowest mean absolute error values.

Huising and Pereira (1998) studied bare earth modeling and found that separating dense vegetation from bare ground was a protracted process. The authors observed that manual filtering may be better than automated, however more time is required for post processing large areas. The manual method was found to be ideal for filtering vegetation and other artifacts in small areas. The authors concluded that using only topography data compounded the problem, and aerial photography was determined essential for classifying land features. The accuracy of elevation measurements was related to the laser system and terrain geometry, and flat terrain and low grass areas were used to estimate accuracy.

### **ALSM Applications**

Persson, Holmgren and Soderman (2002) used ALSM to detect individual trees by estimating height crown closure and stem volume. The study used the lowest laser reflection points to derive bare earth DTMs. The study further noted that return intensity and type return pulse data provided more information about tree structure. Hodgson et al. (2003) also used orthophotography and ALSM surface cover height to map impervious land surfaces.

Multiple remotely sensed data sets may be used to separate vegetative height from a theoretical bare earth condition. Popescu and Wynne (2004) combined lidar and multispectral data to accurately estimate plot level tree height by focusing on the individual tree level. Combining small footprint airborne lidar data in conjunction with spatially coincident optical data was found to help accurately predict tree heights of interest for forest inventory and assessment. The study recommended that project methodology can be applied to process lidar data for vegetation removal, and individual tree location.

Popescu and Wynne (2003) developed analysis and processing techniques to facilitate the use of small foot print ALSM for estimating plot level tree height. This was accomplished by measuring individual trees identifiable on a three dimensional ALSM elevation model. The study used the combination of ALSM and multi-spectral optical data fusion to differentiate between forest types and improve the estimation of average plot heights for pines. The research demonstrated that small foot print ALSM, used in conjunction with spatially coincident optical data, was accurately able to predict the tree heights of interest for forest inventory and assessment.

Hopkinson et al. (2004) used ALSM to map snowpack depth under forested canopies. Snow pack distribution patterns were mapped by subtracting a bare earth DEM grid from a peak snowpack DEM grid. Snow pack depth was used to predict water availability and flood levels during the warming period. The study also found that a high proportion of last pulse returns led to an overestimation of ground elevation. The study recommended a further assessment of type dependent elevation offsets for improving elevation and snow depth estimation.

Brock et al. (2001) used ALSM to recognize and map surfaces that provide accurate low variability topographic measurements. These features were termed fiducial and were used as reference base line features for mapping morphology. Fiducial features are naturally occurring bald earth features such as beaches, bare dunes and ice sheets. The process for separating dense plants of less than 10 centimeters was difficult based solely on passive spectral signatures of ALSM. The presence of vegetation increases the difference between ALSM and ground survey elevations from a minimum of 0.26 meters over bare sand to values near 0.40 meters for all vegetation classes. Of the four defined vegetation classes consisting of mono, sparse, medium and dense, sparse vegetation possessed the highest variance between ALSM and coordinate survey elevations.

Evans et al. (2001) used sampling theory to map individual trees and estimate tree height. Small foot print lidar failed to yield ground returns in areas dominated by dense vegetation canopy.

Renslow and Gibson (2002) developed bare earth models from ALSM and high resolution aerial photography to assist the decision making process for increasing services for utility companies. This was accomplished by mapping fast track utility corridors using bare earth models. Heinzer et.al (2002) used ALSM and aerial images to model inundation, velocity and steady state flow of water. Interestingly, bare earth models were interpolated from group points; however buildings were reinserted to display realistic structural definitions.

### **Geographic Information Systems**

Geographic Information Systems, GIS, is software designed to create maps by capturing, storing, retrieving, manipulating and displaying geographically referenced

spatial tabular data (www.usgs.gov, April 2006). The three types of spatial data common in GIS are points, arcs (lines) and polygons (areas).

GIS thematic map layers can display topological relationships between mapped features. Topology refers to recording the spatial relationship between points, arcs and polygons. A coverage is a GIS data file that display topology, however some GIS data files such as shape files do not display topological relationships.

Metadata files list important parameters describing attributes of remotely sensed and GIS data products. Metadata typically includes the coordinate system, period of data capture and ancillary information pertinent for mapping applications with other data sets.

### **Spatial Modeling**

There are two classes of interpolation, deterministic and geo-statistical. Deterministic methods such as inverse distance weighting, splines, and radial based functions are directly based on an interpolator that uses the surrounding measured values or mathematical formulas applied to those values. Geostatistical models, such as kriging, predict values by accounting for the probabilistic spatial relationship among neighboring points. Kriging is able to predict estimation errors and is often preferred over deterministic methods.

The surface calculated using inverse distance weighting depends on the selection of a power value and the neighborhood search strategy. For inverse distance weighting the maximum and minimum values in the interpolated surface can only occur at sample points. The output surface is sensitive to clustering and the presence of outliers. Inverse distance weighting assumes that the surface is being influenced by the local variation, which can be captured throughout the neighborhood.

The local polynomial method is a moderately quick and smooth deterministic interpolator. It is more flexible than the global polynomial method; however there are more parameter decisions. There is no assessment of prediction errors; however the method provides prediction surfaces that are comparable to kriging with measurement errors. Local polynomial methods do not allow any analysis of the spatial autocorrelation of the data, thus it is less flexible and more automatic than kriging.

The global polynomial method is also a quick and smooth deterministic interpolator. There are fewer decisions to make regarding model parameters than for the local polynomial method. It is best used for surfaces that change slowly and gradually. There is no assessment of the prediction errors and this method may produce a surface that may be too smooth. Values at the edge of the data can have a significant impact on the interpolated surface.

Radial based functions are moderately quick deterministic interpolators that are exact, and they are considerably more flexible than inverse distance weighting, however there are more parameter decisions, and there is no assessment of prediction errors. The method provides prediction surfaces that are comparable to the exact form of kriging. Radial based functions do not allow for analysis of the autocorrelation of the data, thus making it less flexible and more automatic than kriging. Radial based functions are used for calculating smooth surfaces from a large number of data points, and are preferred for gently varying surfaces such as elevation. The radial based function is inappropriate when there are large changes in the surface values within a short horizontal distance and/or when the sample data is prone to error or uncertainty.

Ordinary kriging produces interpolated values by assuming a constant but unknown mean value, allowing a local influence from nearby neighboring values. Because the mean is unknown, there are few assumptions about the data. This makes ordinary kriging flexible but less powerful.

Simple kriging produces interpolated values by assuming a constant but known mean value, allowing local influences due to nearby neighboring values. Because the mean is known it is slightly more powerful than ordinary kriging but in some cases the selection of a mean value is not well known.

Universal kriging produces interpolated values by assuming a trend surface with unknown coefficients in the model; however it allows local influences from nearby neighboring values. It is possible to overfit the trend surface, which fails to leave enough variation in the random errors to properly reflect uncertainty in the model. It can be more powerful than ordinary kriging because it explains much of the variation in the data through a non-random trend surface.

Disjunctive kriging considers functions of the data, rather than just the original data values themselves, and stronger assumptions are required. Disjunctive kriging assumes all data pairs come from a bivariate normal distribution and the validity of these assumptions should be checked. A bivariate normal distribution describes relative frequencies of occurrence in the population of pairs of values. When this assumption is met, the functions of the data are indicator variables that transform the continuous data values to binary values based on a decision threshold value.

Doucette and Beard (2000) evaluated inverse distance weighting, splines and universal kriging as interpolators to fill gaps left by occlusions in digital elevation data.

The results favored splines as a surface interpolator, especially as terrain roughness increased. The study additionally found that altering the search radius parameter significantly impacts interpolation error statistic values.

Selecting a best fit model depends on the assessment of several modeling statistics. In general, the best fit model is one that has the standardized mean error closest to zero, the lowest root mean squared prediction error, the average standard error nearest to the root mean squared prediction error and the standardized root mean squared prediction error closest to one (ESRI 2001).

### **Inundation Mapping with GIS**

Previous flood mapping efforts have used remote sensing and GIS to map the extent, duration and magnitude of flooding. Ball and Schaffranek (2000) used topographic and surface water grids to map water depth in the southern Everglades. Temporal inundation patterns were mapped and compared to historical and current water depths. A comparison to other hydroperiods was conducted to isolate temporal changes affected by anthropogenic influences of water management policy. To estimate water depth accuracy, computed depths were subtracted from depths measured in the wetlands adjacent to the C-111 canal and in Taylor Slough in 1997 and 1999.

Ball and Schaffranek (2000) employed a similar method to study water surface elevation and water depth for Taylor Slough in the southern Everglades. A GIS program was used to subtract topographic elevation grids from surface water elevation grids. The extremely low topographic relief of the southern Everglades produced significant spatial variability in surface water gradients. Furthermore, the land surface elevation grid was calculated from interpolating global positioning systems (GPS) topographic data sponsored by the USGS, National Mapping Division. Daily surface water data was

obtained from the SFWMD, and National Park Service (NPS) Everglades National Park. The research concluded that water depth and topographic accuracy were directly correlated to the spatial resolution and accuracy of input data. Project inundation grids were calculated with the same method; however an ALSM topographic grid was used instead of a GPS topographic grid. ALSM topographic grids produce inundation maps with a finer spatial resolution than GPS topographic grids.

## CHAPTER 3 DATA RESOURCES AND METHODOLOGY

### **Introduction**

Project data sources include aerial color infrared imagery, Landsat7 EMT+ sensor data, surface water elevation data and ALSM topographic data. All tables that are referenced can be found at the end of this chapter.

Color infrared imagery was acquired from Land Boundary Information Systems ([www.labins.com](http://www.labins.com) April 2006), Labins, and each image possessed a 1 meter spatial resolution. Color infrared imagery for the study area is found in quadrangle Royal Palm Ranger Station or Quadrangle 1205 S.W. and was obtained for 1994 and 1999. The primary use of color infrared imagery was to identify vegetation points in the NAD 27 and NAD 83 ALSM point data sets.

### **Surface Water Data**

Surface water elevation values for regional canal stations and well monitoring sites were obtained from the South Florida Water Management District (SFWMD), U.S. Geological Survey (USGS) and National Park Service (NPS). Surface water elevation data covers the period during October 12-22, 1999. SFWMD canal stage elevations were recorded for both head and tail stage, and the mean between head and tail was used to create surface water grids. Surface water values were recorded in feet, and NGVD29 was used as the reference vertical datum for hydrologic and topographic data sets.

### **Digital Elevation Model Construction**

In 1999, FEMA and NASA sponsored 3001©, a consulting firm, to conduct ALSM flight operations for the C-111 basin. ALSM files are arranged by flight area, and each flight area includes a cache of files that provide a variety of elevation data products. ALSM data was captured by single pulse return data, and the products included text files of x,y,z coordinates and processed DTM files. All coordinate elevation values were recorded in feet, and text files were prepared for all first return raw data and automated filtered bare earth data. NAD 27 raw data values were recorded to either one-hundredth or one thousandth of a foot. All NAD 83 bare earth file data were recorded to one one-hundred thousandth of a foot. Only accuracies of hundredths of a foot should be considered for DEM analysis, because real time kinematic GPS values are only accurate to one one-hundredth of a foot. The post spacing for points was 10 feet along the track direction and 23 feet across the track direction. Bare earth contour line DTMs were included for each area and elevation lines were categorized by one-foot intervals. These DTMs were not used in this study, because of their low vertical resolution.

Data quality reports were prepared for all areas and they included coordinates for flight area ground control points in addition to the methodology used to create the bare earth digital terrain models. These reports are commonly used to inform the client about the accuracy of ALSM data by a statistical comparison between ground surveyed GPS points to associated ALSM points. Data quality reports for the study area listed a vertical accuracy of 15 centimeters, and bare earth DTM files were created using Delaunay triangulation (3001 1999). Bare earth files were created using proximal analysis to filter unwanted points according to the report; however no additional information was provided about the procedure.

### **Landsat 7 Enhanced Thematic Mapper**

Landsat 7 ETM + image data were used to detect inundated surfaces and dense clouds within the study area after Hurricane Irene. Landsat7 scenes for October 16, 1999, and April 9, 2000, were obtained from the USGS, and all data deliverables were stored on CD-ROM media and delivered as Geotiff files. For image processing, all Geotiff files required both importation in ERDAS Imagine and exportation as an ERDAS Imagine image file. The first scene was captured on October 16, 1999, nine hours after Hurricane Irene passed over the C-111, and the second was captured on April 9, 2000 during the peak of the dry season.

A bend in the L31W canal was used to detect an offset between the October 16, 1999, and April 9, 2000, Landsat 7 ETM+ scenes. Band 8 was used from both scenes to locate the x and y values for associated pixels, and the offset was measured. The offset between associated pixels was 48 ft. north and 1 ft. east.

### **Vegetative Index Methodology**

ERDAS Imagine is software that is specifically designed to work with large geo-referenced image data sets. NDVI map methodology was initiated by creating a layer stack of red and infrared bands for both Landsat7 scenes. The ERDAS Imagine layer stack function combined sensor data, and the NDVI function automatically created an NDVI image by separating Band 3 and Band 4 from the stack and substituting them into the NDVI equation.

The ERDAS Imagine Spatial modeler extension selected the appropriate individual band layers in a composite layer stack and substituted them into their designated vegetative index equations. The Spatial Modeler tool was used to create vegetative index two and vegetative index three indices described in Chapter 2.

### **Unsupervised Classification**

An unsupervised classification divides pixels into classes based on their digital number value. ERDAS Imagine unsupervised classification was performed on the three vegetative index images, and 30 classes were created for all vegetative index maps. All vegetative index unsupervised images were scaled with Class 1 representing the lowest reflectance grouped values and class 30 representing the highest reflectance grouped values.

### **ALSM Processing**

Topographic grids were created from NAD 83 / NGVD 29 and NAD 27 / NGVD 88 ALSM data. The procedure for creating a point map theme from text data required a list of vertical, horizontal and elevation values. All text files were space delimited and consequently, no files could be opened by GIS software. Only tab and comma delimited formats are recognized by GIS software for importation. Furthermore, all text files were too large to fit the 65,536 spreadsheet row entry maximum. In response to this constraint, a quick and effective procedure was developed to convert text files into shape files.

The conversion of text files into database tables was required for importation into GIS software. This initial step involved opening each text file with Microsoft Wordpad, and converting the native .xyz format to an ASCII text file. The ASCII text file was opened in a spreadsheet and saved as a database file; however spreadsheet row entries were limited to only 65,536 displayed values. The Find and Replace tool in Microsoft WordPad located the 65,536th value in the text file, and all values listed above the 65,536th value were selected and deleted. The altered file was saved under the original text file name, and displayed the 65,536th value as the first value in the spreadsheet. All cells were converted to a number format with six decimal places and the column

containing coordinate values were assigned X, Y, and Z field headings respective to their measurements. The process was applied to all files until the original text file was reduced to an acceptable size for one spreadsheet. The end result produced a series of spreadsheets with each representing one sub-area.

Arcview 3.2 was used to develop a point shape file from the data base file. All database tables were imported into Arcview, and the Add Event function was used to display the table coordinate values as points for all data base tables imported into Arcview. Arcview's Geoprocessing tool was used to merge and convert sub area database files into a point shape file. The geoprocessing tool designates the tables to be merged and then exports the resultant thematic shape file to a known file directory. The offset coordinate value between NAD 83 and NAD 27 was 156235.73 ft. false east and 159.86 ft. false north. These values were later used to project surface water data points from NAD 27 to NAD 83.

### **Bare Earth Modeling**

The procedure for modeling a bare earth condition for the study area involved the manual removal of ALSM points that represent vegetation, fiducial features and structures. Point removal was based on the assumption that the study area possessed a flat topography and low elevation characteristic of the C-111 basin. The steps utilized in the process included a cross-comparison between color infrared imagery, NAD 27 ALSM DEM, and ground control point elevations in the study area. Multiple interpolators and search parameters were tested for predicting grid elevation values.

ALSM data was collected in NAD 83 and NGVD 88 datum; however the unfiltered data was placed in NAD 27 and NGVD 29. The measured difference between NGVD 29 and NGVD 88 first order benchmark elevation values is 1.5125 ft. Project inundation

maps were placed in NGVD 88, because this was the vertical datum used in the data collection process.

The proximal analysis method was used by 3001 © to model the bare earth condition for NAD 83 data, however this method is not defined in the data quality report for Area 2. Furthermore, this method was not sufficient for flood mapping, because vegetation points were found in the bare earth model for the study area. The success of topographic bare earth models relies on the accuracy of the estimated maximum bare earth elevation threshold used to remove points.

### **Aerial Color Infrared Analysis**

The available Land Boundary Information System (Labins) aerial imagery covered the dates of December 27, 1994, Figure 3.1(a) and February 21, 1999, Figure 3.1(b). Aerial color infrared imagery was useful for identifying vegetation patterns and associated land features in ALSM maps. Healthy vegetation in images possessed a strong reflectivity in the infrared region of the electromagnetic spectrum, and was displayed as red. Although row crop vegetation reflected strongly as red, the individual boundaries varied between both images. In both images, dense tree canopies reflected the strongest and were easily distinguished from the surrounding land cover. In the 1999 image, wetland forest was characterized by variable red reflectivity values; however only high dense tree canopies were consistently reflected as red in the 1994 image. The soil mound seen in Figure 1.2, reflected as white in the 1994 image when leaf canopy was reduced, and was difficult to distinguish from the surrounding land cover. In the 1999 aerial image, the soil mound was easily distinguished from the heterogeneous cover of healthy vegetation and exposed bare soil.

In the 1999 aerial image row crop vegetation conformed to field boundaries, however in the 1994 aerial image not all row crop vegetation conformed to field boundaries. This dissimilarity was most noticeable in canopy patterns found in leased parcel 19. A semi-circular arc of vegetation can be seen in the southeast quadrant of the 1994 image, Figure 3.1(a). This was useful for identifying suspect vegetation patterns found in the raw ALSM topographic DEMs.

### **Ground Control Point Analysis**

Although ground control points, GCP, were not in the study area, they were analyzed for determining the threshold value for estimating the bare earth condition, Table 3.1. The process for determining vegetation points was subjective. This depended on visual analysis and analysis of nearby ground control points in the NAD 27 DEM. The objective of the approach was the removal of vegetation points, while preserving points that represented roads and bare earth. Based on this methodology, the value of 4.80 ft. was determined to be the maximum bare earth elevation value for the study area for NAD 27. Consequently, all points in the associated NAD 83 DEM that exceeded the value of 3.29 ft. were also identified as vegetation and removed using the clip tool in Arcview. Recall that the difference between NAD 83 and NAD 27 maximum bare earth elevation values is 1.51 ft., and this is equal to the difference between NGVD 29 and NGVD 88 elevation values. Arcview's query filter was used to remove elevation points that exceeded the designated maximum elevation threshold value. The clip tool in Arcview was used to create a separate shape file consisting only of points that were not deleted.

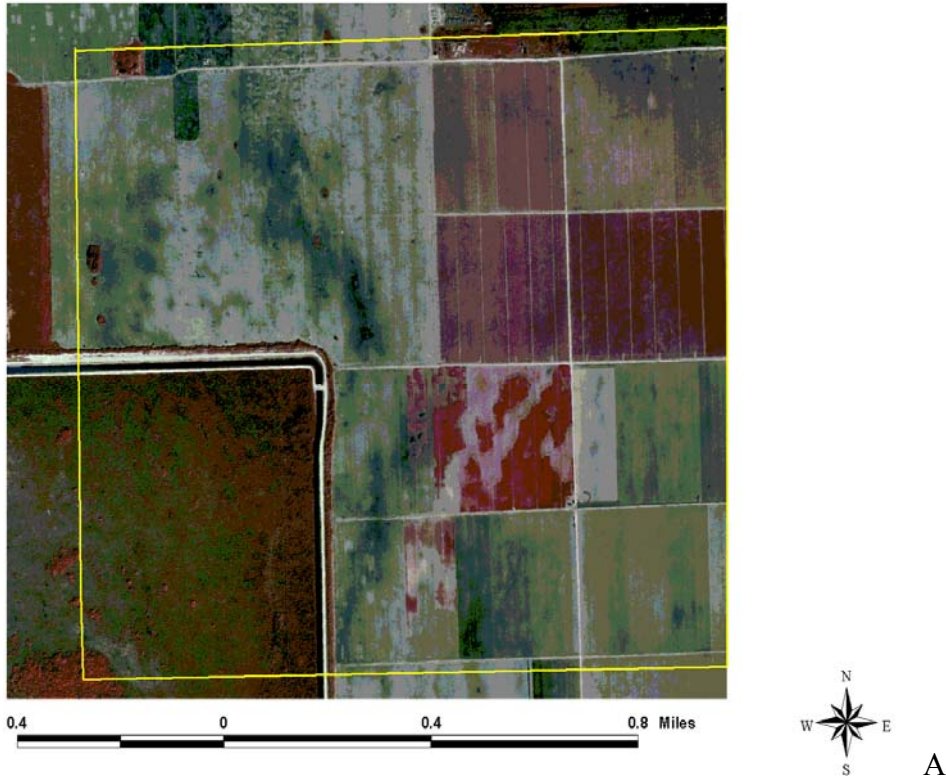
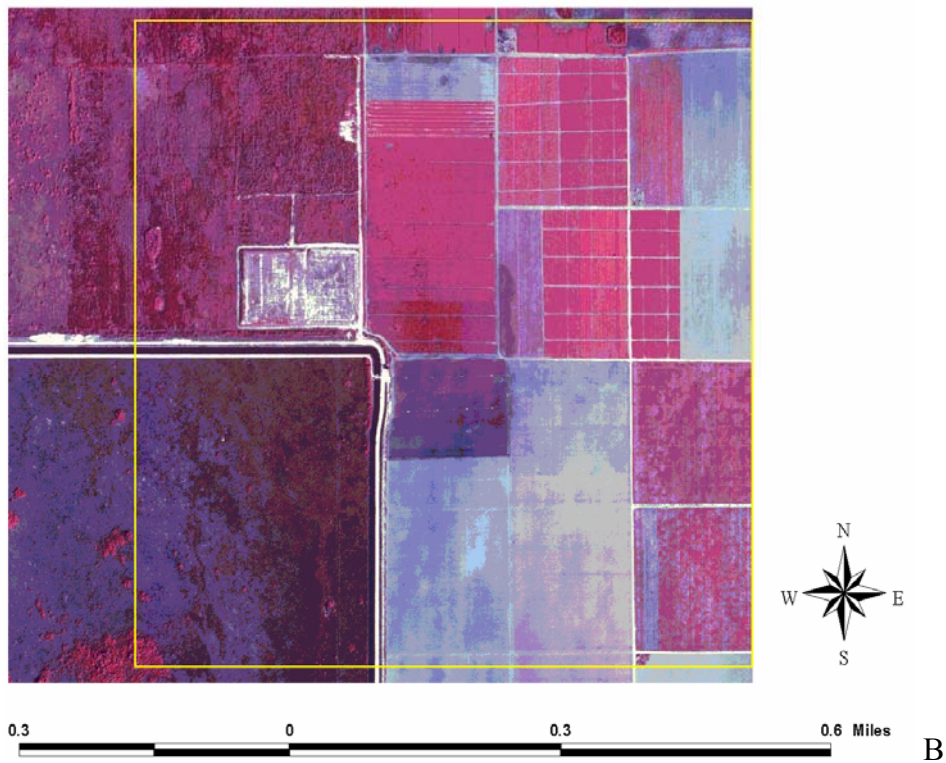


Figure 3.1 Color infrared aerial photos of the study area. (A) 1994 color infrared aerial image (B) 1999 color infrared aerial image. The study area is outlined in yellow.



### **Topographic Spatial Modeling**

Multiple interpolators were used to develop prediction grids for NAD 27 and NAD 83 point shape files. These interpolators included inverse distance weighting, local polynomial, global polynomial, radial based functions, universal kriging, ordinary kriging, simple kriging and disjunctive kriging. The root mean square error, RMSE, statistic was calculated by sequential dropping of each observed elevation point and estimating it using the appropriate interpolation procedure. The RMSE was used to select the optimum interpolation method for surface water and topographic grids. If two tests possessed an equal RMSE statistic, then the mean absolute error, was used as the next decision statistic.

All prediction grids, including surface water, were exported as raster surfaces to be later used for calculating inundation grids. All interpolation methods were used to generate z prediction values for a test x and y location, the results of the different prediction methods showed that the predicted values at the test location ranged from 2.9217 ft. to 2.9483 ft. The difference in z prediction values indicates that a small variation exists between predicted topographic grids using the various methods.

Table 3.2 lists the search parameters for the inverse distance weighting method that were not set to a default value. The neighborhood method was used for all tests. The search ellipse used for the neighborhood search had major and minor semi-axes of 2,134.6 ft., and the anisotropy factor was set to a value of 1. The x and y test prediction locations were 797,555.55 ft. and 394,614.36 ft. respectively. Table 3.3 lists the search parameters for the global polynomial method. Table 3.4 lists the search parameters for local polynomial method. Table 3.5 lists the search parameters for radial based function tests.

Table 3.6 lists the search parameters used for kriging methods. For all kriging methods, no transformation was applied, and no trend was assumed. The angle direction and tolerance were  $15^\circ$  and  $45^\circ$  and the band width was 6. The number of lags was 12, the search shape angle were 3 and  $15^\circ$  respectively. The major and minor semi-axes were 6,306.9 ft. and 5,546.8 ft., and the anisotropy factor was 1.137. The test x and y locations were 797,555.95 ft. and 394,614.36 ft., and twenty neighbors were used for the test prediction value.

### **Surface Water Elevation Map Methodology**

The surface water elevation map (SWEM) was created to show the change in surface water elevation values over the study period, and was used to calculate inundation grids. All surface water data was acquired from the SFWMD, USGS, and the NPS. All surface water project data values were referenced with NAD 27 horizontal datum and NGVD 29 vertical datum. NGVD 29 surface water elevation values were converted to NGVD 88 by subtracting 1.51 ft from NGVD 29 values.

REMO is the SFWMD internet data retrieval program that provided surface water elevation data. REMO hydrologic data was delivered in text format and all data was converted to data base file format. All water elevation data was recorded in feet and referenced to NGVD29. Canal elevation measurements included head and tail measurements; however the mean value between head and tail was used to create surface water grids. SFWMD data sites included the S175, S177, S178, FP, FP1, FP2 and S332D. FP, FP1 and FP2 are wells and the S175, S177, S178 and S332D are water control structures. Figure 3.2 shows in situ measurement sites used to create SWEM.

USGS provides maximum daily ground water elevations for monitoring stations in Miami-Dade. USGS maximum water elevation data for G3355 was acquired through the

USGS water resources internet link with the SFWMD, and USGS water resources for Miami-Dade. G3355 is located in the southeast corner of Figure 3.2.

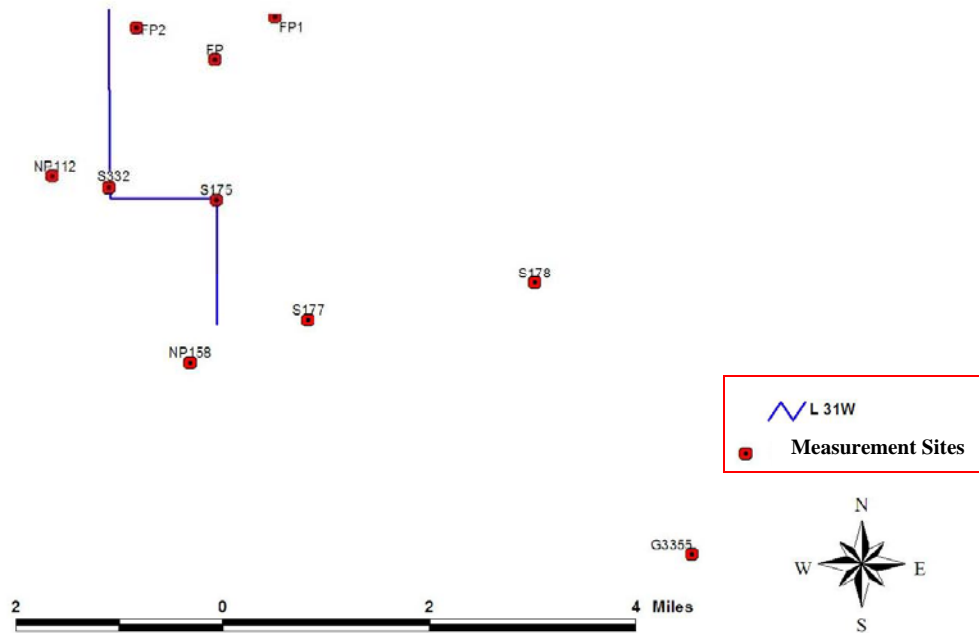


Figure 3.2 Map of measurement sites.

USGS sponsors Tides and Inflows in the Mangroves in the Everglades, TIME ([time.er.usgs.gov](http://time.er.usgs.gov)). TIME provides telemetric surface water elevation measurements in daily, hourly and fifteen minute intervals. TIME water monitoring wells NP112 and NP158 were used to create surface water grids. The locations NP112 and NP158 are shown in Figure 3.2.

The procedure for developing the surface water site point shape file began with transforming the Latitudinal and Longitudinal coordinates from Degrees-Minutes-Seconds to Data-Decimal-Degrees, DDD,

$$DDD = Degrees + \left( \frac{Minutes}{60} \right) + \left( \frac{Seconds}{3600} \right) \quad 1)$$

The DMS coordinates were divided into separate spreadsheet fields, and the conversion for each coordinate was performed using cell formulas. Longitudinal coordinates were assigned negative values. The resultant spread sheet file was exported as a tab delimited text file and assigned a .dat extension.

The ERDAS Imagine vector tool was used to export the .dat files as Arcinfo coverages. The coverage file was opened in Arcview, and the view properties were set to match the projection parameters of ALSM as defined in the meta-data report, Table 3.7. Finally, the coverage file was converted to a shape file with the same coordinates as the ALSM data.

### **Surface Water Elevation Map Interpolation**

Tables 3.8, 3.9, 3.10 and 3.11 list the initial search parameters for kriging tests used to estimate the surface water elevation. A description of these parameters is discussed below.

For universal kriging no trend removal and no transformation were performed. A bandwidth of 6 ft. and the lag size and lag number were 2,721 ft. and 12. The major semi-axis and minor semi-axis for the neighborhood search ellipse were 30,000 ft. and 24,000 ft. The anisotropy factor was set to a default value of 1.25 for all tests. The x and y test prediction locations were 804,799 ft. and 389,908 ft. The software's default value for search neighbors was used, and the number of search neighbors was set to five for prediction.

For disjunctive kriging, no transformation or trend removal was conducted. The direct method was used, and the major and minor ranges were 30,023 ft. and 12,607 ft.

The search direction, partial sill and nugget were  $64.9^\circ$ , 0.64504 ft. and 0.0221170 ft., respectively. The lag size and number were 2,721 and 12. The major and minor semi-axes were 30,023 ft. and 12,607 ft. The anisotropy factor was set to 2.3815. The x and y test location values were 804,799 ft. and 389,908 ft., and the bandwidth was set to 6 ft.

For ordinary kriging, no transformation or trend removal was conducted. The major and minor ranges were 30,705 ft. and 26,007 ft. The angle direction, partial sill and nugget were  $14.8^\circ$ , 1.1645 ft. and 0 ft., respectively. The lag size and number were 2,721 ft. and 12, and the bandwidth was set to 6 ft. The major and minor semi-axes were 30,705 ft. and 26,007 ft. The anisotropy factor was 1.1806, and the x and y test location values were 804,799 ft. and 389,908 ft.

For simple kriging, no transformation was applied, and the mean threshold value not to be exceeded was 3.857 ft. The bandwidth was set to 6 ft., and the major and minor ranges were 30,091 ft. and 21,698 ft. The anisotropy factor was activated for all tests, and the nugget was 0.42352 ft. The lag size and number were 2,721 ft. and 12 respectively. The search angle direction and partial sill were  $20^\circ$  and 0.61003 ft. The major and minor semi-axes were 30,705 ft. and 26,007 ft. The test x and y prediction locations were 804,799 ft. and 389,908 ft.

Table 3.12 lists the search parameters for universal kriging for SWEM. The universal kriging major range was set to 30,668 ft. and the minor range was set to 25,892 ft. The major semi-axis and minor semi-axis were set to 30,000 ft. and 24,000 ft. The anisotropy factor was set to 1.25. The test prediction location was 804,799 ft. and 389,908 ft. The lag size and number were set to 2,721 ft. and 12 respectively. Eight neighbors were used for the search parameters. No trend removal and or transformation

were conducted. The global influence, local influence, angle direction, angle tolerance, search direction and were equal to 65%, 35%, 15%, 35°, 15° and 6 ft. respectively. Shape 3 was selected and the shape angle was set to 15°.

### Surface Water Inundation Map Methodology

The surface water inundation map, SWIM, was calculated by subtracting ALSM topographic grid values from SWEM grid values. Surface water and topographic grids were exported as raster surfaces with a 3 meter resolution. The raster math calculator in ArcGIS Spatial Analyst extension was used to subtract topographic grids from surface water grids, and the resultant inundation grids also had a 3 meter spatial resolution. A value of 0 ft. in elevation was inserted into the L31W canal to prevent aliasing caused by interpolation.

3D ALSM DEMs were useful for determining elevation values that represented vegetation. Converting the raster surface into a TIN created 3D TIN DEMs, and the TIN was imported into ArcGIS Scene.

Table 3.1 Area 2 static GPS points used to determine the elevation filter. Z1 is the elevation of the GPS point, and Z2 is the measured ALSM elevation for that point.  $\Delta Z$  is the difference in elevation between Z1 and Z2.

Test Id	Z1 ft.	X ft.	Y ft.	Z2 ft.	$\Delta Z$ ft.
663	4.50	640246.31	394360.81	4.890	0.390
665	4.46	640248.90	394361.10	4.890	0.430
729	4.72	640518.40	392310.00	4.660	0.060
732	4.31	640707.30	392308.60	4.300	0.010
733	4.29	640716.80	392308.50	4.400	0.110
734	4.60	640728.50	392308.40	4.400	0.200
735	4.61	640739.40	392307.80	4.630	0.020
736	4.67	640752.00	392306.70	4.660	0.010
737	4.64	640763.10	392307.20	4.660	0.020
738	4.51	640774.10	392305.30	4.760	0.250
739	4.66	640785.90	392304.50	4.630	0.030
741	4.59	640495.50	392311.90	4.860	0.270

Table 3.1 Continued.

Id	Z1 ft.	X ft.	Y ft.	Z2 ft.	$\Delta Z$ ft.
742	4.65	640484.10	392312.90	4.660	0.010
743	4.65	640472.00	392314.00	4.760	0.110
744	4.55	640460.70	392313.50	4.660	0.110
745	4.52	640449.80	392316.20	4.530	0.010
746	4.53	640438.80	392318.60	4.430	0.100
746	4.53	640438.80	392318.60	4.530	0.000
747	4.59	640427.50	392321.10	4.890	0.300
749	4.63	640402.80	392324.90	4.660	0.030

Table 3.2 Inverse distance weighting search parameters for topography<sup>1</sup>.

Test Id	Power	Shape	Shape Angle	Neighbors	Prediction
1	2	3	15	60	2.9338
2	1.7682	3	15	60	2.9446
3	1.7682	1	15	15	2.9343
4	1.7682	2	15	60	2.9444
5	1.7682	4	15	120	2.9480
6	1.7682	4	10	120	2.9483
7	1.7682	1	10	15	2.9343
8	1.7682	2	10	60	2.9443
9	1.7682	3	10	60	2.9446
10	2	1	20	15	2.9343
11	2	2	20	60	2.9443
12	2	3	20	60	2.9449
13	2	4	20	120	2.9356
14	2.7365	1	20	15	2.9217
15	2.7365	2	20	60	2.9222
16	2.7365	3	20	60	2.9220
17	2.7365	4	20	120	2.9223
18	2.7365	4	15	120	2.9223
19	2.7365	3	15	60	2.9222
20	2.7365	2	15	60	2.9222
21	2.7365	1	15	15	2.9217
22	2.7365	1	10	15	2.9217
23	2.7365	2	10	60	2.9222

<sup>1</sup> The shape angle is in degrees. Shape type refers to the search shape used for all interpolation tests. Shape 1 is an open circle and shape 2 is a circle divided by four perpendicular lines running north, south, east and west. Shape 3 is a circle divided by four perpendicular lines running northeast to southwest and northwest to southeast. Shape 4 is a circle divided by eight lines that possess the same directions as Shapes 2 and 3.

Table 3.2 Continued

Test Id	Power	Shape	Shape Angle	Neighbors	Prediction
24	2.7365	3	10	60	2.9222
25	2.7365	4	10	120	2.9223
26	2.7365	4	5	120	2.9223
27	2.7365	3	5	60	2.9222
28	2.7365	2	5	60	2.9222
29	2.7365	1	5	15	2.9217
30	2.7365	1	0	15	2.9217
31	2.7365	2	0	60	2.9222
32	2.7365	3	0	60	2.9222
33	2.7365	4	0	120	2.9223
34	2.7365	4	25	120	2.9223
35	2.7365	3	25	60	2.9222
36	2.7365	2	25	60	2.9222
37	2.7365	1	25	15	2.9217

Table 3.3 Global polynomial search parameters for topography.

Test Id	Power
1	2
2	2

Table 3.4 Local polynomial search parameters for topography.

Test Id	Global Influence (%)	Local Influence (%)	Power
1	10	90	1
2	15	85	1
3	20	80	1
4	25	75	1
5	30	70	1
6	0	100	1
7	10	90	2
8	20	80	2
9	25	75	2
10	30	70	2

Table 3.5 Radial based function search parameters for topography. SWT is spline with tension, MQ is multi-quadratic, CRS is completely regularized spline, IM is inverse multi-quadratic and TPS is thin plate spline.

Test Id	Kernal Function	Parameter	Shape	Shape Angle	Z Prediction Value ft.	Neighbors
1	SWT	1.3715	3	15	2.9500	60
2	SWT	1.3715	1	15	2.9494	15
3	SWT	1.3715	2	15	2.9500	60

Table 3.5 Continued

Test Id	Kernal Function	Parameter	Shape	Shape Angle	Z Prediction Value ft.	Neighbors
4	SWT	1.3715	4	15	2.9500	64
5	SWT	1.3715	4	20	2.9499	64
6	SWT	1.3715	3	20	2.9504	32
7	SWT	1.3715	2	20	2.9500	32
8	SWT	1.3715	1	20	2.9468	8
9	SWT	1.3715	1	10	2.9468	8
10	SWT	1.3715	2	10	2.9498	32
11	SWT	1.3715	3	10	2.9504	32
12	SWT	1.3715	4	10	2.9500	64
13	SWT	1.3715	4	5	2.9500	64
14	SWT	1.3715	3	5	2.9505	32
15	SWT	1.3715	2	5	2.9500	32
16	SWT	1.3715	1	5	2.9468	8
17	MQ	0	1	5	2.9382	8
18	CRS	0.47662	1	5	2.9240	8
19	IM	7.3705	1	5	2.9248	8
20	TPS	1 e <sup>20</sup>	1	5	2.9274	8

Table 3.6 Kriging search parameters for topography.

Type	Major Range	Minor Range	Direction	Partial Sill	Nugget	Lag Number	Z Prediction Value ft.
OK	6306.9	5546.8	274.4	0.015308	0.0406	532.08	3.0653
SK	1437.7	915.89	288.8	0.02606	0.0249	187.38	3.0558
UK	6040	6040	9.0	0.0000	0.013034	532.08	3.0660
DK	1350.4	957.16	290.8	0.45212	0.41439	186.15	3.0569

Table 3.7 Projection Parameters for ALSM. Source 3001© Area 2 Data Quality Report.

Description	NAD 27	NAD 83
Map Units	Feet	Feet
Distance Units	Feet	Feet
Standard Projection	SP 27 - Florida - East	SP 83 – Florida East
Custom Projection	Transverse Mercator	UTM
Central Meridian	81 00 00	81 00 00
Latitude of Orgin	24.3333	24.3333
Scale Factor	0.999942	0.999917
False Easting	500,000	200,000
False Northing	0	0

Table 3.8 Universal kriging search parameters for SWEM.

Test Id	Global	Local	Angle Direction	Angle Tolerance	Nugget
1	20	80	15	45	0.011617
2	20	80	30	45	0.011617
3	30	70	30	45	0.017298
4	30	70	20	35	0.017298
5	30	70	0	30	0.017298
6	25	75	10	30	0.013573
7	25	75	20	30	0.013573
8	35	65	20	30	0.014003
9	40	60	10	30	0.007041
10	40	60	10	30	0.007041
11	45	55	25	30	0.000000
12	50	50	15	35	0.000000
13	55	45	15	35	0.000000
14	60	40	15	35	0.000000
15	65	35	15	35	0.000000

Table 3.8 Conyinned

Test Id	Major Range	Minor Range	Angle Direction	Partial Sill	Shape	Shape Angle	Z Prediction Value ft.
1	30332	23242	13.2	0.0081215	3	20	3.3100
2	30332	23242	13.2	0.0081215	2	15	3.3554
3	30453	24640	8.9	0.0151810	1	15	3.2981
4	30453	24640	8.9	0.0151810	4	25	3.3312
5	30453	24640	8.9	0.0151810	3	10	3.3214
6	30550	23285	13.3	0.0114650	3	10	3.3160
7	30550	23285	13.3	0.0114650	3	30	3.3245
8	30415	24626	11.8	0.0376450	3	15	3.1673
9	30526	25812	13.7	0.0774980	3	15	3.0834
10	30526	25812	13.7	0.0774980	3	30	3.0761
11	30569	25809	14.8	0.1291700	4	30	3.0526
12	30526	25864	15.7	0.1818600	3	15	3.0551
13	30628	25859	15.7	0.2500900	3	15	3.0550
14	30586	25890	14.9	0.3312100	3	15	3.0550
15	30668	25892	14.7	0.4212600	3	15	3.0549

Table 3.9 Simple kriging search parameters for SWEM.

Test Id	Angle Direction	Angle Tolerance	Shape	Shape Angle	Neighbors	Z Prediction Value ft.
1	0	35	1	30	5	3.3499
2	0	35	2	30	10	3.3380
3	0	35	3	30	9	3.3382
4	0	35	4	30	10	3.3380
5	15	35	1	30	10	3.3499
6	15	35	2	30	10	3.3380
7	15	35	3	30	9	3.3382
8	15	35	4	30	10	3.3380
9	15	35	1	20	5	3.3460
10	15	35	2	20	10	3.3380
11	15	35	3	20	8	3.3520
12	15	35	4	20	10	3.3380
13	15	35	1	10	5	3.3460
14	15	35	2	10	9	3.3500
15	15	35	3	10	8	3.3520
16	15	35	4	10	10	3.3380
17	20	50	1	15	5	3.3459
18	20	50	2	15	9	3.3459
19	20	50	3	15	8	3.3520
20	20	50	4	15	10	3.3380
21	20	50	1	35	5	3.3499
22	20	50	2	35	10	3.3380
23	20	50	3	35	9	3.3382
24	20	50	4	35	10	3.3380
25	15	35	1	20	5	3.3459
26	15	35	2	20	10	3.3380
27	15	35	3	20	8	3.3520
28	15	35	4	20	10	3.3380

Table 3.10 Ordinary Kriging search parameters for SWEM.

Test Id	Angle Direction	Angle Tolerance	Shape	Shape Angle	Neighbors	Z Prediction Value ft.
1	15	45	1	15	5	3.0799
2	15	45	2	15	9	3.0588
3	15	45	3	15	8	3.0551
4	15	45	4	15	10	3.0532
5	15	45	1	20	5	3.0799
6	15	45	2	20	10	3.0532
7	15	45	3	20	8	3.0551
8	15	45	4	20	10	3.0532
9	15	45	1	15	5	3.0799
10	15	45	2	15	9	3.0588
11	15	45	3	15	8	3.0551
12	15	45	4	15	10	3.0532
13	15	45	1	25	5	3.0799
14	15	45	2	25	10	3.0532
15	15	45	3	25	8	3.0551
16	15	45	4	25	10	3.0532
17	20	70	1	25	5	3.0799
18	20	70	2	25	10	3.0532
19	20	70	3	25	8	3.0551
20	20	70	4	25	10	3.0532
21	20	35	1	25	5	3.0799
22	20	35	2	25	10	3.0532
23	20	35	3	25	8	3.0551
24	20	35	4	25	10	3.0532
25	20	35	1	10	5	3.0799
26	20	35	2	10	9	3.0588
27	20	35	3	10	8	3.0551
28	20	35	4	10	10	3.0532
29	10	60	1	15	5	3.0799
30	10	60	2	15	9	3.0588
31	10	60	3	15	8	3.0551
32	10	60	4	15	10	3.0532
33	10	50	1	15	5	3.0799
34	10	50	2	15	9	3.0588
35	10	50	3	15	8	3.0551
36	10	50	4	15	10	3.0532
37	10	50	1	15	5	3.0799
38	10	50	2	15	9	3.0588
39	10	50	3	15	8	3.0551
40	10	50	4	15	10	3.0532

Table 3.10 Continued

Test Id	Angle Direction	Angle Tolerance	Shape	Shape Angle	Neighbors	Z Prediction Value ft.
41	10	50	1	15	5	3.0799
42	10	50	2	15	9	3.0588
43	10	50	3	15	9	3.0551
44	10	50	4	15	10	3.0532
45	0	50	1	30	5	3.0757
46	0	50	2	30	10	3.0532
47	0	50	3	30	9	3.0488
48	0	50	4	30	10	3.0532
49	0	35	1	30	5	3.0757
50	0	35	2	30	10	3.0532
51	0	35	3	30	9	3.0488
52	0	35	4	30	10	3.0532

Table 3.11 Disjunctive kriging search parameters for SWEM. D in the column heading is the distribution, PD is probability distribution and CD is cumulative distribution.

Test Id	D	Angle Direction	Angle Tolerance	Shape	Shape Angle	Neighbors	Z Prediction Value ft.
1	PD	15	45	3	20	5	3.1977
2	PD	30	45	2	15	5	3.1977
3	PD	30	45	1	15	5	3.2058
4	PD	20	35	4	25	5	3.1977
5	PD	0	30	3	10	5	3.1977
6	PD	10	30	3	10	5	3.1977
7	PD	20	30	3	30	5	3.2058
8	PD	20	30	3	15	5	3.1977
9	PD	10	30	3	15	5	3.1977
10	PD	10	30	3	30	5	3.2058
11	PD	25	30	4	30	5	3.1977
12	PD	15	35	3	15	5	3.1977
13	CD	15	45	3	15	5	3.1029
14	CD	15	45	4	20	5	3.1977
15	CD	20	40	1	10	5	3.2058
16	CD	20	40	4	10	5	3.1977
17	CD	20	40	1	20	5	3.2058
18	CD	20	40	1	5	5	3.2058
19	CD	20	40	1	30	5	3.2058
20	CD	20	40	2	35	6	3.1977
21	CD	20	40	3	35	5	3.2058
22	CD	20	40	1	35	6	3.2058
23	CD	20	40	4	35	6	3.1977
24	CD	20	40	1	0	5	3.2009
25	CD	15	40	1	20	5	3.2058
26	CD	15	40	2	20	6	3.1977
27	CD	15	40	3	20	6	3.1977
28	CD	15	40	4	20	6	3.1977
29	CD	15	45	1	15	5	3.2058
30	CD	15	45	2	15	6	3.1977
31	CD	15	45	4	15	6	3.1977
32	CD	15	45	1	30	5	3.2058
33	CD	15	45	2	30	6	3.1977
34	CD	15	45	3	30	5	3.2058
35	CD	15	45	1	10	5	3.2058
36	CD	15	45	2	10	6	3.1977
37	CD	15	45	3	10	6	3.1977
38	CD	15	45	4	10	6	3.1977
39	CD	15	45	1	20	5	3.2058
40	CD	15	45	2	20	6	3.1977
41	CD	15	45	3	20	6	3.1977

Table 3.11 Continued

Test Id	D	Angle Direction	Angle Tolerance	Shape	Shape Angle	Neighbors	Z Prediction Value ft.
42	CD	15	45	4	20	6	3.1977
43	CD	15	45	1	10	5	3.2058
44	CD	15	45	2	10	6	3.1977
45	CD	15	45	3	10	6	3.1977
46	CD	15	45	4	10	6	3.1977
47	CD	15	45	4	20	6	3.1977
48	CD	15	45	3	20	6	3.1977
49	CD	15	45	2	20	6	3.1977
50	CD	15	45	1	20	5	3.2058

Table 3.12 Universal Kriging for SWEM, October 12-22, 1999. All values represent surface water interpolation for NAD 83 and NGVD 88.

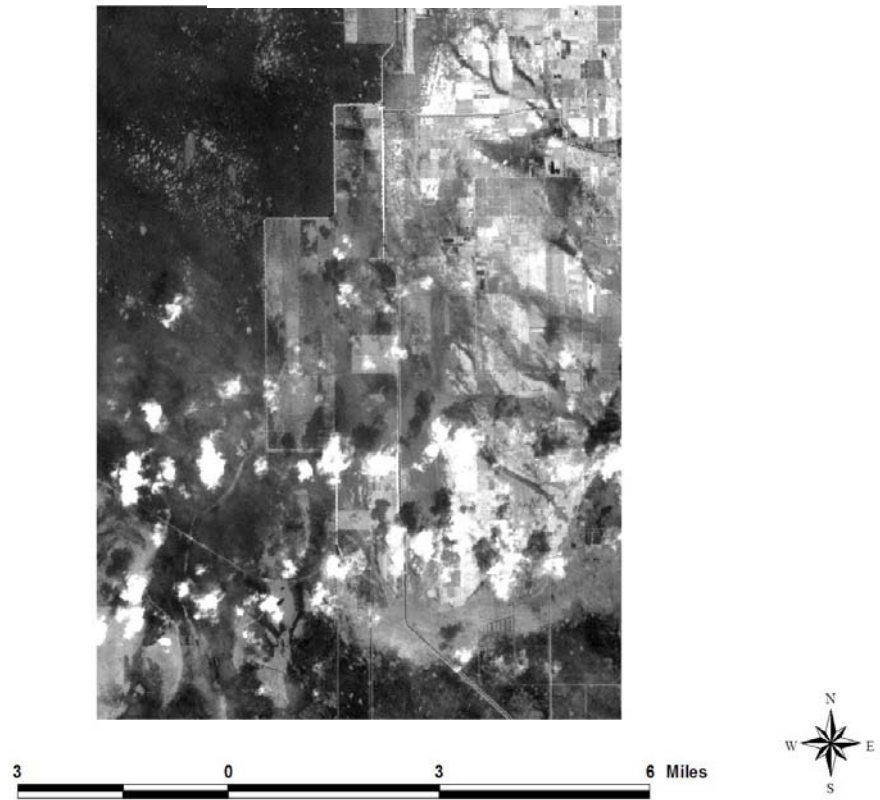
Day	Nugget ft.	Partial Sill ft.	Z Prediction Value ft.
10/12/1999	0.1965	0.32490	0.6102
10/13/1999	0.2296	0.30122	0.6224
10/14/1999	0.0000	0.61716	0.4183
10/15/1999	0.0000	0.54420	0.3928
10/16/1999	0.0000	0.42082	0.3454
10/17/1999	0.0000	0.35905	0.3190
10/18/1999	0.0000	0.33162	0.3037
10/19/1999	0.0000	0.36915	0.3235
10/20/1999	0.0000	0.35809	0.4177
10/21/1999	0.0426	0.43048	0.4304
10/22/1999	0.0049	0.54628	0.4031

## CHAPTER 4 RESULTS AND DISCUSSION

### **Cloud Detection**

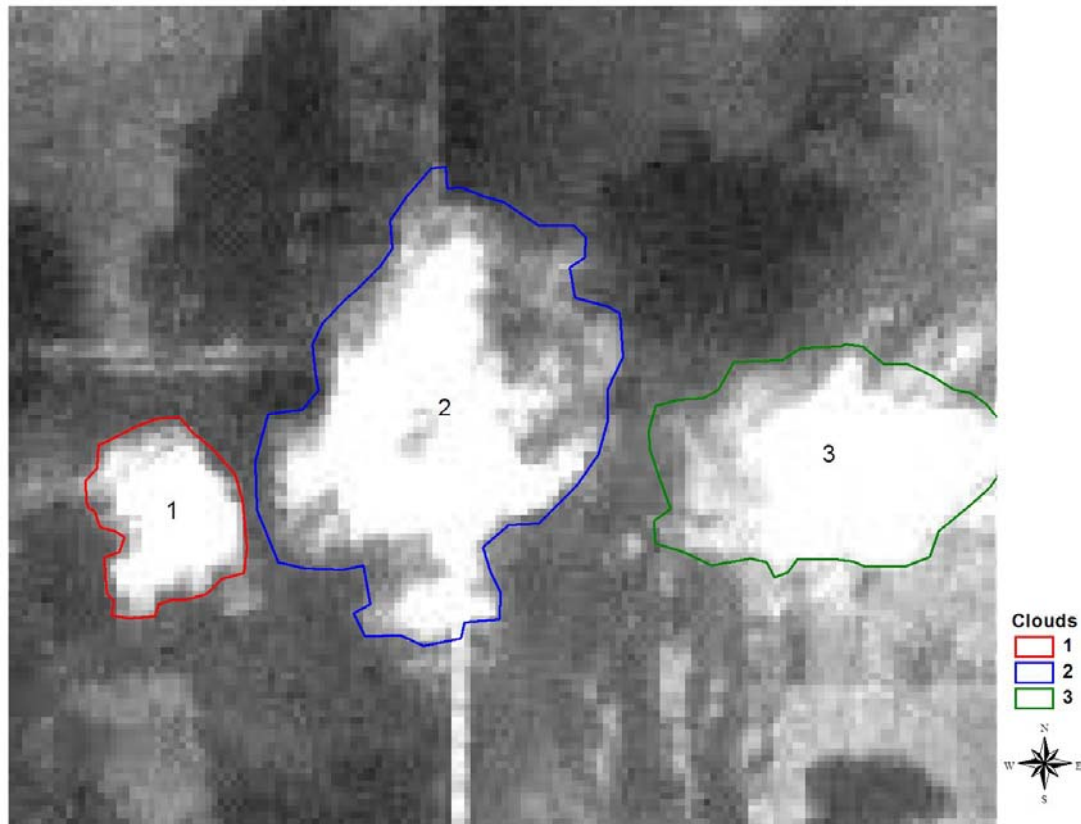
The initial step for flood analysis began with detecting clouds in the October 16, 1999, Landsat 7 ETM+ scene. Clouds can obstruct the spectral signature of water bodies, therefore clouds were mapped in the study area. Clouds found within Hurricane Irene were used as a reference feature to identify cloud classes in all maps of vegetative indices. Hurricane Irene is located in the north east quadrant of the October 16, 1999, Landsat 7 ETM+ scene. Vegetative index two, vegetative index three and Band 8 were used to map clouds in the study area. For an initial analysis, Band 8 was selected to identify clouds in the study area, because of its 15 meter spatial resolution. Clouds are clearly displayed as irregular shapes comprised of white pixels, and each cloud possesses a shadow located northwest of the cloud shape, Figure 4.1(A).

Three clouds are visible in the study area, however only two full cloud shadows are visible, Figure 4.1(B). Clouds in the study area were found to completely obstruct the ground signature and their shadows produced darker pixels on the land surface.



A

Figure 4.1 (A) Map of the Frog Pond with Band 8. Clouds appear as white irregular shaped features. (B) Zoom in of the study area with Band 8.



B

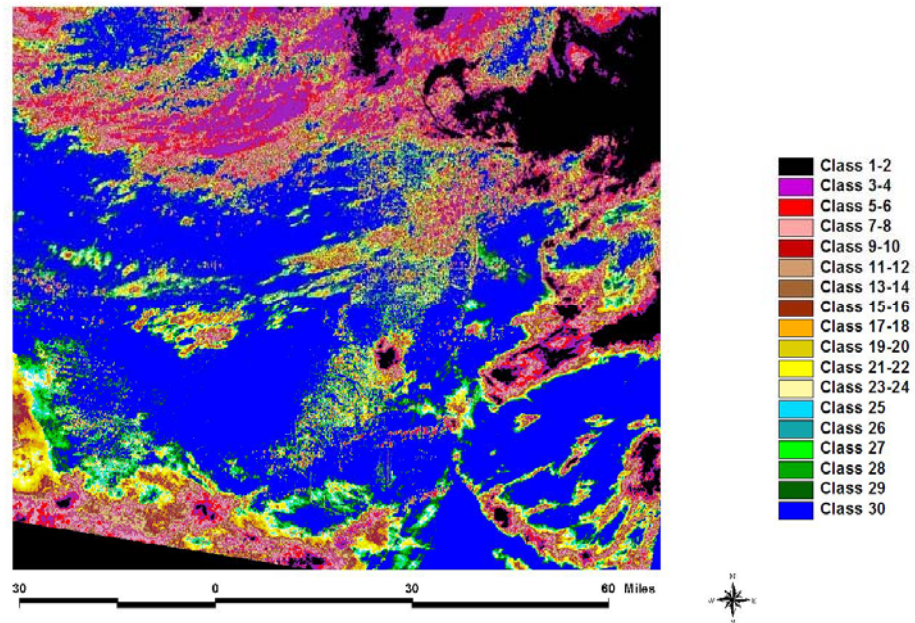
Figure 4.1

### Vegetation Index Two and Vegetation Index Three

Unsupervised classification of vegetation index two and vegetation index three were also used to detect dense clouds and verify clouds identified with Band 8. As with Band 8, the cloud formation of Hurricane Irene was used as the reference feature to identify potential cloud classes. The clouds from Hurricane Irene were located in the northeast quadrant of the vegetative index two and vegetative index three maps.

Classes 1-2 in vegetation index two were determined to be cloud classes and classes 3-8 were determined to be partial classes. Classes 3-7 were determined to be cloud classes in vegetation index three. Clouds that were identified with Band 8 in the study area produced similar but not exact shapes with vegetation index two and

vegetation index three. Vegetation index two uses more classes to map these clouds than vegetation index three, Figure 4.2(A) and Figure 4.2(B).



A

Figure 4.2(A) Vegetation index two map of south Florida, October 16, 1999. Clouds from Hurricane Irene are most visible in the northeast section with class 1 and class 2. (B) Vegetation index three map of south Florida, October 16, 1999. Clouds from Hurricane Irene are most visible in the northeast section with classes 3-7.

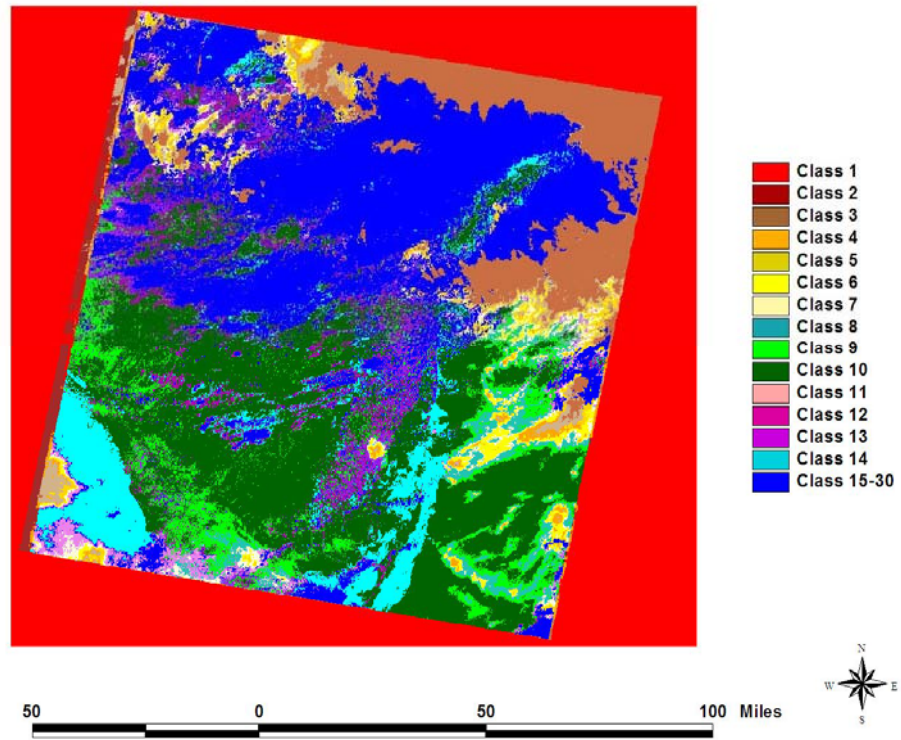
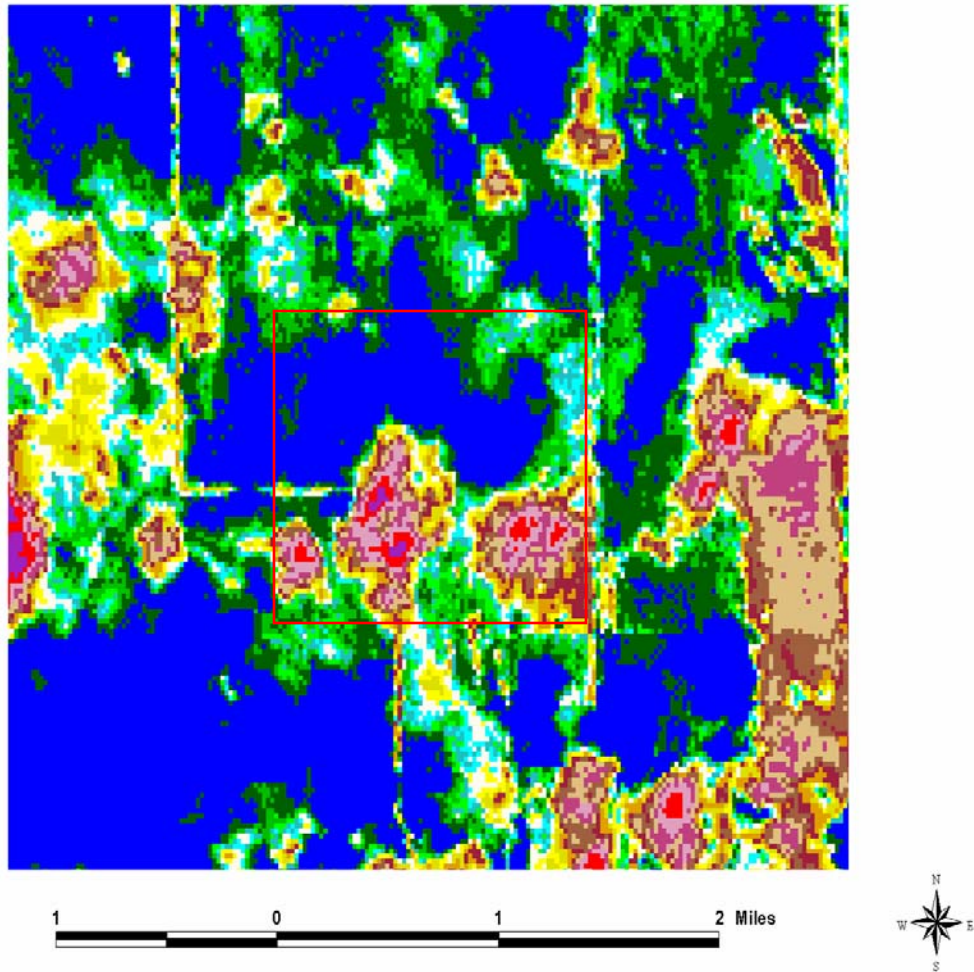


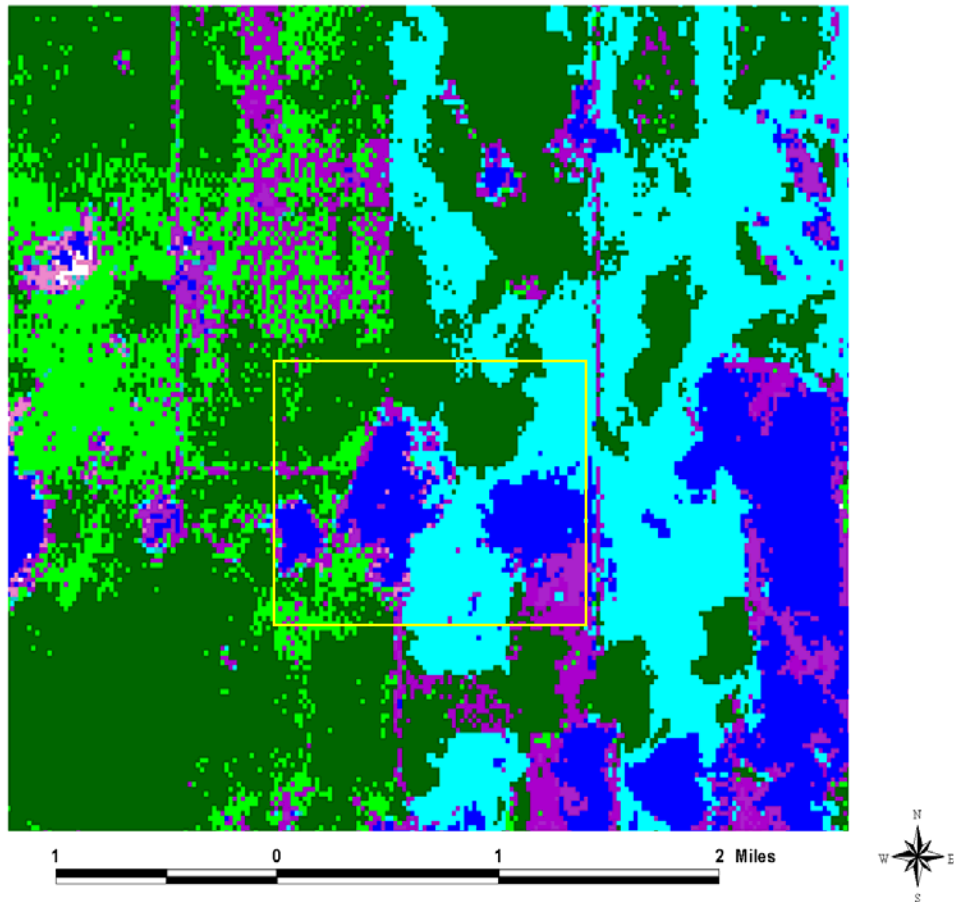
Figure 4.2

B



A

Figure 4.3(A) Vegetation index two map of the study area, October 16, 1999. All three clouds are visible in the study area outlined in red. The legend for Figure 4.2(A) applies to Figure 4.3(A). (B) Vegetation index three map of the study area, October 16, 1999. Clouds in the study area, outlined in yellow, are most visible with classes 15-30. The legend for Figure 4.2(B) applies to Figure 4.3(B).



B

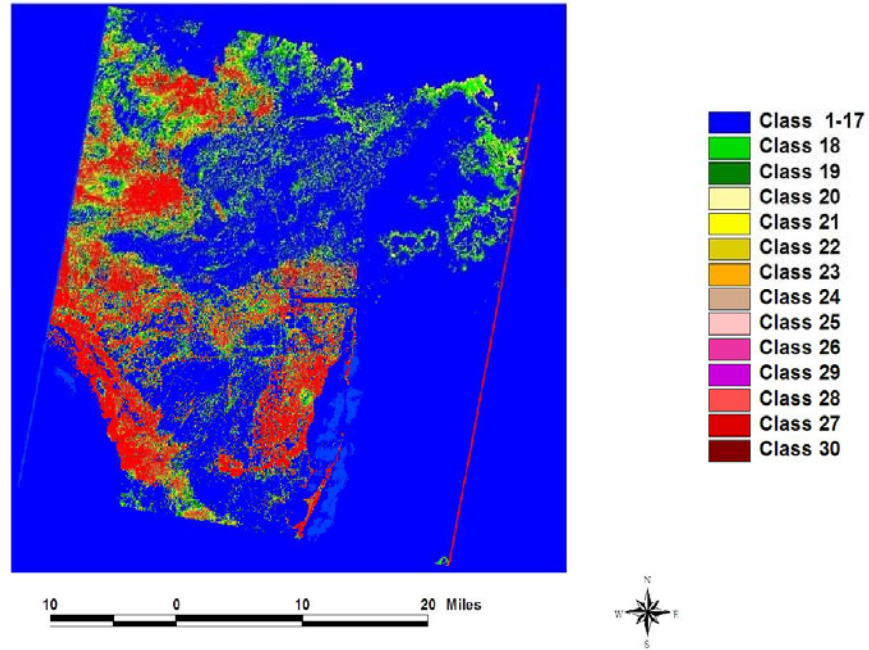
Figure 4.3

The analysis of vegetative index two and vegetative index three showed that the combination of high and low gain thermal bands was superior for mapping clouds. It is important to note that the lack of cloud cover displayed with vegetative index three could possibly lead to the incorrect assessment that clouds do not exist in the study area. To conclude, three clouds were located in the study area, and their signature completely dominated the signature of the ground, however it is inconclusive whether or not cloud shadows prevented water detection.

### NDVI

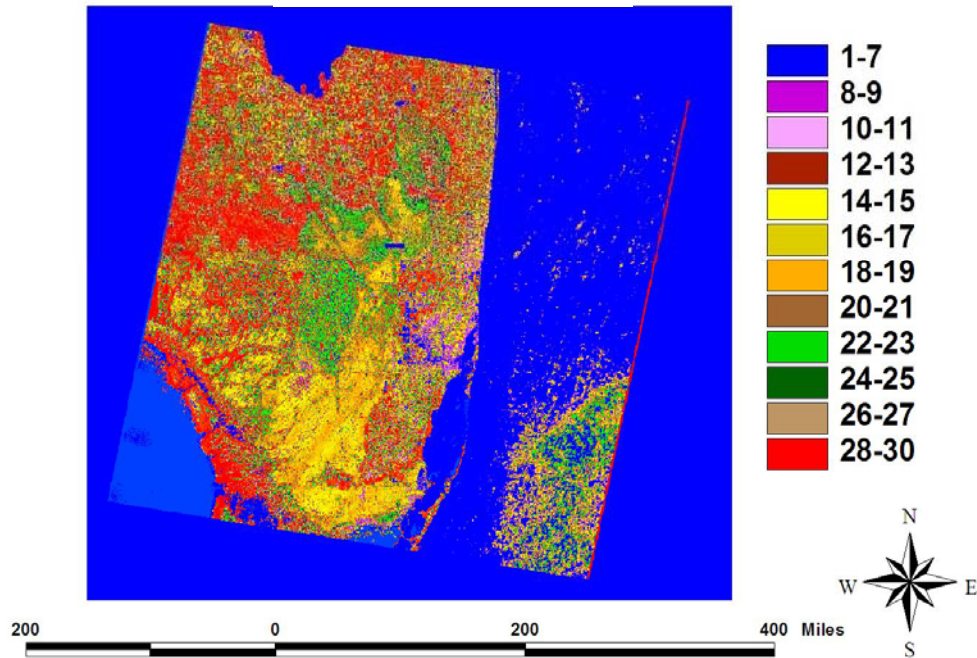
NDVI was useful for mapping water under both dry and severe flood conditions, and the Atlantic Ocean was the primary feature used to identify open water classes in

both NDVI maps. Open water represents a severely inundated condition where only the spectral signature of water is visible; however this may also represent a condition where emergent canopy does not exceed inundation depth. Atlantic Ocean open water classes were found to conform to the east coast of south Florida's peninsular land boundary. Open water classes were found to be clearly distinguishable and separated from land classes along the east coast boundary, Figure 4.4(A) and Figure 4.4(B).



A

Figure 4.4(A). October 16, 1999, NDVI map of the south Florida. Open water classes are represented with blue. (B). April 9, 2000, NDVI map of south Florida. Classes 1-7 are open water and represented with blue.



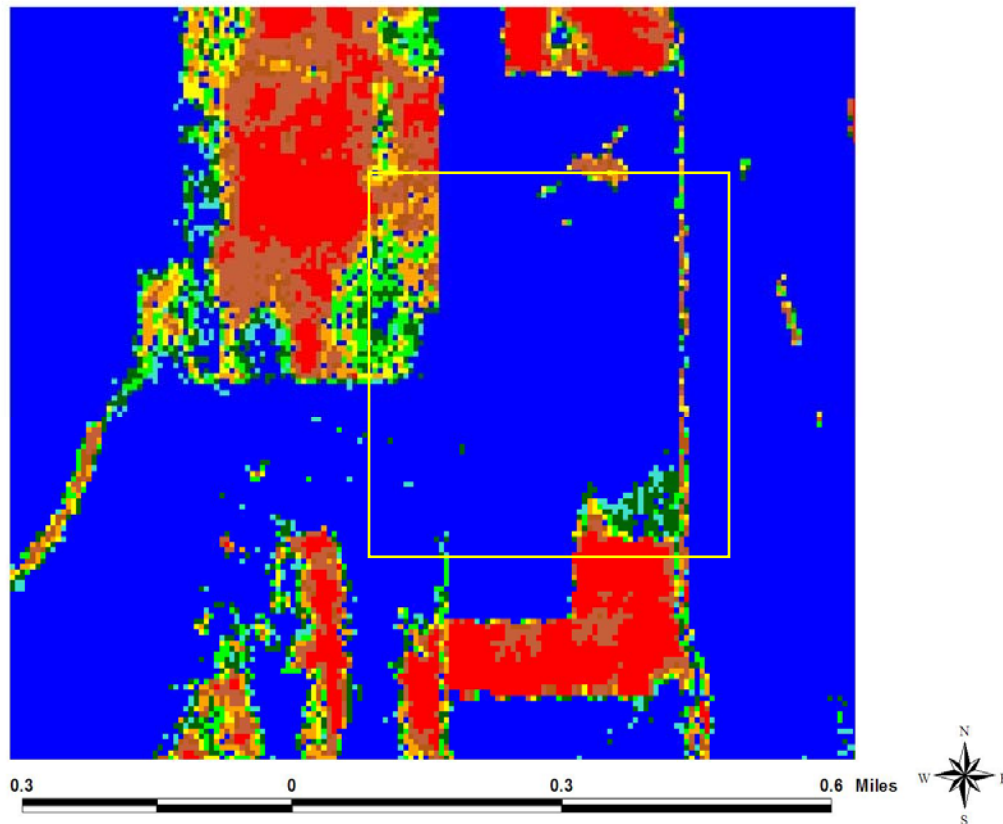
B

Figure 4.4

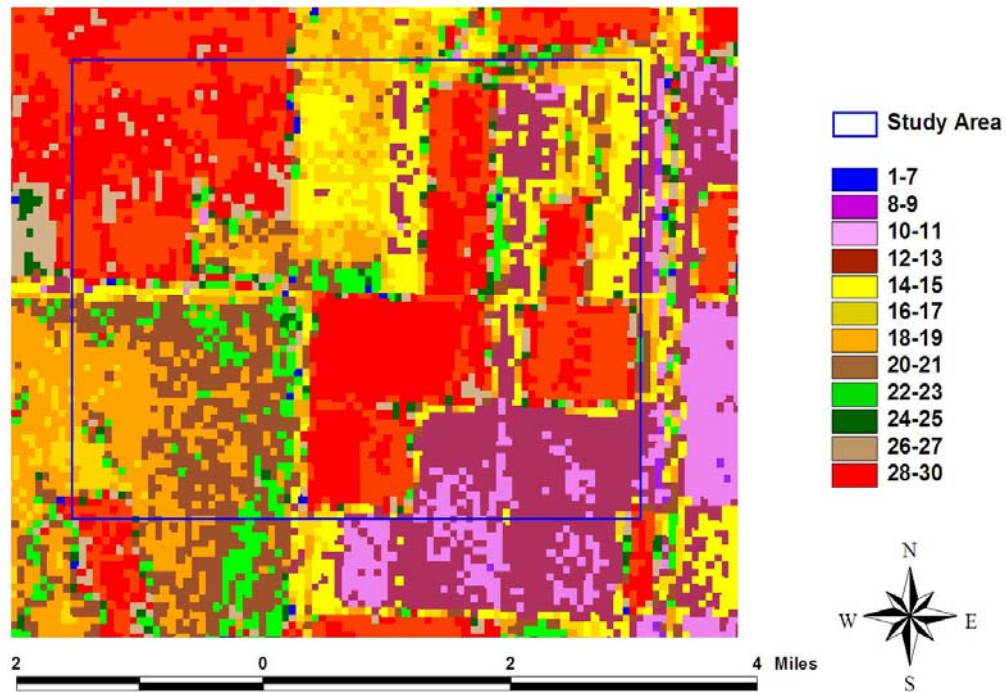
To identify and map water classes in the study area for October 16, 1999, and April 9, 2000, only the NDVI classes found in the Atlantic Ocean were used. The land boundary was clearly visible from open water in both images; however the increase of open water classes in the October 16, 1999, NDVI map showed the flood impact of Hurricane Irene.

Classes 1 -7 were determined to be open water in the April 9, 2000, NDVI map, and classes 1-17 were determined to be open water in the October 16, 1999, NDVI map. The October 16, 1999, NDVI map was expected to have more water classes due to the flood condition produced by Hurricane Irene. Figures 4.5(A) and Figure 4.5(B) display the coverage of water in the study area. Clouds from Hurricane are visible with classes 18-20; however clouds in the study area are not distinguishable with classes 18-20.

Because clouds are not be mapped in October 16, 1999, NDVI map, it is difficult to exactly determine the separation between open water and cloud pixels in the study area. The method used to determine an open water class was successful for separating clouds from water in the April 9, 2000, NDVI map; however this method is not adequate for separating clouds from water in the October 16, 1999, NDVI map. Despite this constraint, the October 16, 1999, NDVI map does display a large increase in the coverage of water classes that is not found in the April 9, 2000, NDVI map.



A  
 Figure 4.5(A). October 16, 1999, NDVI map of the study area outlined in yellow. Open water classes are represented with blue. (B). April 9, 2000, NDVI map of the study area outlined in blue. Open water classes 1-7 are represented with blue.



B

Figure 4.5

High NDVI classes in the October 16, 1999, NDVI map are found where the spectral signature of water is obstructed by the signature of canopy. These pixels were mostly found in areas where high and dense canopy exists. This is most visible in the wetland shrub/scrub areas and in the row crop areas where high NDVI class pixels are located adjacent to NDVI water pixels.

Although NDVI was determined to be useful for verifying the flood extent, several constraints became obvious during the analysis. First, the 30 meter spatial resolution of NDVI maps failed to distinguish vegetation from water where vegetation canopy exceeded ponded water depth. Second, clouds that were mapped with Band 8, vegetation index two and vegetation index three were not mapped with NDVI. Finally, NDVI maps

could not display the duration, change in magnitude and extent of flooding for Hurricane Irene, due to the low frequency of available Landsat 7 ETM+ images.

### **Topographic Analysis**

The procedure used to create bare earth topographic grids involved bare earth modeling and spatial modeling. Bare earth modeling initially began by identifying ALSM vegetation and artifact points with color infrared imagery and DEMs, and then the points were removed. Point removal was based under the assumption that the topography in the C-111 basin is extremely flat and that a low variability exists between neighborhood elevation points. Spatial modeling was employed to predict elevation values where large gaps were left from ALSM point removal. The spatial modeling procedure involved the use of multiple interpolators and assessment of the generated statistics. The optimum interpolation method was used to create both NAD 27 and NAD 83 ALSM DEMs.

The four deterministic interpolators that were used to create ALSM elevation grid surfaces are inverse distance weighting, global polynomial, local polynomial and radial based functions. The lowest root mean square value was used as the decision statistic for selecting the optimum test method, however several tests were found to possess the lowest value. To resolve this problem, the test that possessed a mean absolute error closest to zero was selected as the optimum method.

The radial based function interpolator produced the overall lowest root mean square error values, and was selected as the best interpolation method for ALSM DEMs, Table 4.1. Tests 3, 12, 13 and 16 all produced the lowest root mean square value, 0.1351 ft., therefore the lowest mean error statistic among these tests was used to select the optimum search parameters. Because of its low mean error value, test 13 was selected as the

optimum search parameter method for NAD 27 and NAD 83 ALSM data. Details for the other interpolators may be found in Tables 4.2, 4.3 and 4.4.

The search parameters for test 13 were applied to ordinary kriging, universal kriging, disjunctive kriging and simple kriging interpolators. Simple kriging produced the lowest root mean square value, 0.1433 ft., Table 4.5. Although geo-statistical interpolators are more rigorous than deterministic interpolators, they are not ideal for predicting topographic grids that possess a significant variability in density with ALSM points (ESRI 2001). Furthermore, the high variation in point density within the DEM made analysis and interpretation of semi-variograms inconclusive.

### **Classified ALSM DEM**

Classified ALSM DEMs were manually created by assigning elevation values into a specified interval. An elevation interval of 0.2 ft. was used to separate vegetation from the bare ground between the elevations of 4-6 ft. for NAD 27. The legend for elevation in Figure 4.6(A) describes elevation intervals in feet. Elevation intervals that were above the maximum elevation threshold of 4.8 ft. were represented with green, to represent vegetation. Three dimensional images of classified NAD 27 and NAD 83 DEMs were used to analyze the effect of point removal, Figure 4.6(A)-(H). The classified TIN DEM clearly displayed field vegetation, fiducial features and the S175 culvert. Except for part of the L31W canal, the NAD 83 classified TIN DEM did not map these features. This is attributed to large gaps produced by point removal. The three dimensional views of the NAD 83 DEM in Figures 4.6 (E-H) show the effect of point removal.

It is interesting to note that both NAD 27 DEMs show extremely false low elevation values east of the L31 W canal. This may be caused by scattering of the infrared laser beam, or a problem with post processing. Both NAD 27 DEMs also display

extremely high elevation values that are not characteristic of the topography in the study area, and this was likely caused by the laser beam striking an object in the atmosphere.

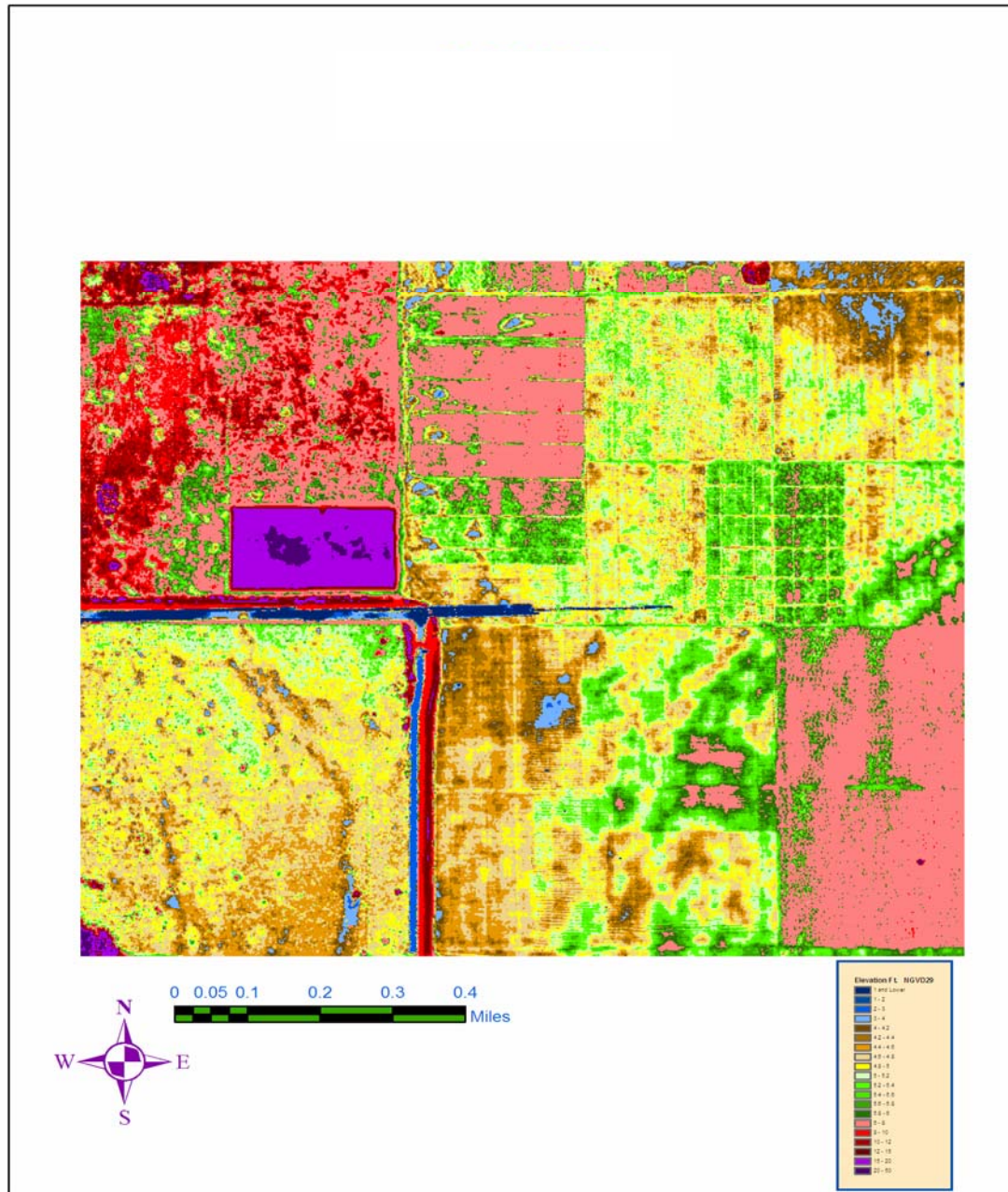


Figure 4.6(A) Planar view of the NAD 27 study area DEM. The legend applies to all three dimensional (3D) DEMs. (B) 3D southeasterly view of the study area using NAD 27 ALSM data. (C) 3D southerly view of the study area using NAD 27 ALSM data. (D) 3D westerly view of the study area using NAD 27 ALSM data. (E) 3D southerly view of the study area using NAD 83 ALSM data. (F) 3D easterly view of the study area using NAD 83 ALSM data. (G)

3D easterly view of the study area using NAD 83 ALSM data. (H) 3D westerly view of the study area using ALSM data.

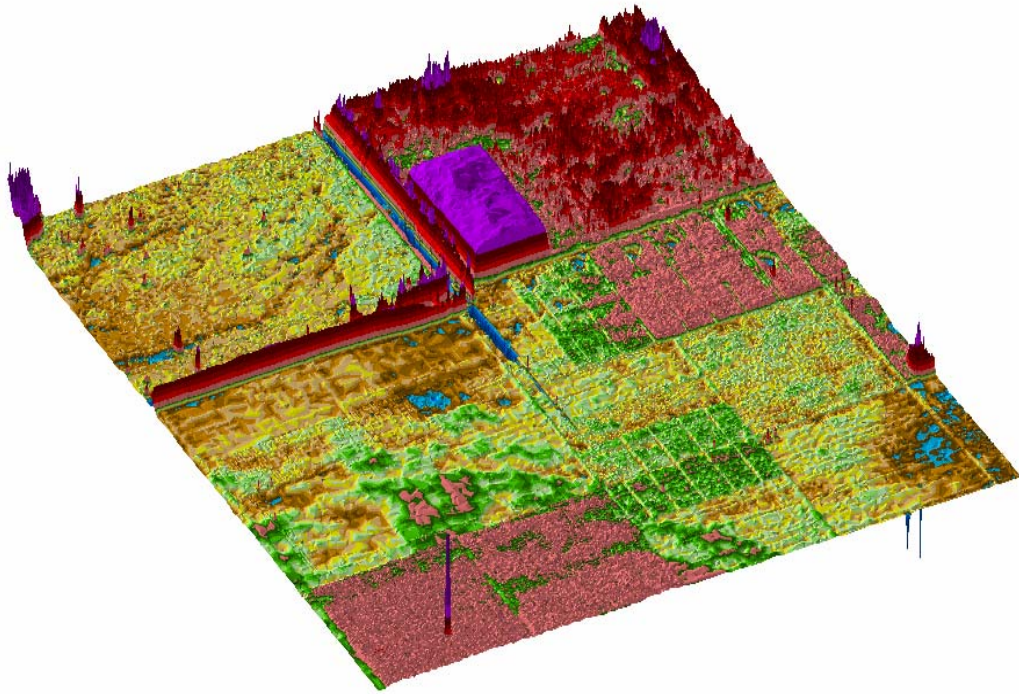


Figure 4.6

B

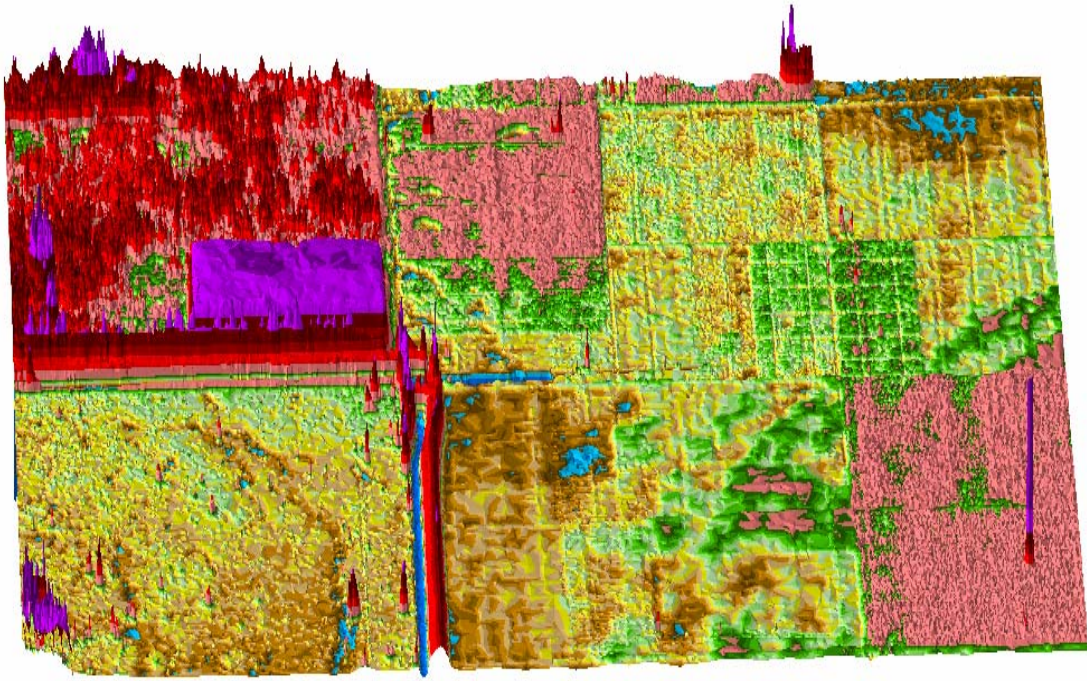


Figure 4.6

C

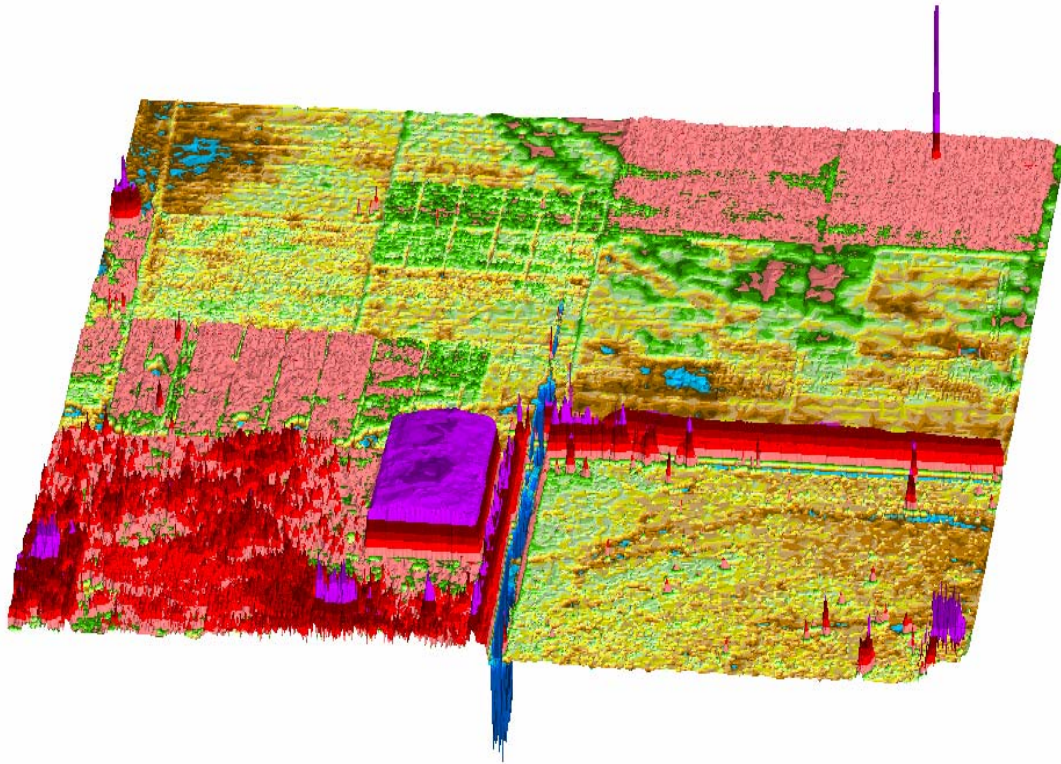


Figure 4.6

D

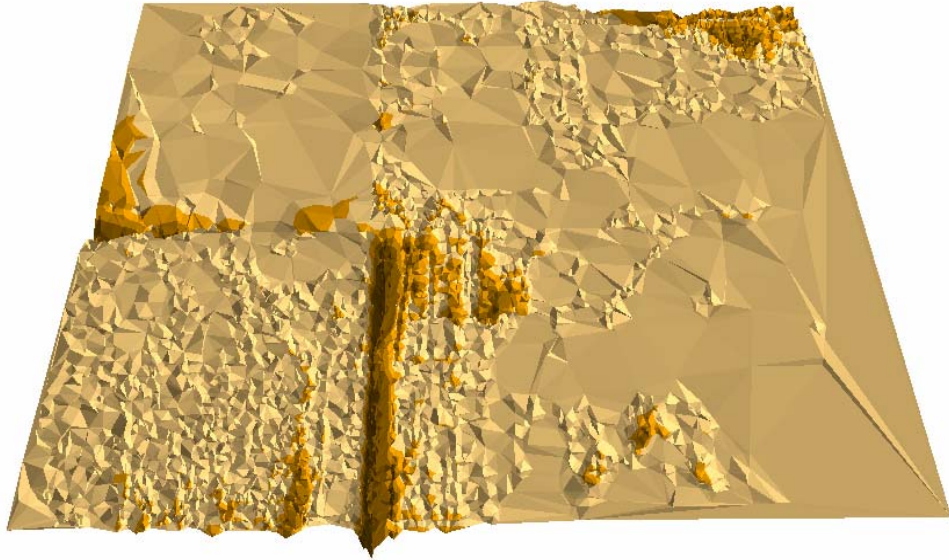


Figure 4.6

E

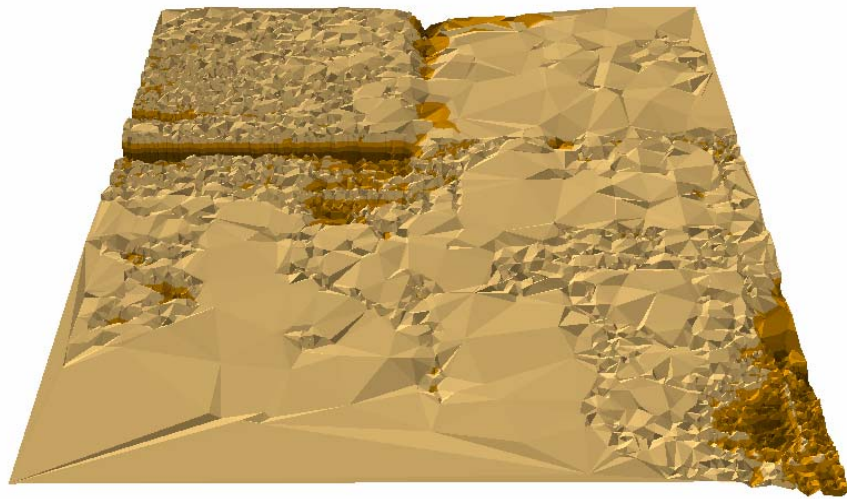


Figure 4.6

F

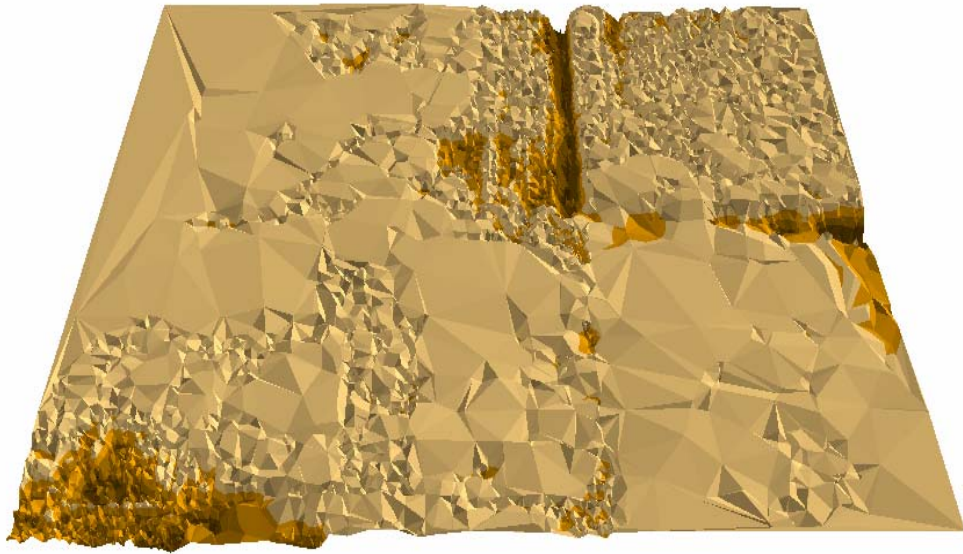
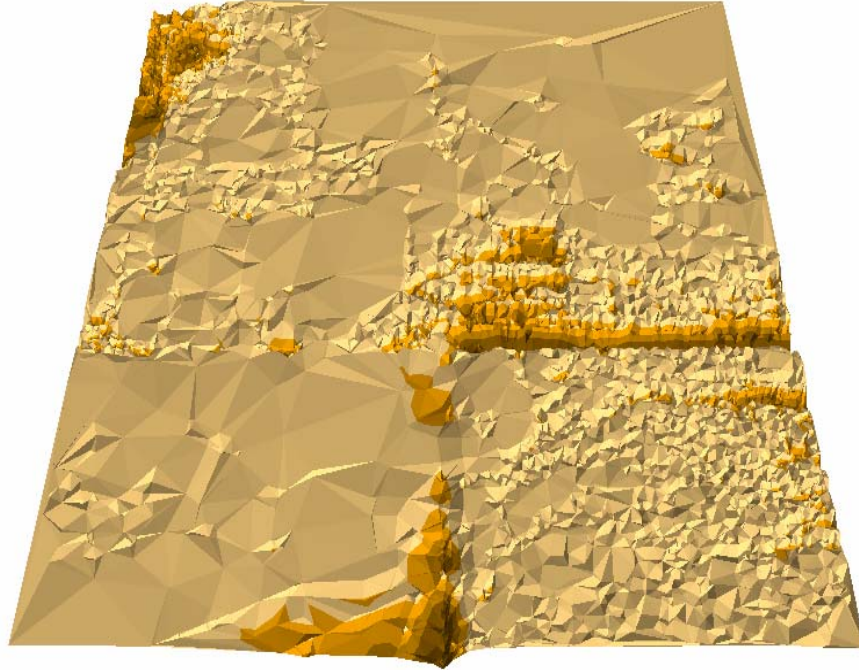


Figure 4.6

G



H

Figure 4.6

### **Surface Water Elevation Map Analysis**

The four geo-statistical interpolators that were used to predict elevation values for surface water elevation grids are universal kriging, disjunctive kriging, simple kriging and ordinary kriging. The root mean square error served as the decision statistic for selection of the optimum interpolation method. If two tests shared an equal value, then the test with the mean error value closest to zero was selected as the optimum method.

For universal kriging, test 15 produced the overall lowest root mean square error value of 0.4701 ft. (see Table 4.6), and the search parameters for test 15 were applied to create all surface water elevation maps, Table 4.7. These parameters were also used for October 16, 1999, NAD 27 surface water elevation data; however the root mean square error value was 0.02 ft. greater than that of NAD 83. Furthermore, NAD 27 possessed

greater mean error and mean error values; however the root mean square standardized error and average standard error values for NAD 27 were less than NAD 83. Details for the other interpolators are shown in Tables 4.8, 4.9 and 4.10.

Table 4.11 lists the surface water elevation values for the study period, and Figure 4.7 shows a graph of surface water elevation data for the study period. An analysis of surface water data showed a sharp increase in elevation that was coincident with the impact of Hurricane Irene, and a gradual decrease associated with drainage. SWEM contours in Figures (A-H) appear to show a directional flow towards the S332 and S178 pumping stations. The SFWMD (2000) reported that the S332 was operating at maximum capacity on October 14, 1999, however no specific information is provided for the other water control structures in the study area. Surface water elevation maps displayed a smooth transition between contour intervals; however discontinuities in the elevation intervals were more noticeable as the distance between stations increased, Figure 4.8 (A-K). Elevation values are in feet NGVD 88.

Prediction error maps for SWEM were produced, because universal kriging was selected as the interpolation method. Figure 4.9 (A-K) show universal kriging prediction error maps made from surface water elevation maps. Several trends were noticed during the production of SWEM prediction error maps. October 16, 1999 displayed the lowest prediction error, and an increase in prediction error existed for the remainder of the study period. Furthermore, SWEM prediction error for October 12, 1999, was observed to be the highest for the entire study period. Prediction error values are in feet.

The low prediction error for October 16, 1999, is attributed to both high surface water elevation values and the low variability in values for stations throughout the study

area. The increase in prediction error coincides with an increase in the variability in elevation values between neighboring stations. This increase in variability is most likely due to the effect of water management and variable drainage rates for water control structures.

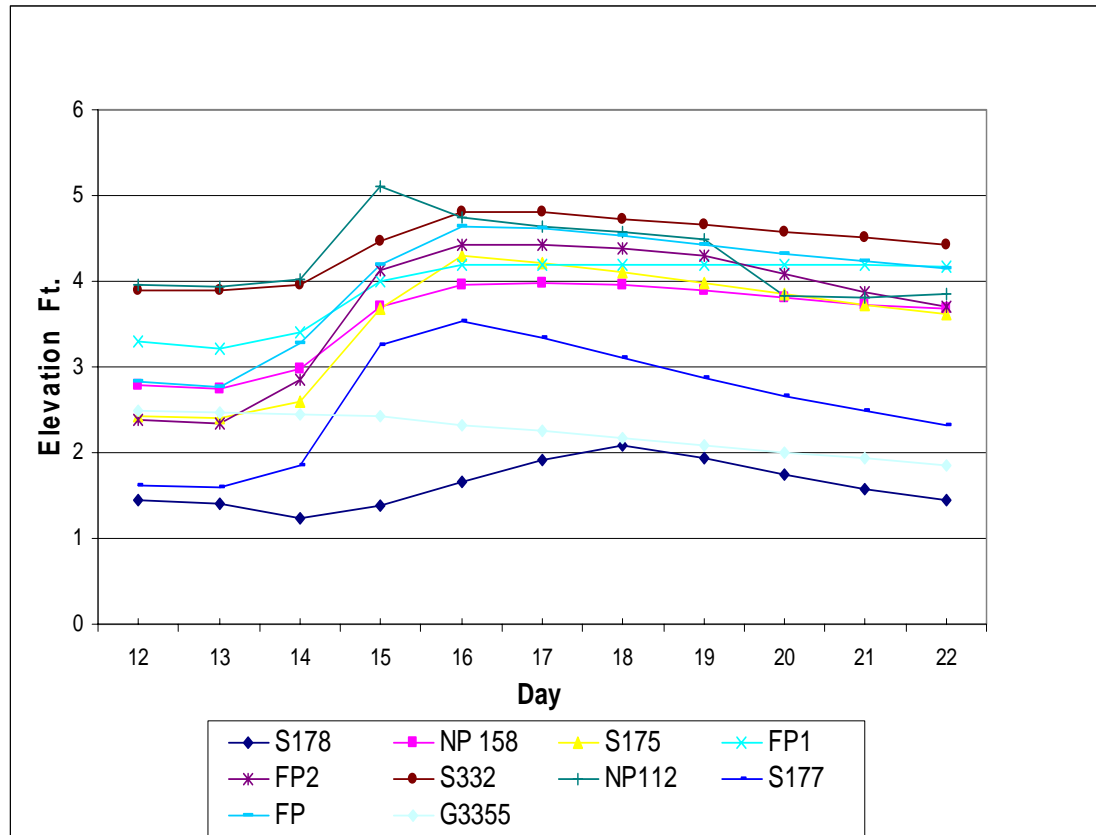


Figure 4.7 Graph of surface water elevation values. Values are in feet NGVD 88.

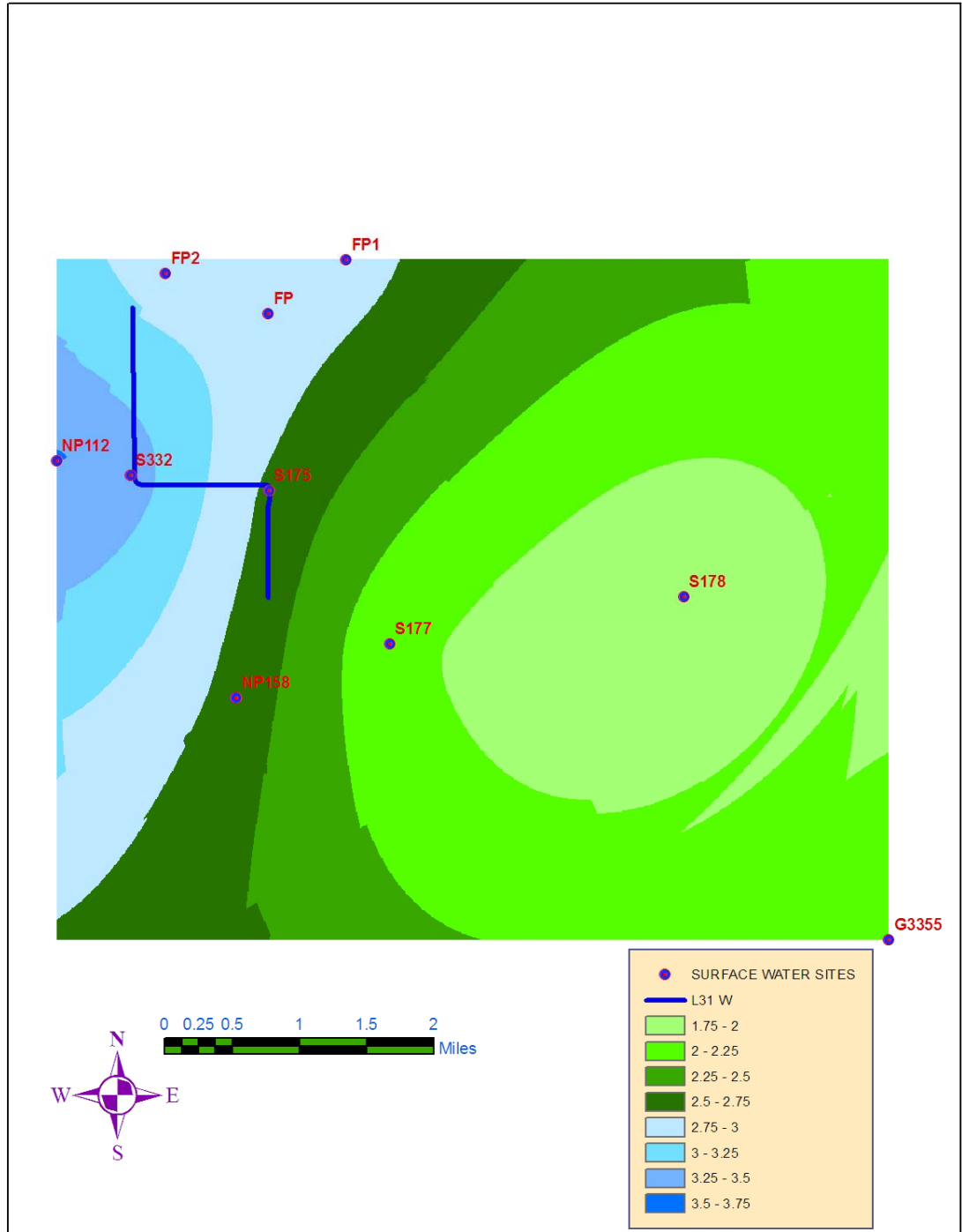


Figure 4.8 (A) SWEM October 12, 1999. (B) SWEM October 13, 1999. (C) SWEM October 14, 1999. (D) SWEM October 15, 1999. (E) SWEM October 16, 1999. (F) SWEM October 17, 1999. (G) SWEM October 18, 1999. (H) SWEM October 19, 1999. (I) SWEM October 20, 1999. (J) SWEM October 21, 1999. (K) SWEM October 22, 1999. Elevation values are in feet NGVD 88.

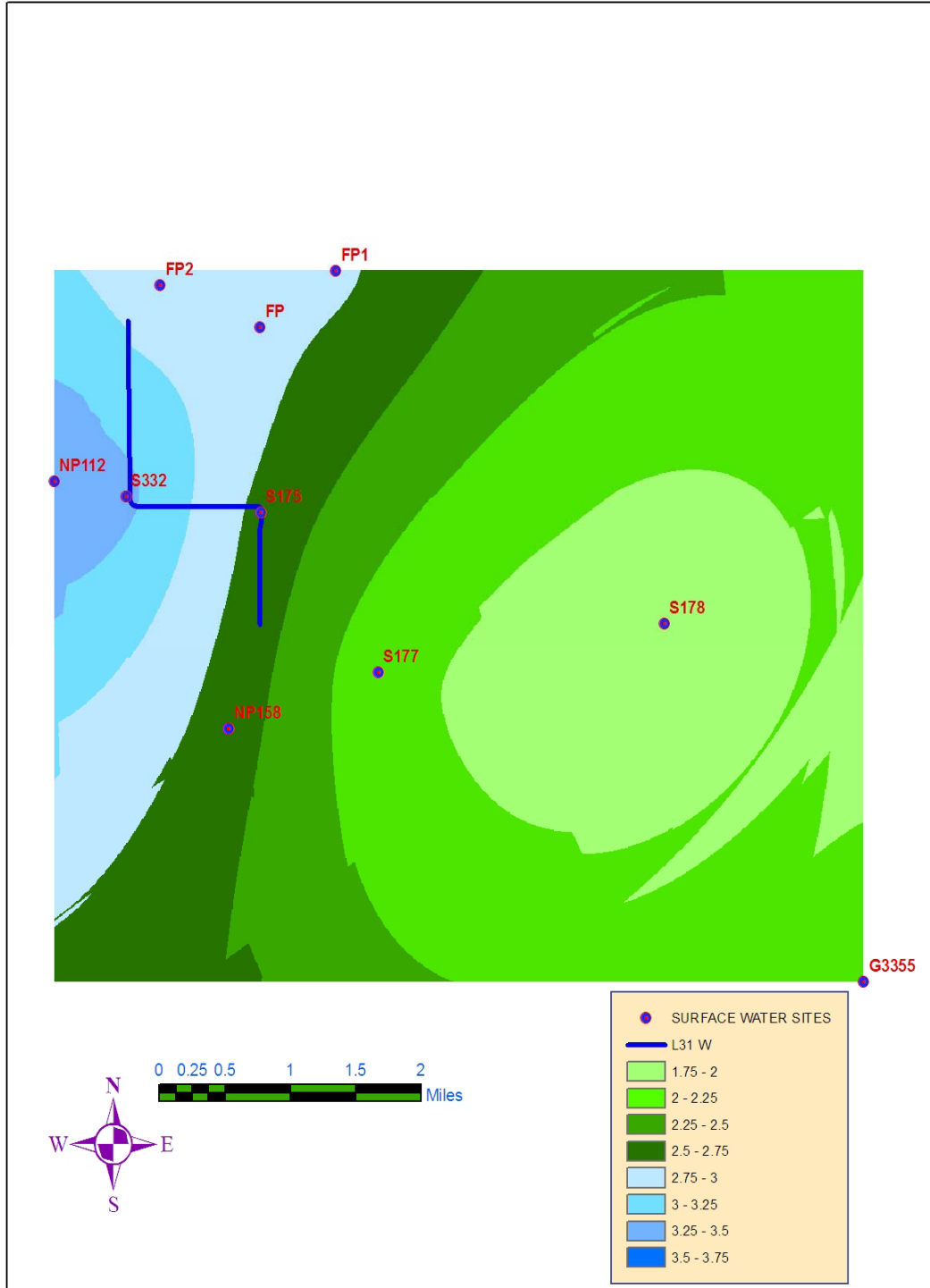


Figure 4.8

B

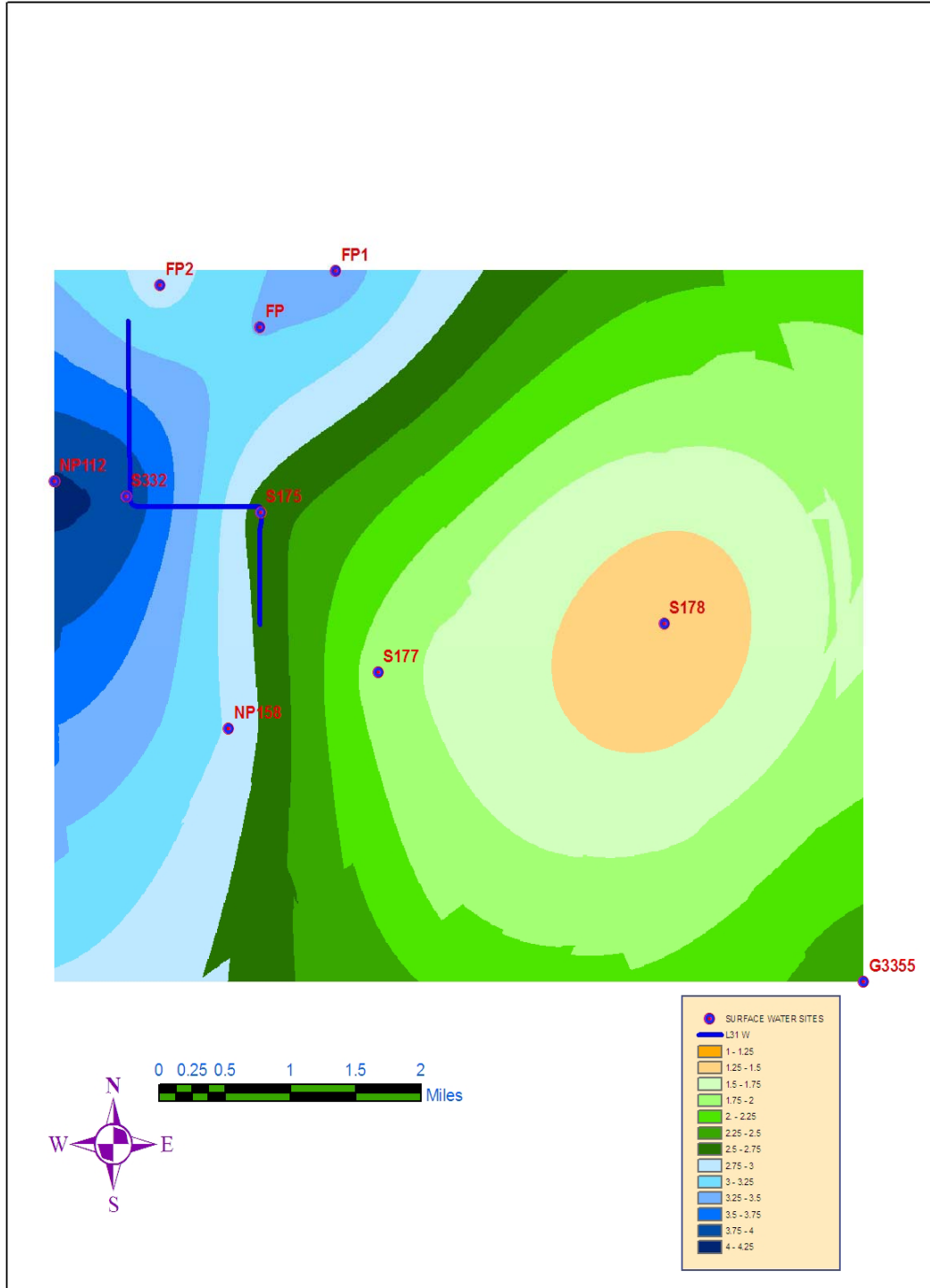


Figure 4.8

C

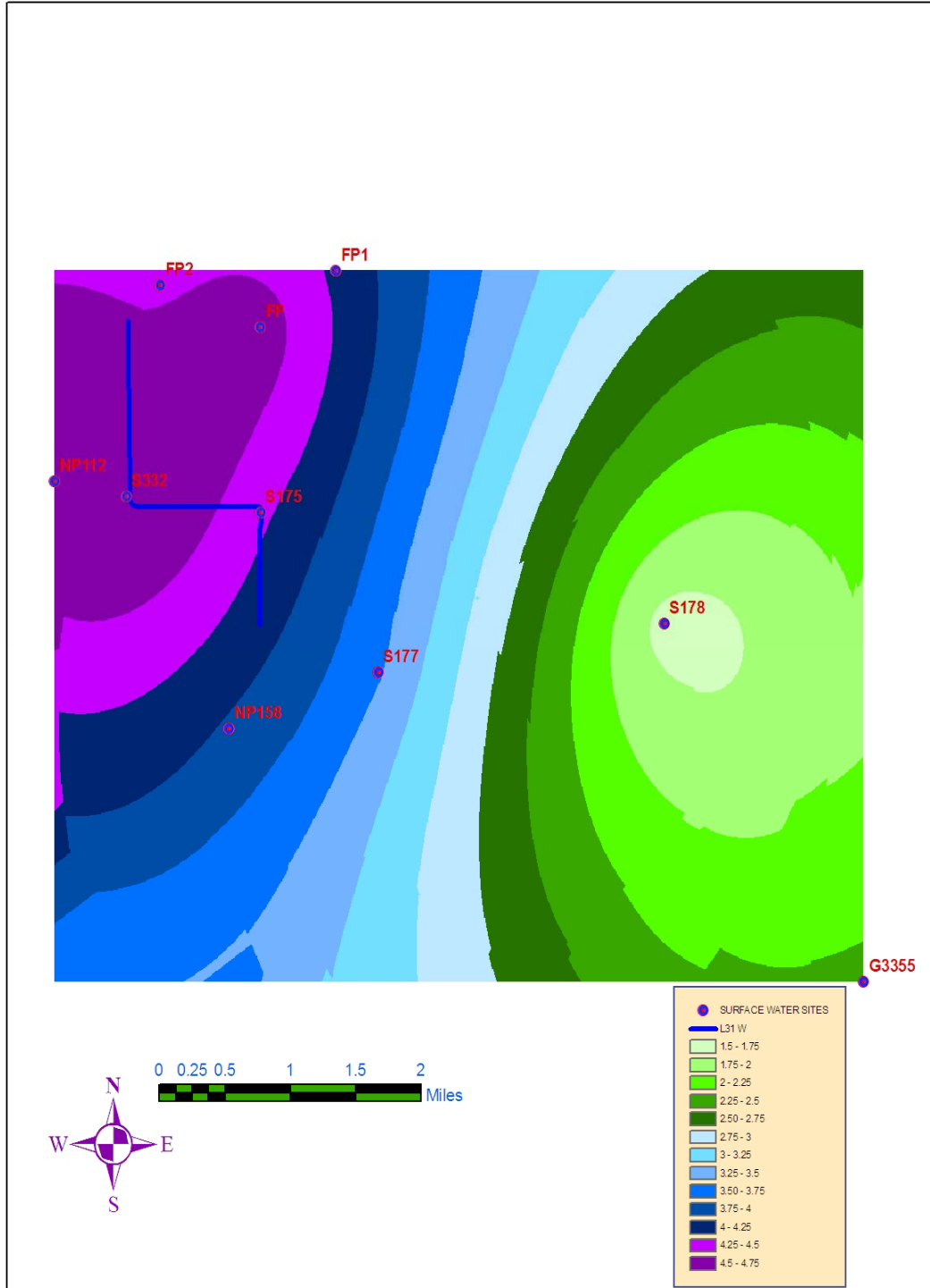


Figure 4.8

D

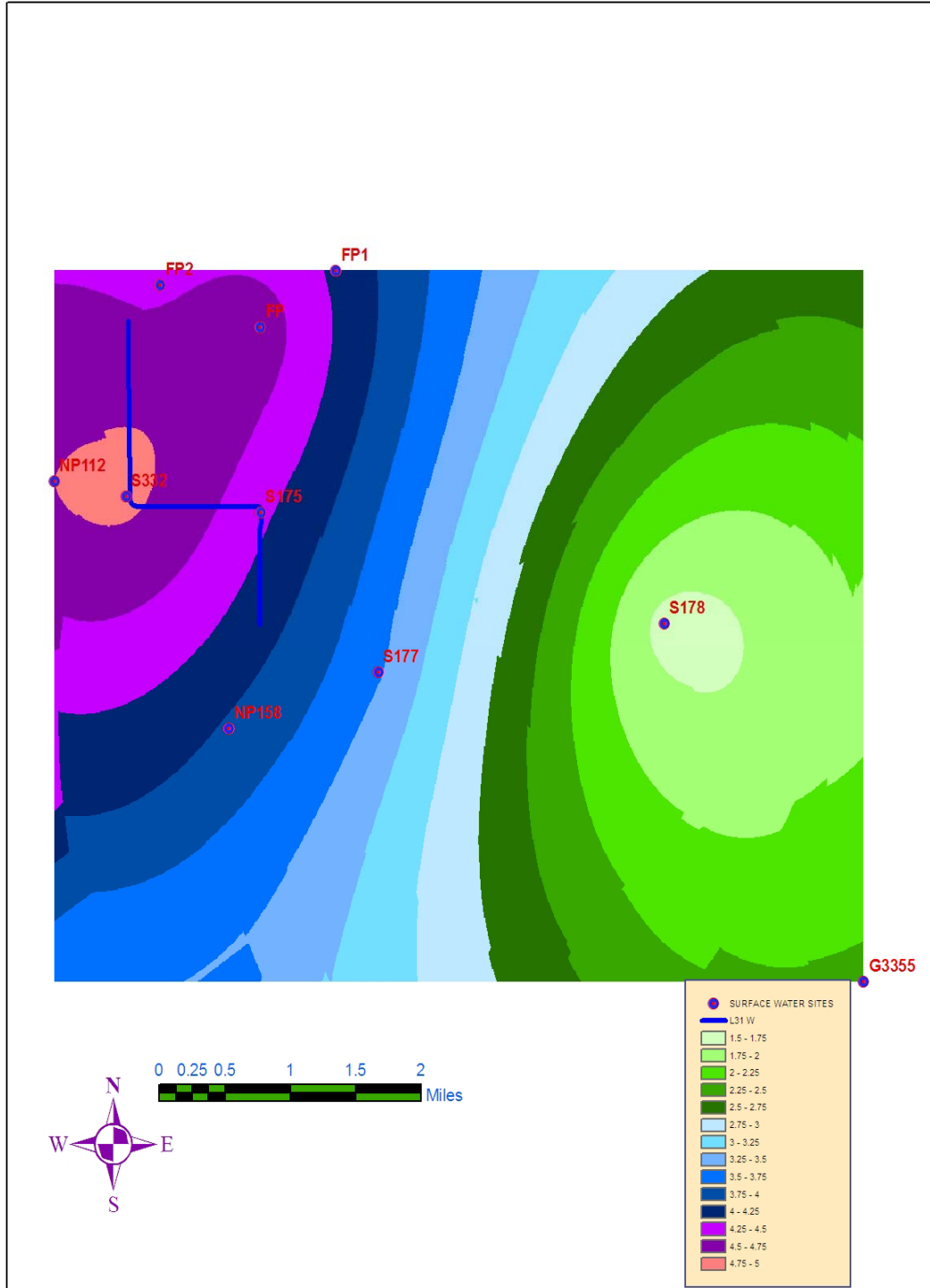
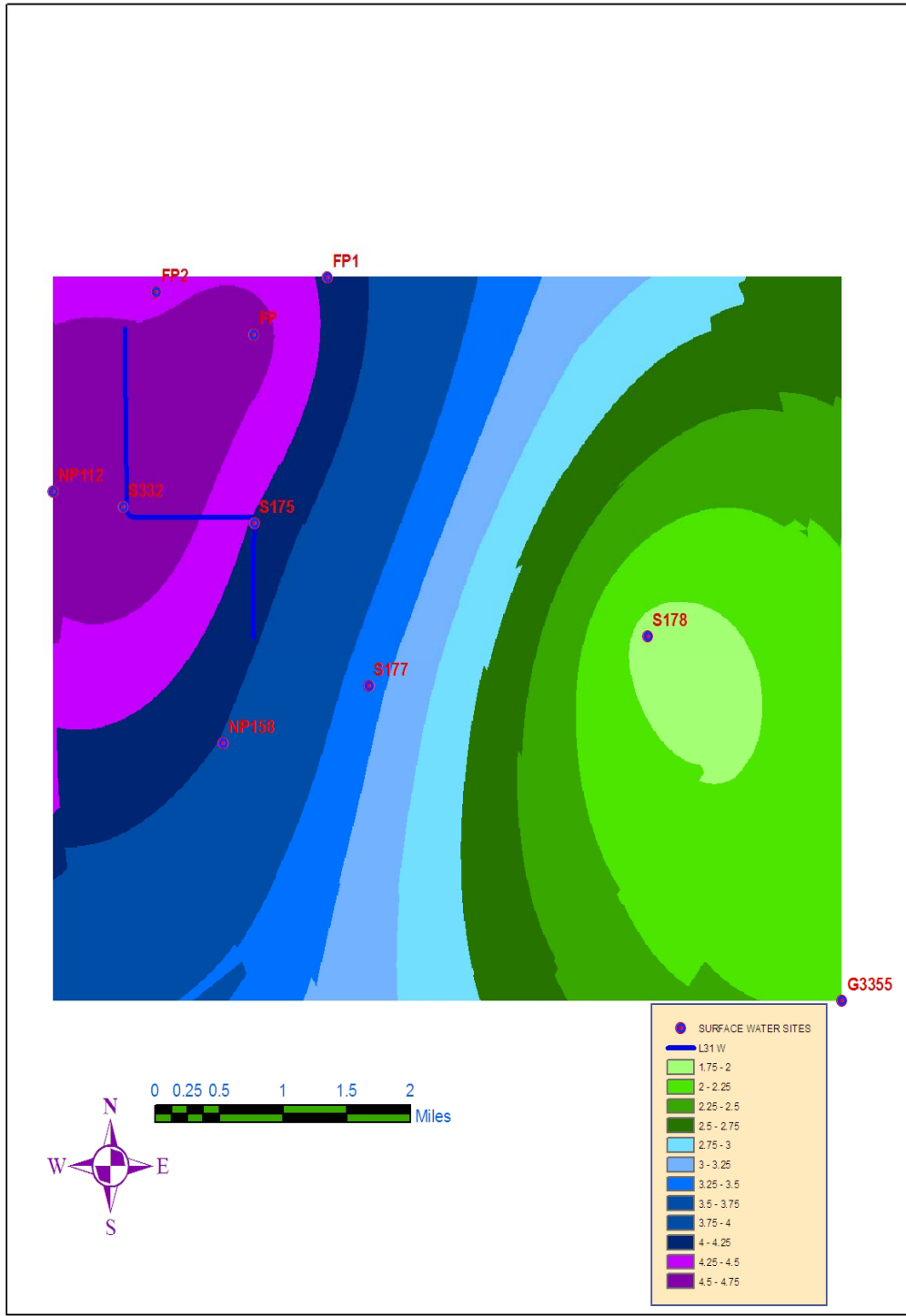


Figure 4.8

E



F

Figure 4.8

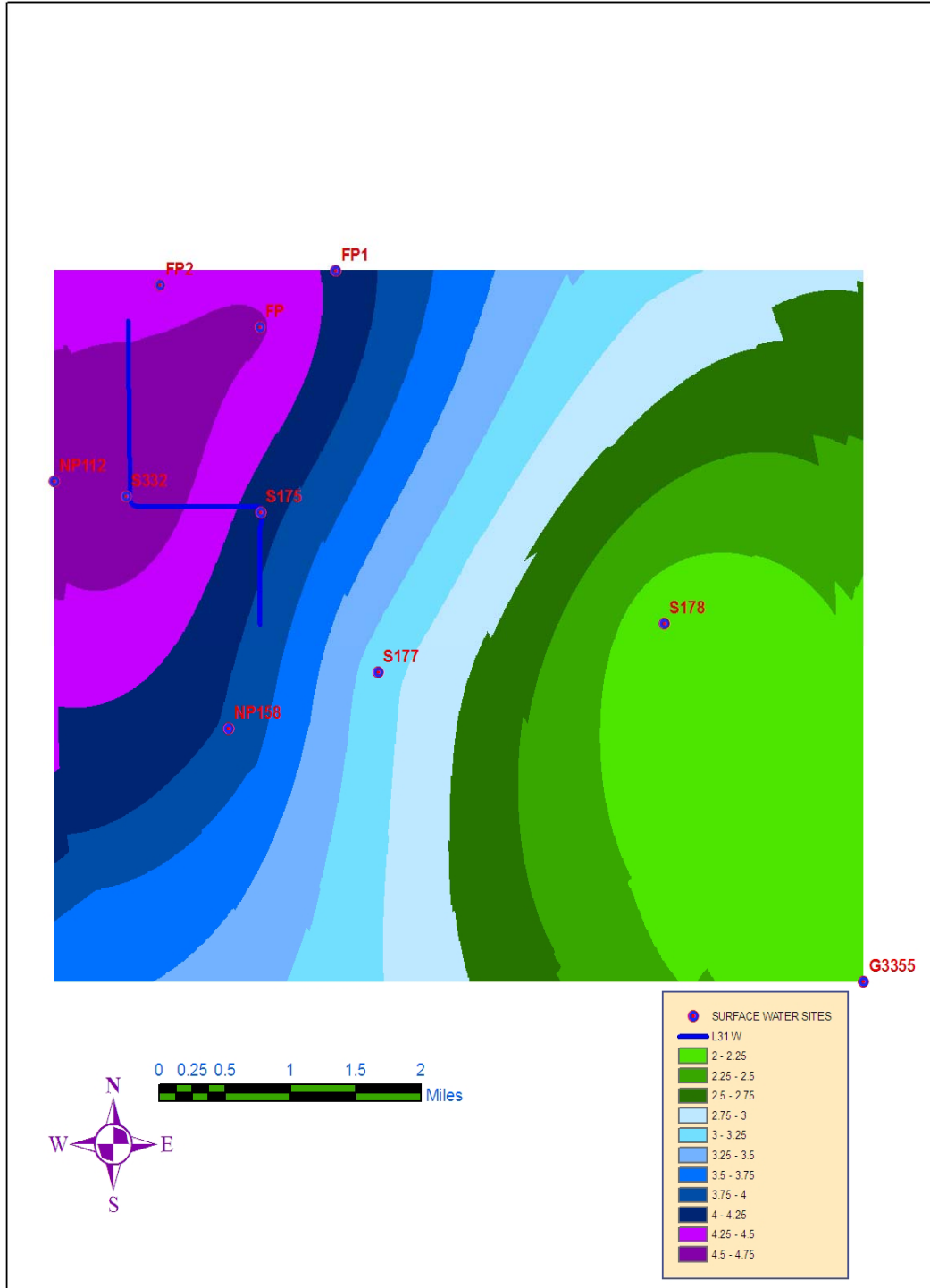


Figure 4.8

G

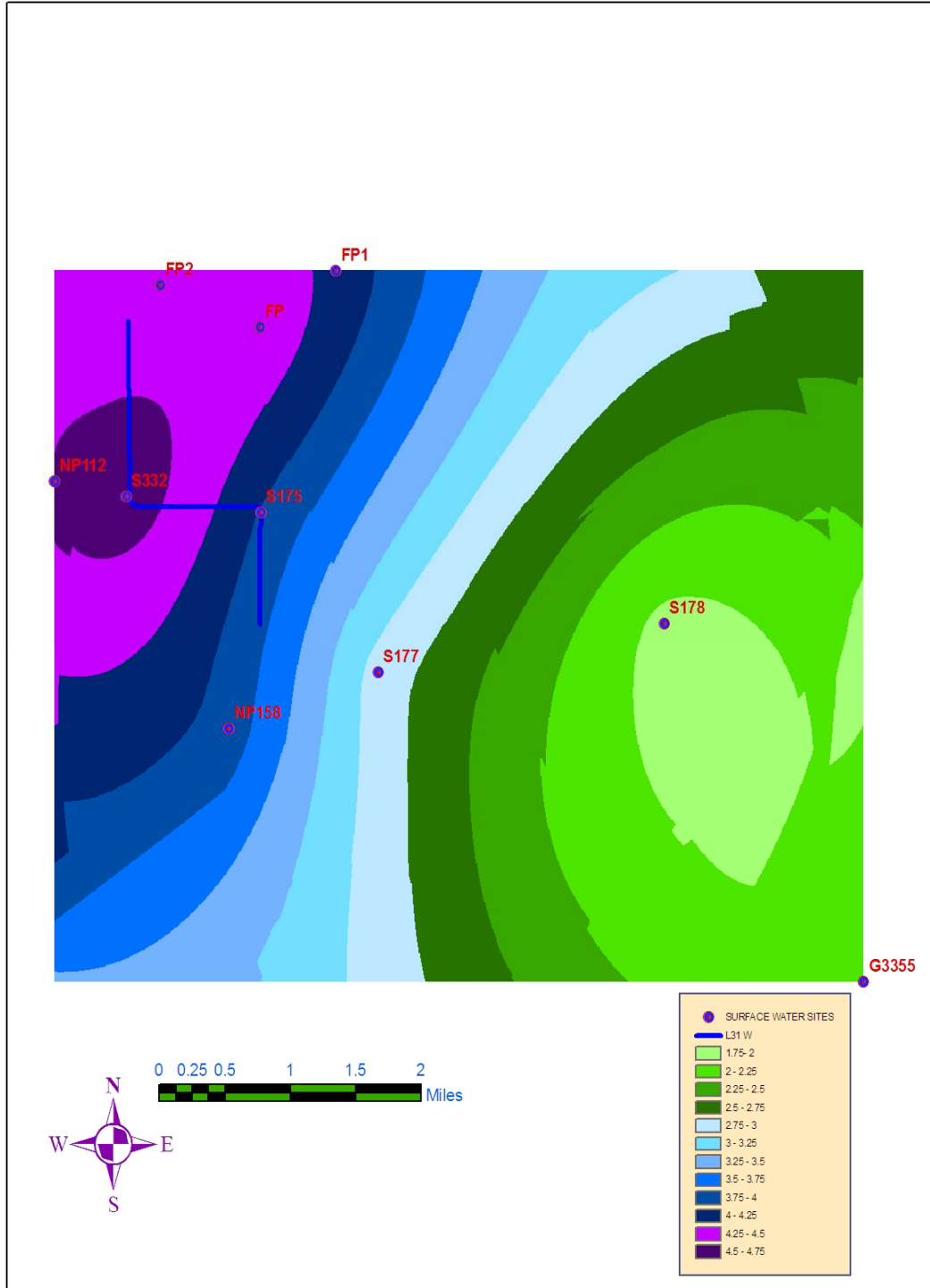


Figure 4.8

H

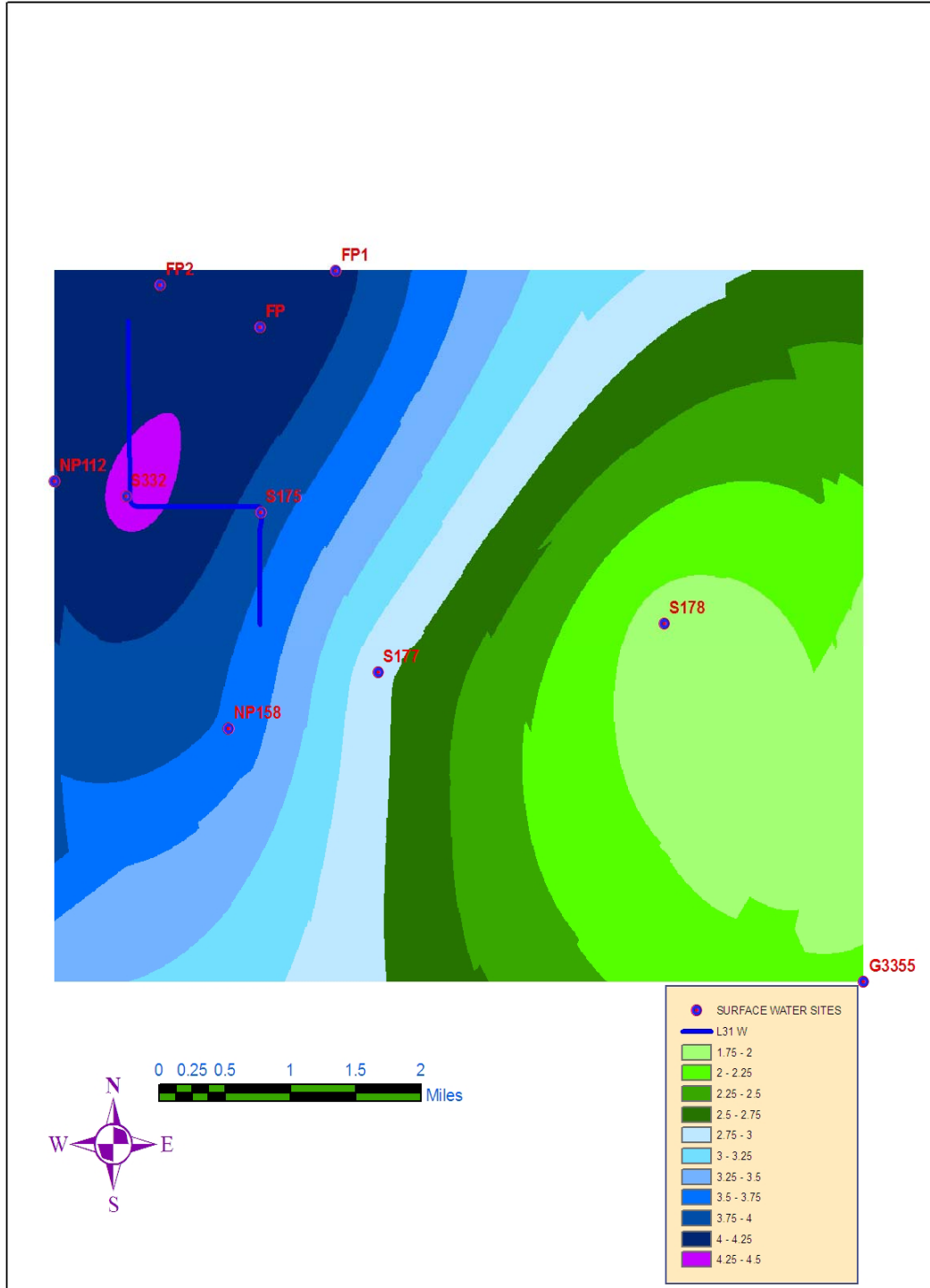


Figure 4.8

I

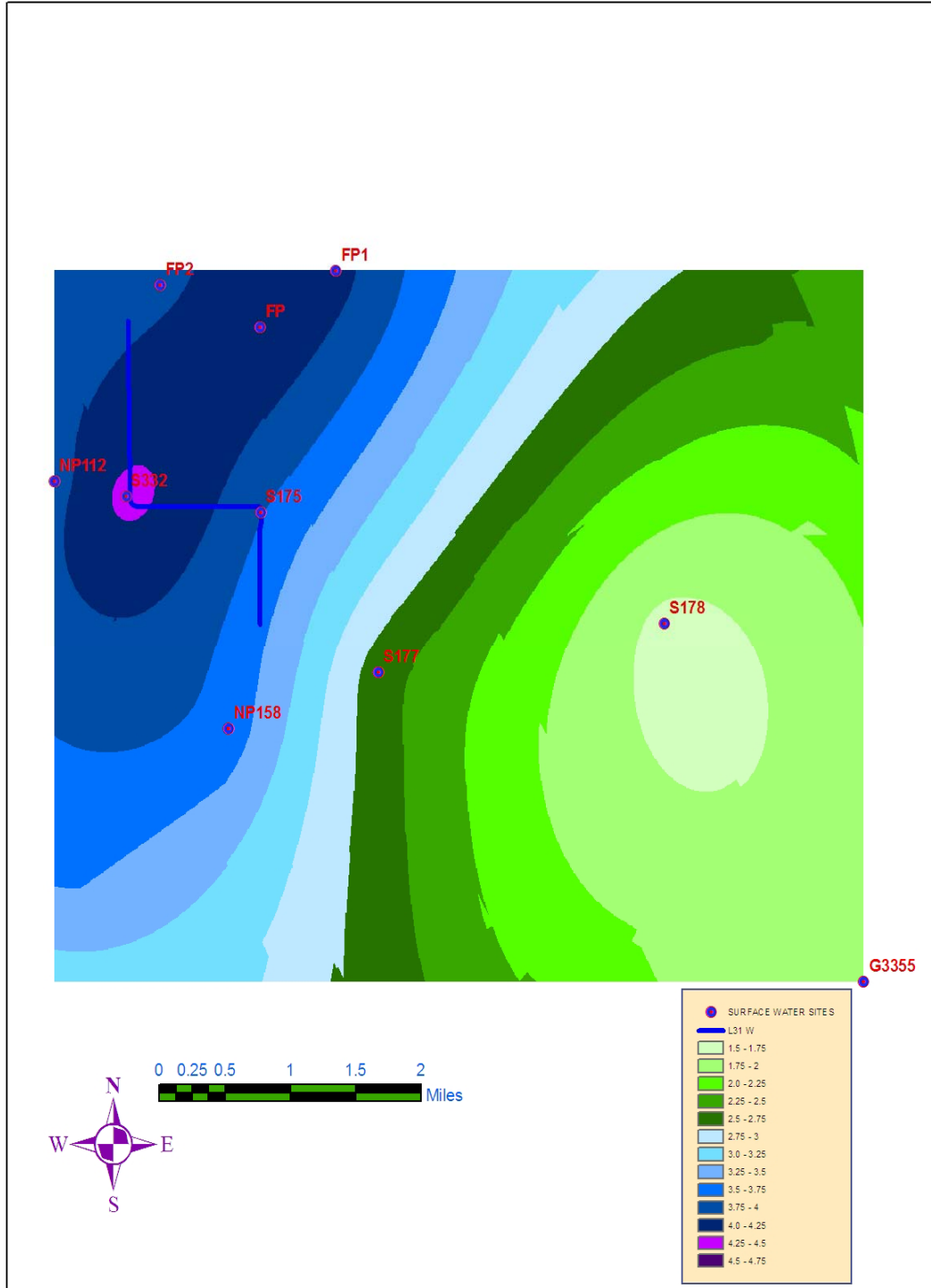


Figure 4.8

J

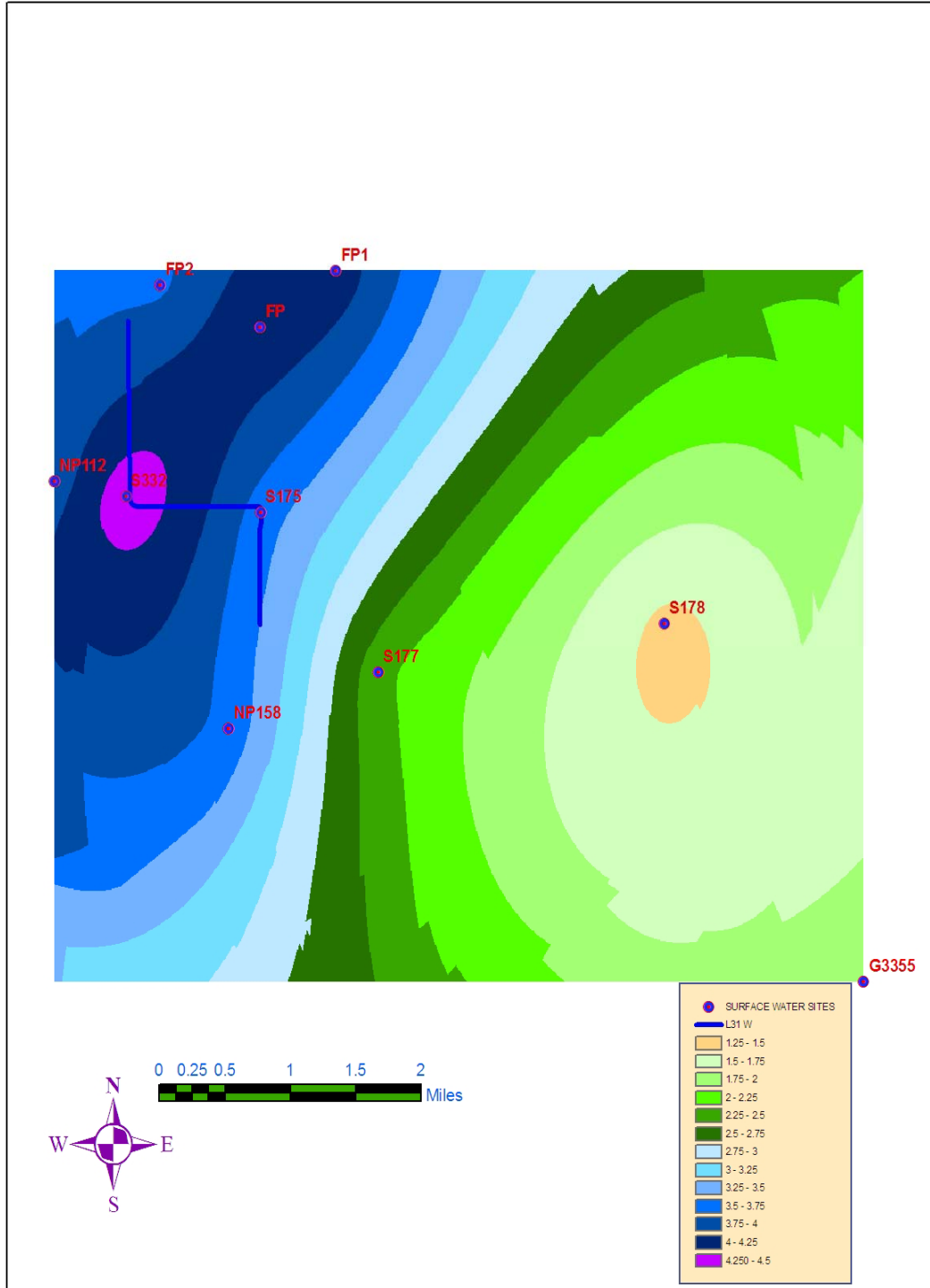
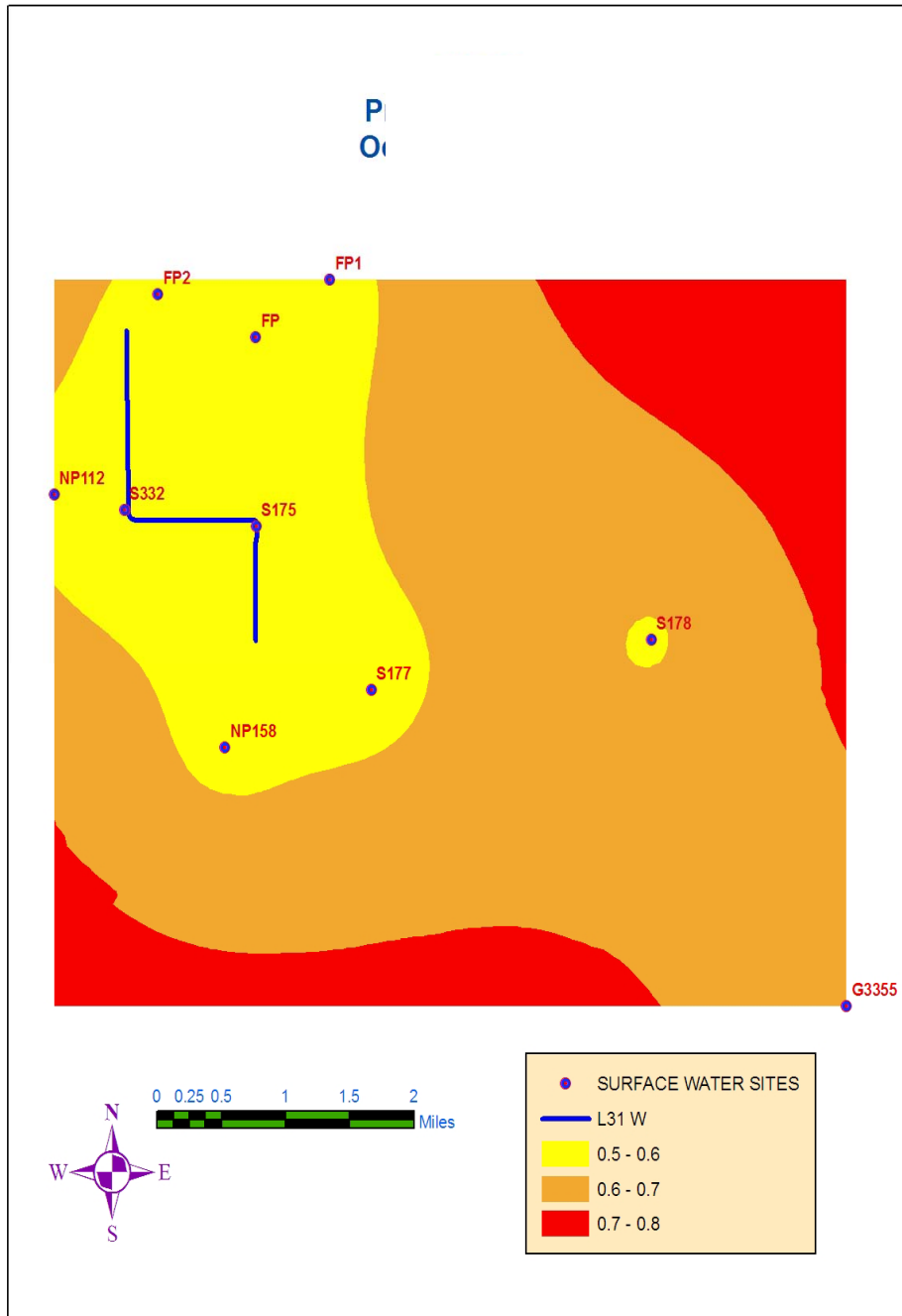


Figure 4.8

K



A

Figure 4.9 (A) Prediction error for SWEM October 12, 1999. (B) Prediction error for SWEM October 13, 1999. (C) Prediction error for SWEM October 14, 1999. (D) Prediction error for SWEM October 15, 1999. (E) Prediction error for SWEM October 16, 1999. (F) Prediction error for SWEM October 17, 1999. (G) Prediction error for SWEM October 18, 1999. (H) Prediction error for SWEM October 19, 1999. (I) Prediction error for SWEM October 20, 1999. (J) Prediction error for SWEM October 21, 1999. (K) Prediction error for SWEM October 22, 1999. Legend error values are in feet.

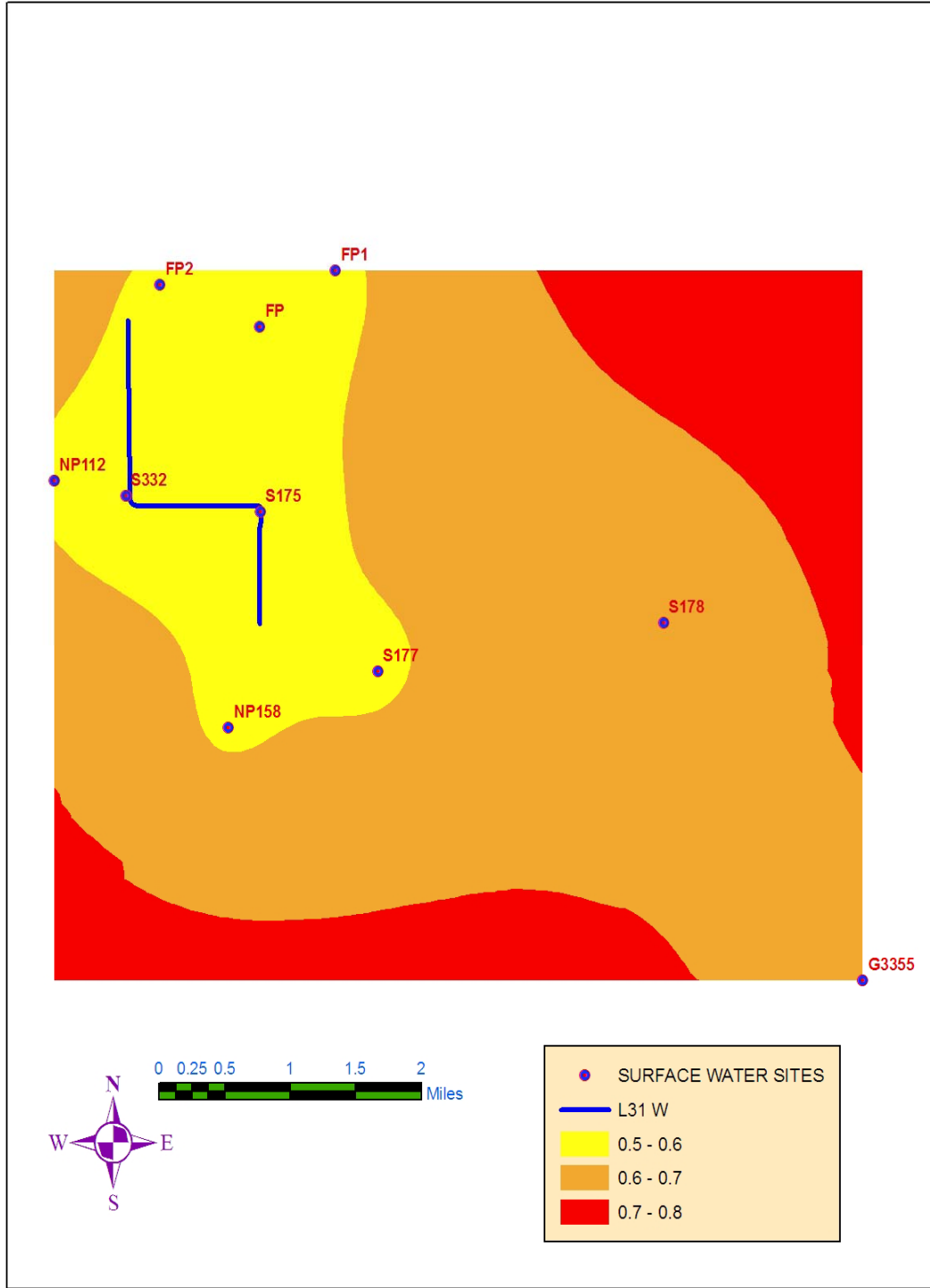


Figure 4.9

B

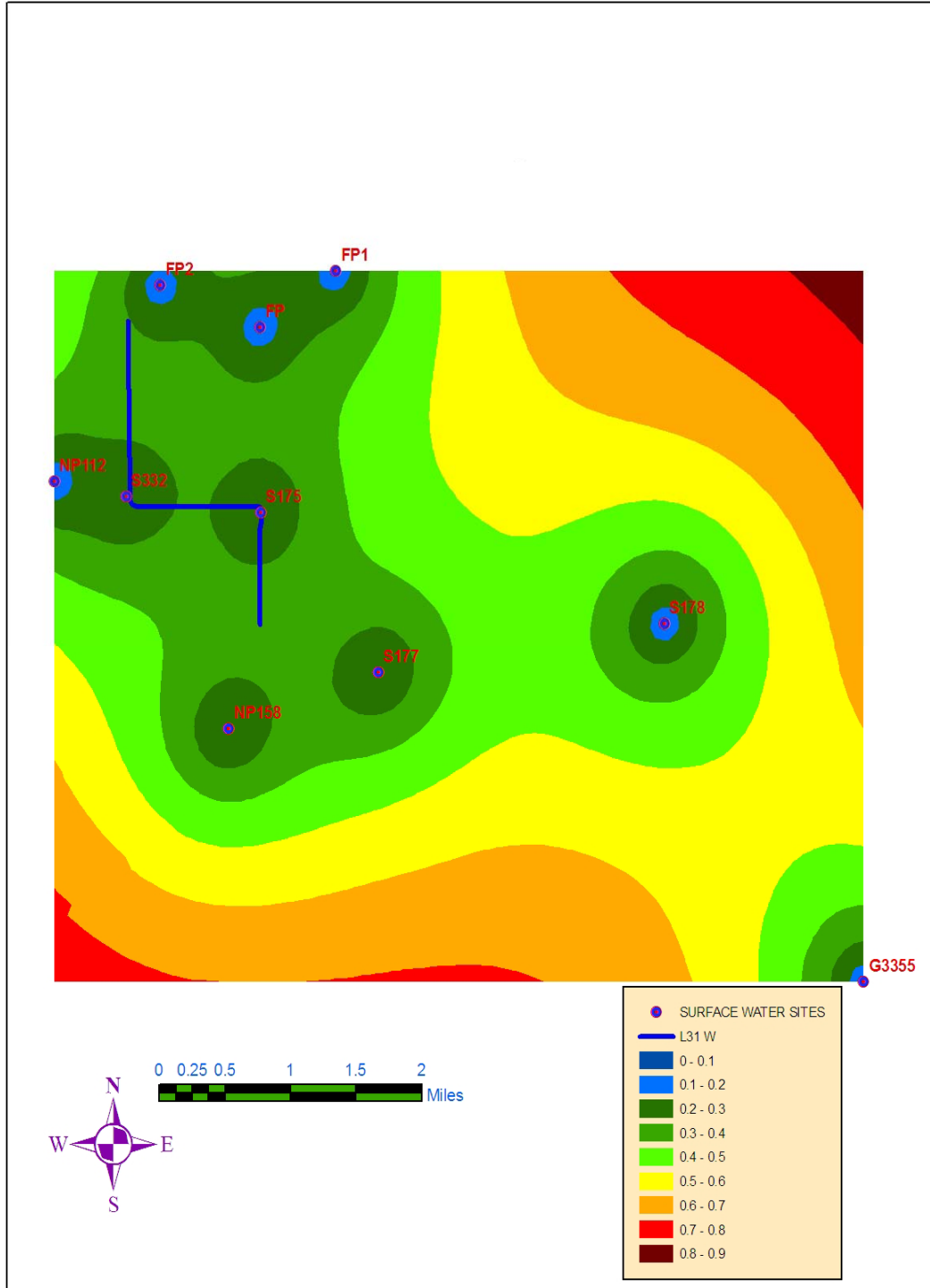


Figure 4.9

C

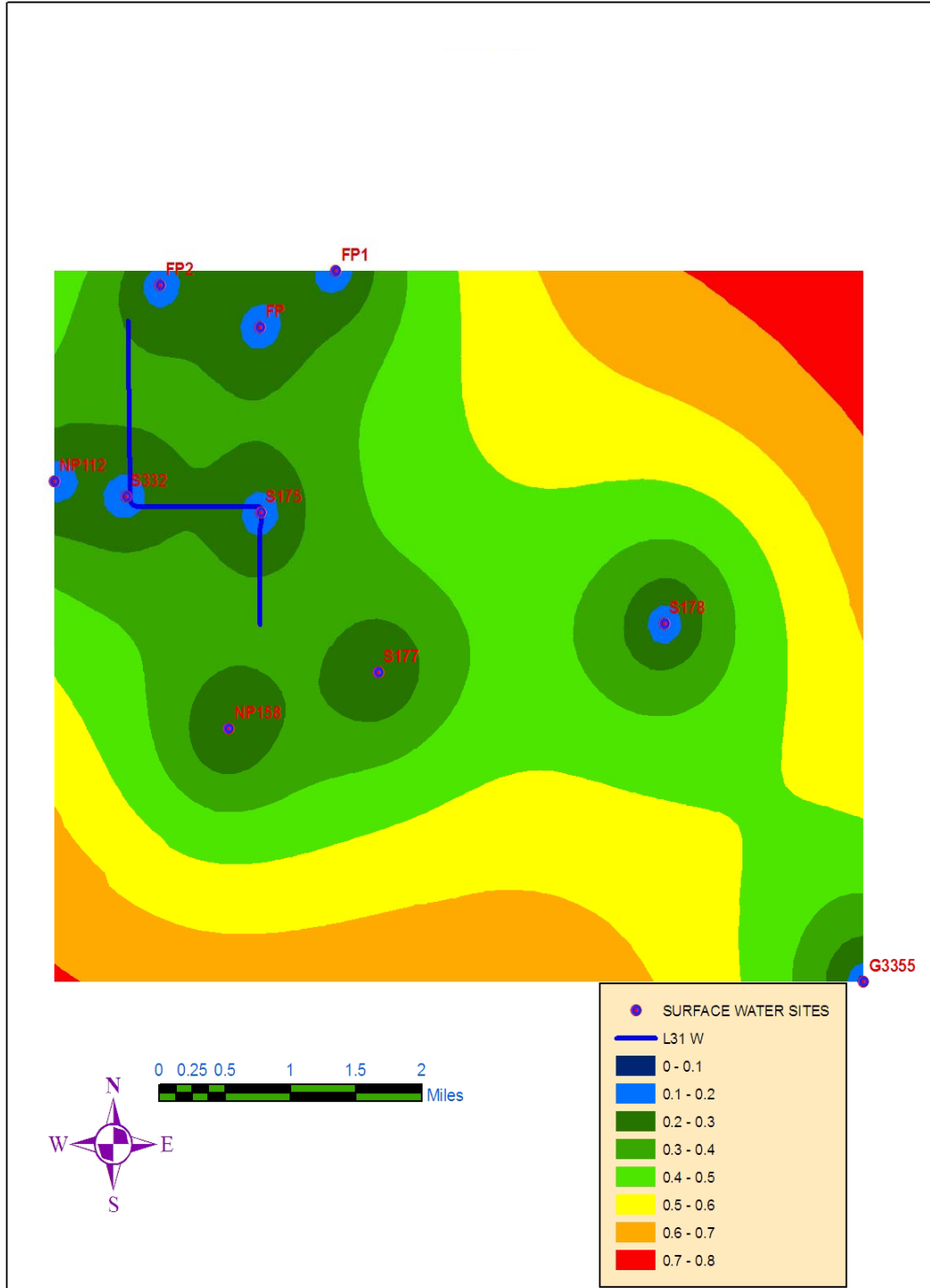


Figure 4.9

D

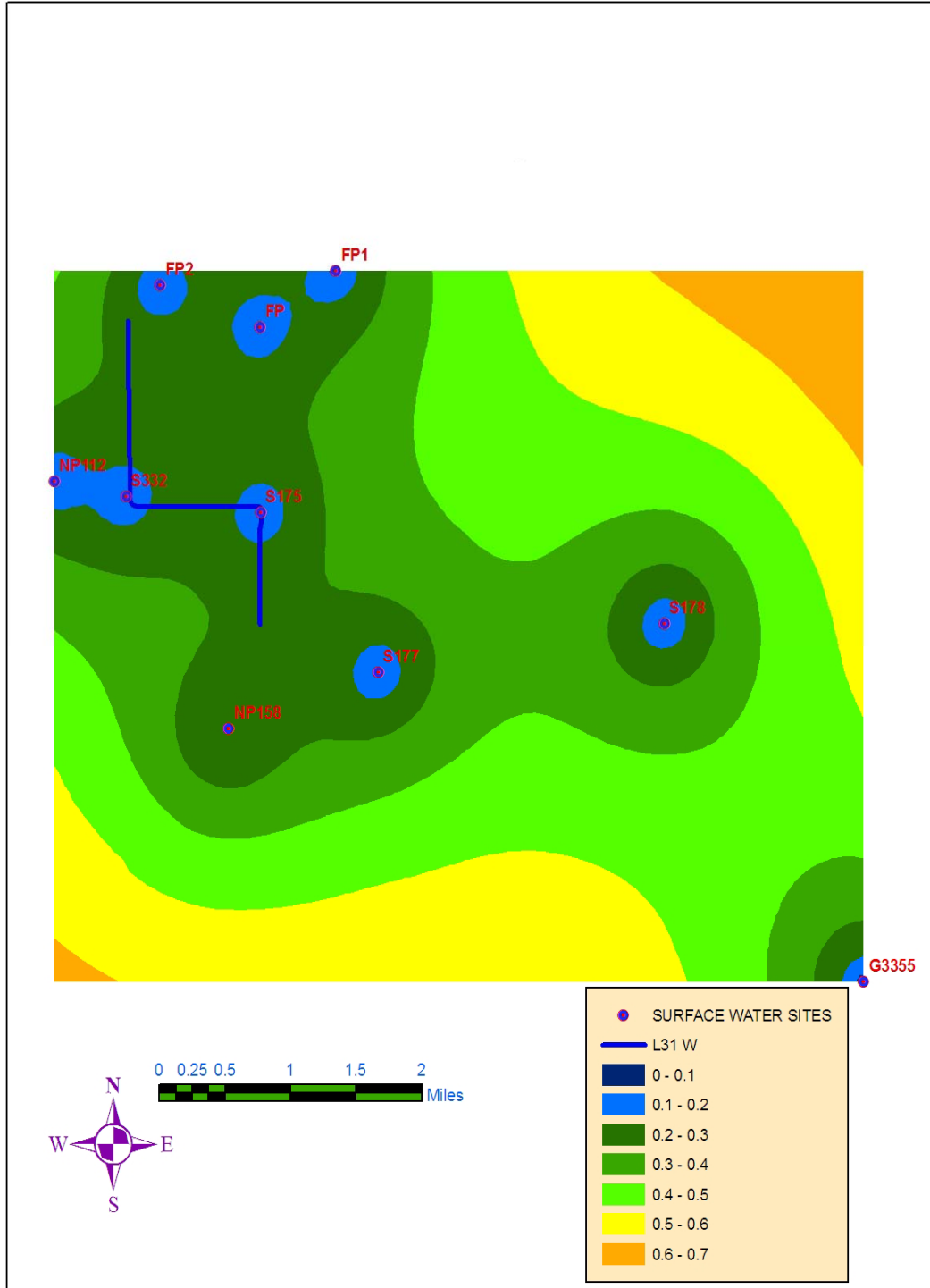


Figure 4.9

E

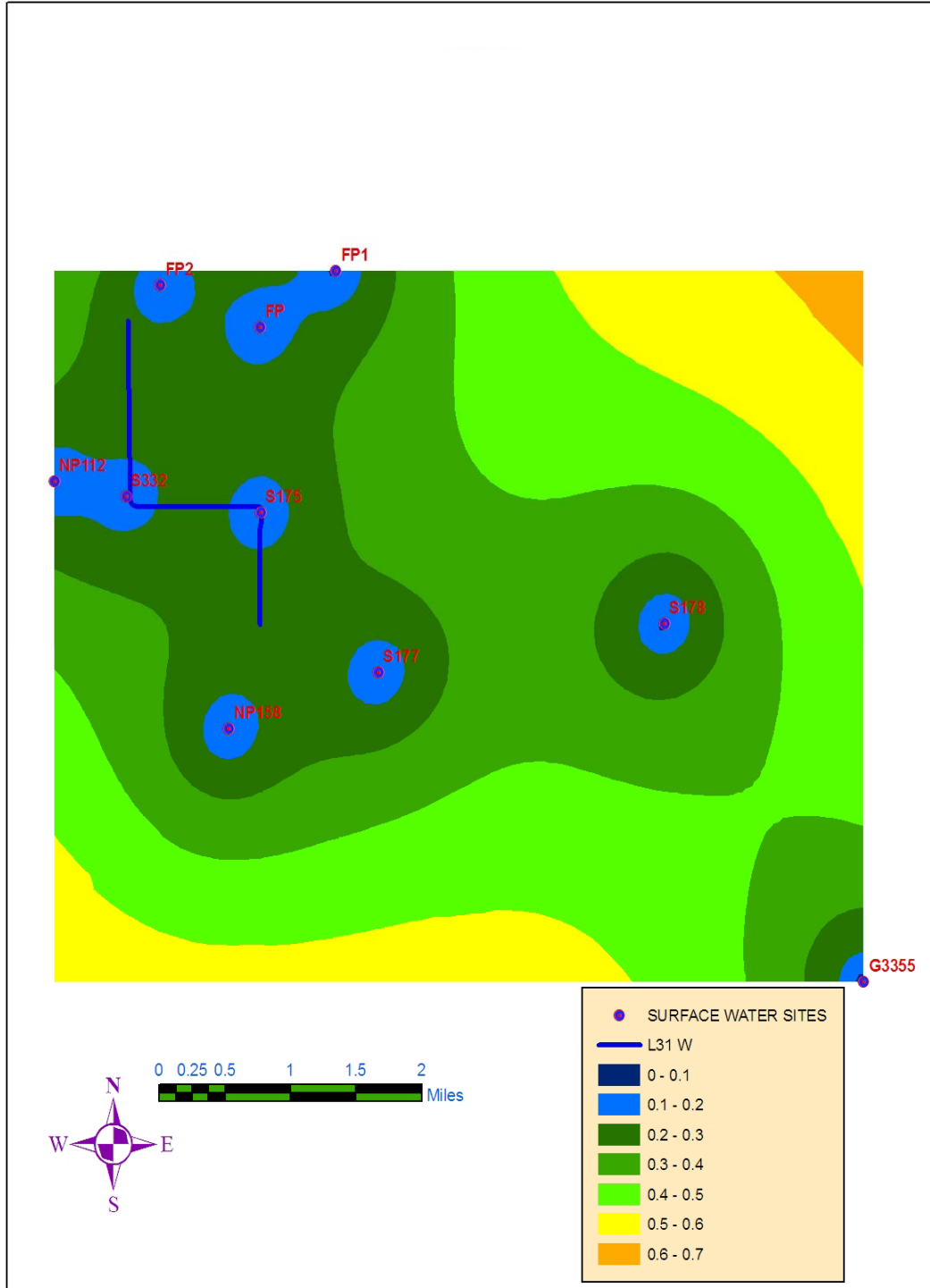


Figure 4.9

F

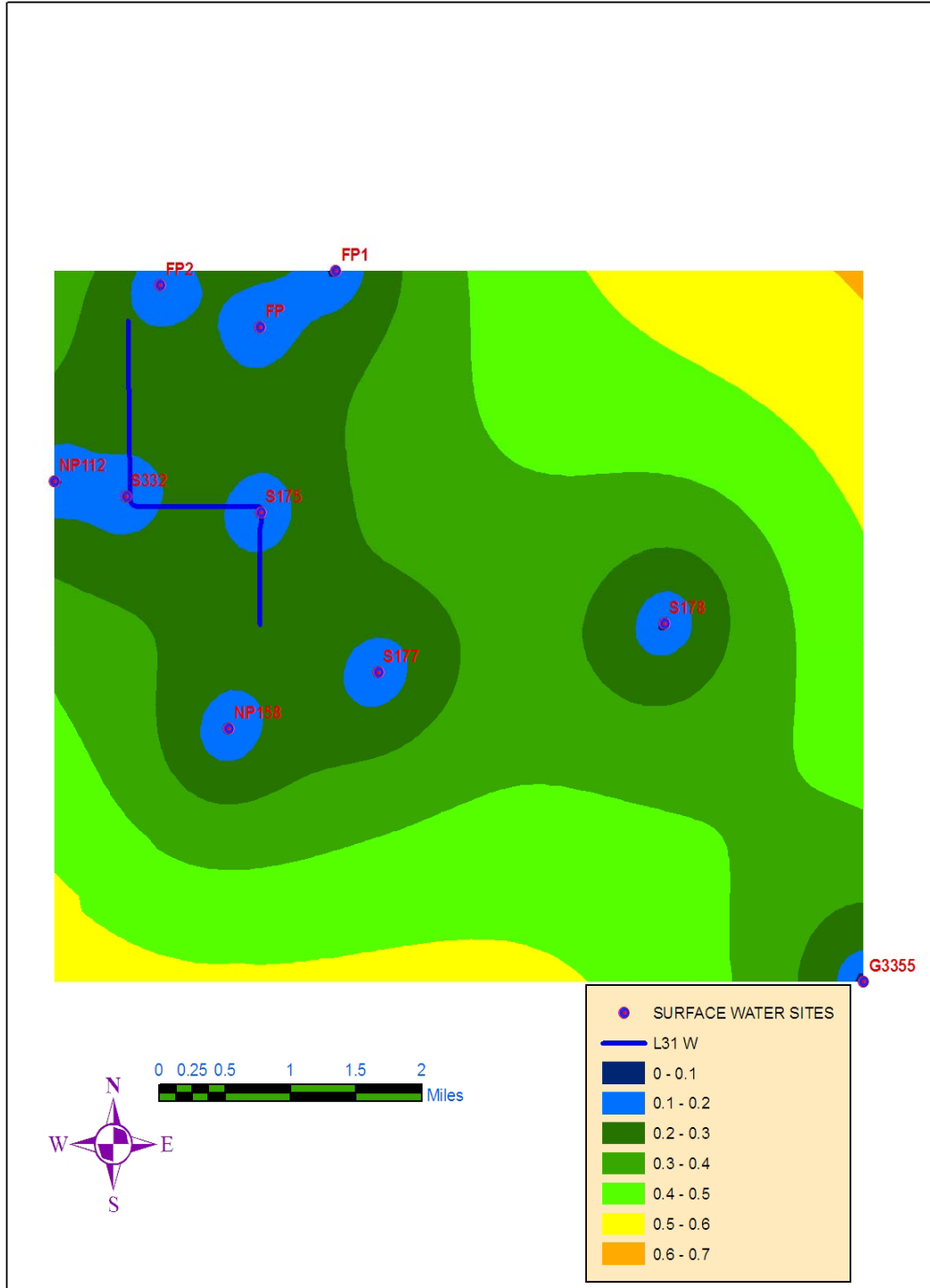


Figure 4.9

G

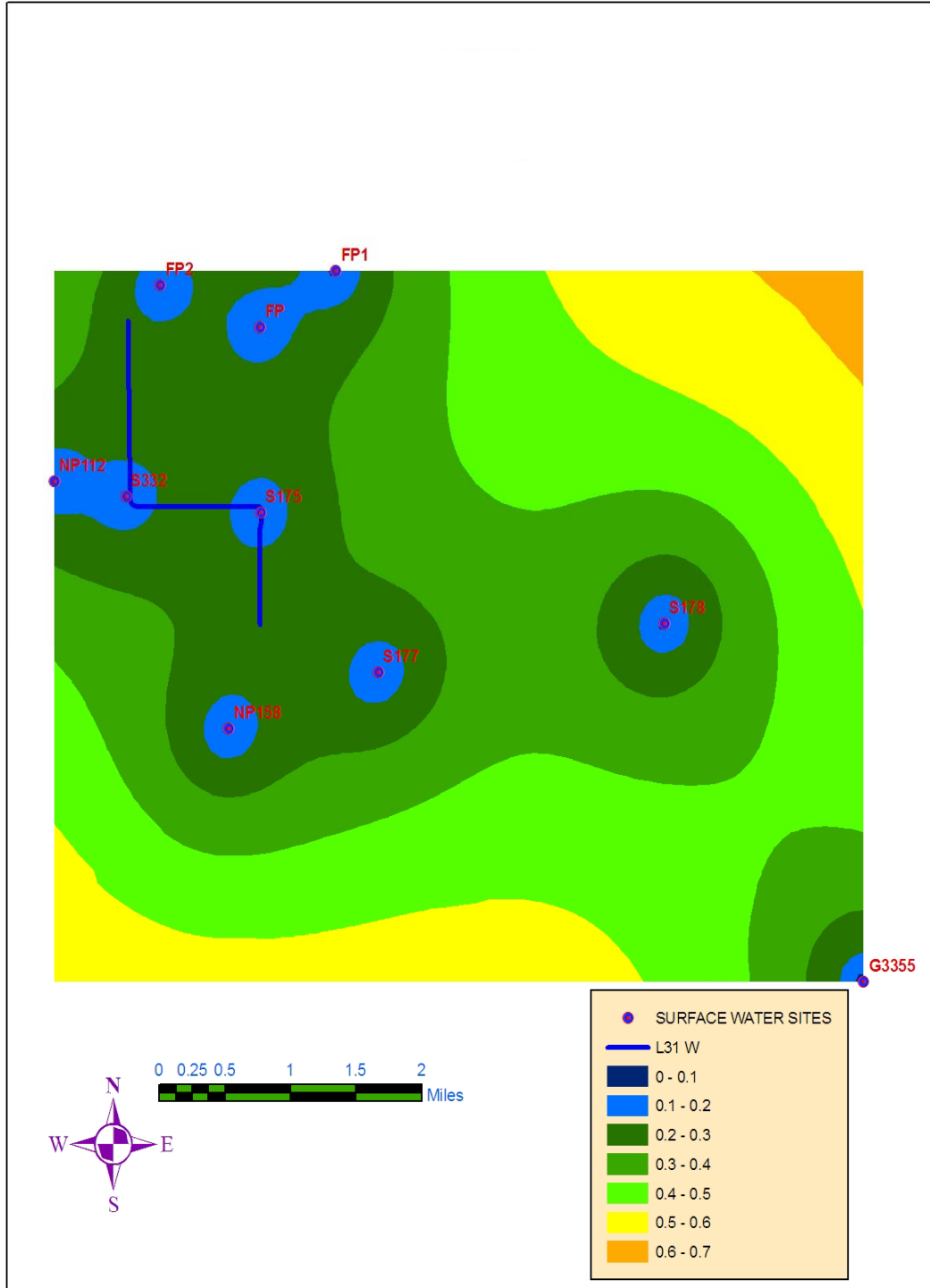


Figure 4.9

H

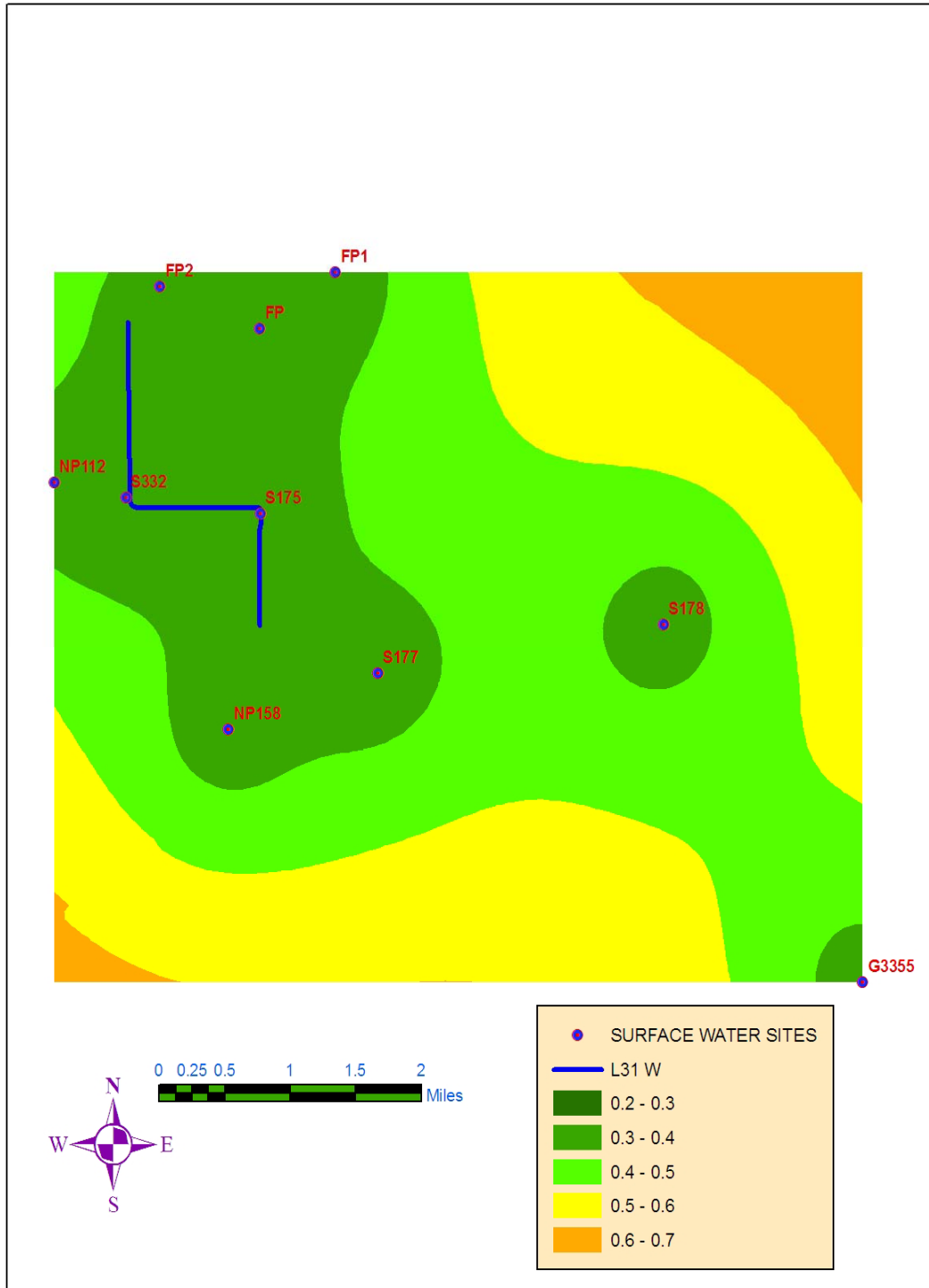


Figure 4.9

I

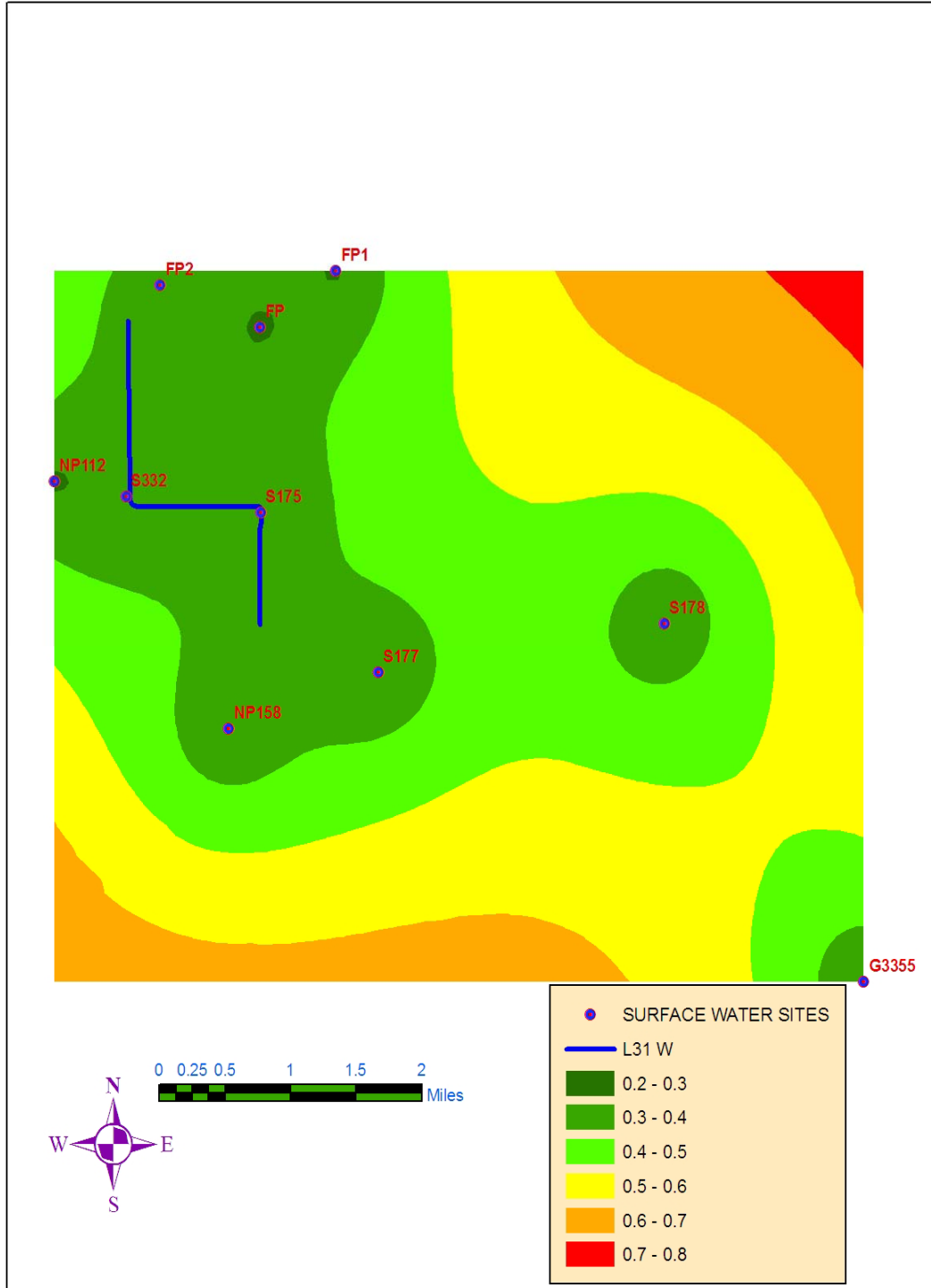


Figure 4.9

J

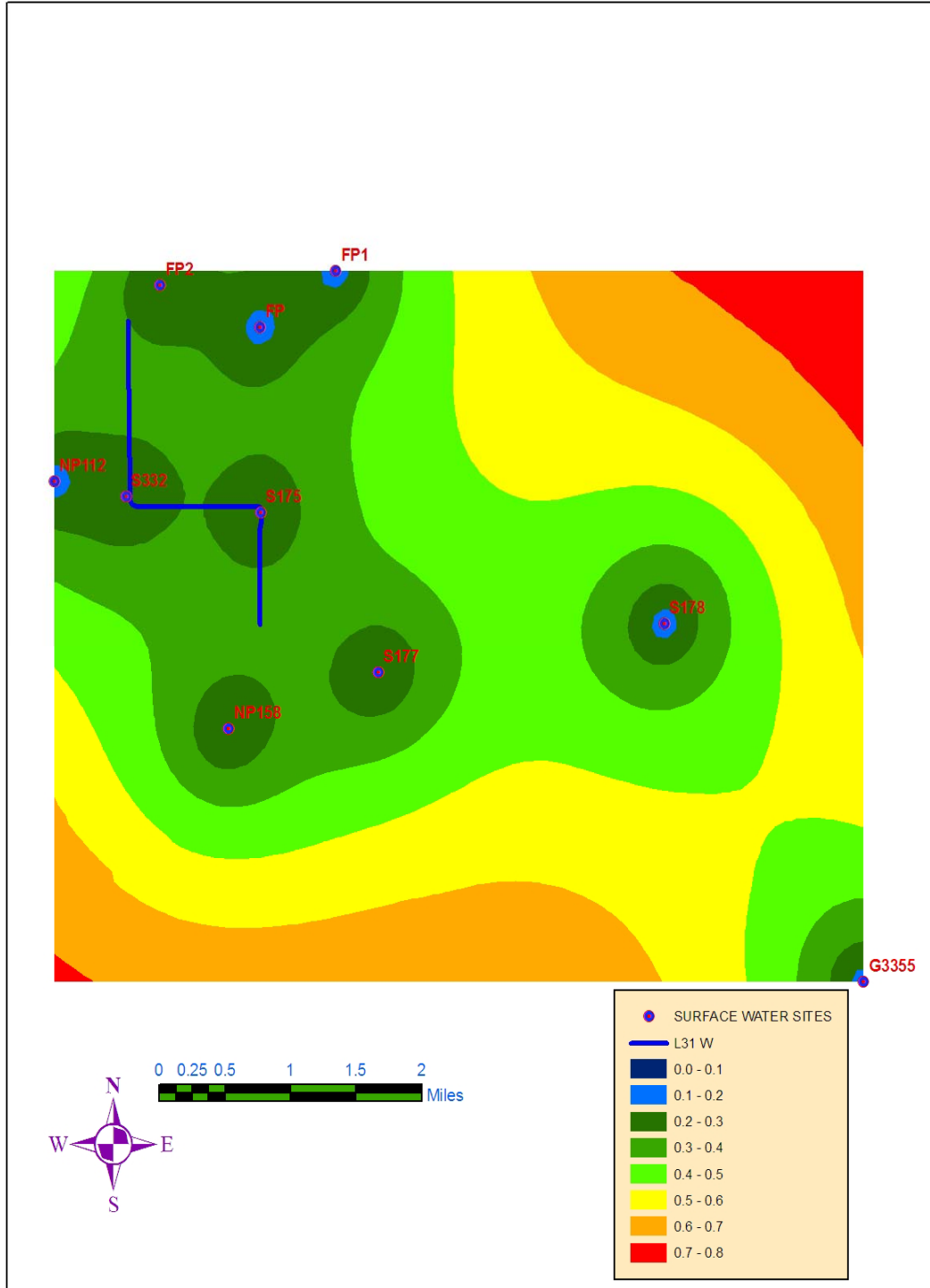


Figure 4.9

K

### **Surface Water Inundation Map**

The surface water inundation map, SWIM, was created by subtracting topographic grids from surface water grids. SWIM was applied to each day of the study period from October 12-22, 1999, Figure 4.10(A)-(L), and depth was characterized by five classes based on 0.25 ft. elevation intervals representing water table elevation below ground surface, Table 4.12. Numerical values found in the SWIM legends represent no inundation in 0.25 ft intervals. For example, the interval, 0-0.25 ft., represents a water table 0-0.25 ft. below land surface. An analysis of NAD 83 SWIM maps show a sharp increase in flooding that is coincident with Hurricane Irene. The maximum flood condition occurred on October 16, 1999, and inundation gradually decreased over the study period.

Inundation contours were also observed to conform to the change in surface water elevation. On October 12, 1999, SWIM shows inundation in the L31W canal and portions of wetland and agricultural areas. Inundation values in these areas are likely the result of a low topographic elevation and high surface water elevation at the S332 pumping station. The same reason may also explain inundation patterns for October 13, 1999.

The low surface water elevation value of the S178 pumping station and well G3355 significantly influenced inundation patterns in the southeast quadrant of the study area. Due to this, the first non-inundated area appear in the southeast quadrant on October 21, 1999.

Inundation statistics were calculated using ArcGIS 3D Analyst for October 16, 1999, Table 4.13. The SWIM NAD 83 inundation grid was used for the calculation, and values were calculated above a plane that was set to 0 ft. The Z-tolerance factor was set

to 0.1 ft. The greatest percentage change in inundation volume occurs on October 15, 1999, and the largest volumetric value occurs on October 16, 1999. The calculated volume of water over the study area was found to decrease during October 17-22, 1999. The increase in volume for October 14, 1999, is likely due to either the increase in surface water elevation from conveyance operations or initial rainfall from Hurricane Irene.

The most vulnerable areas inside the study area are those which have the highest magnitude of inundation and duration of flooding. SWIM classes 4 and 5 represent a high magnitude, and the areas remaining in class 4 and class 5 on SWIM October 22, 1999, shows the greatest duration of flooding. Figure 4.10(K) shows the coverage of class 4 and class 5 areas for October 22, 1999, and these areas were determined to be the most vulnerable inside the study area. These areas coincide with low elevation areas in the ALSM DEM.

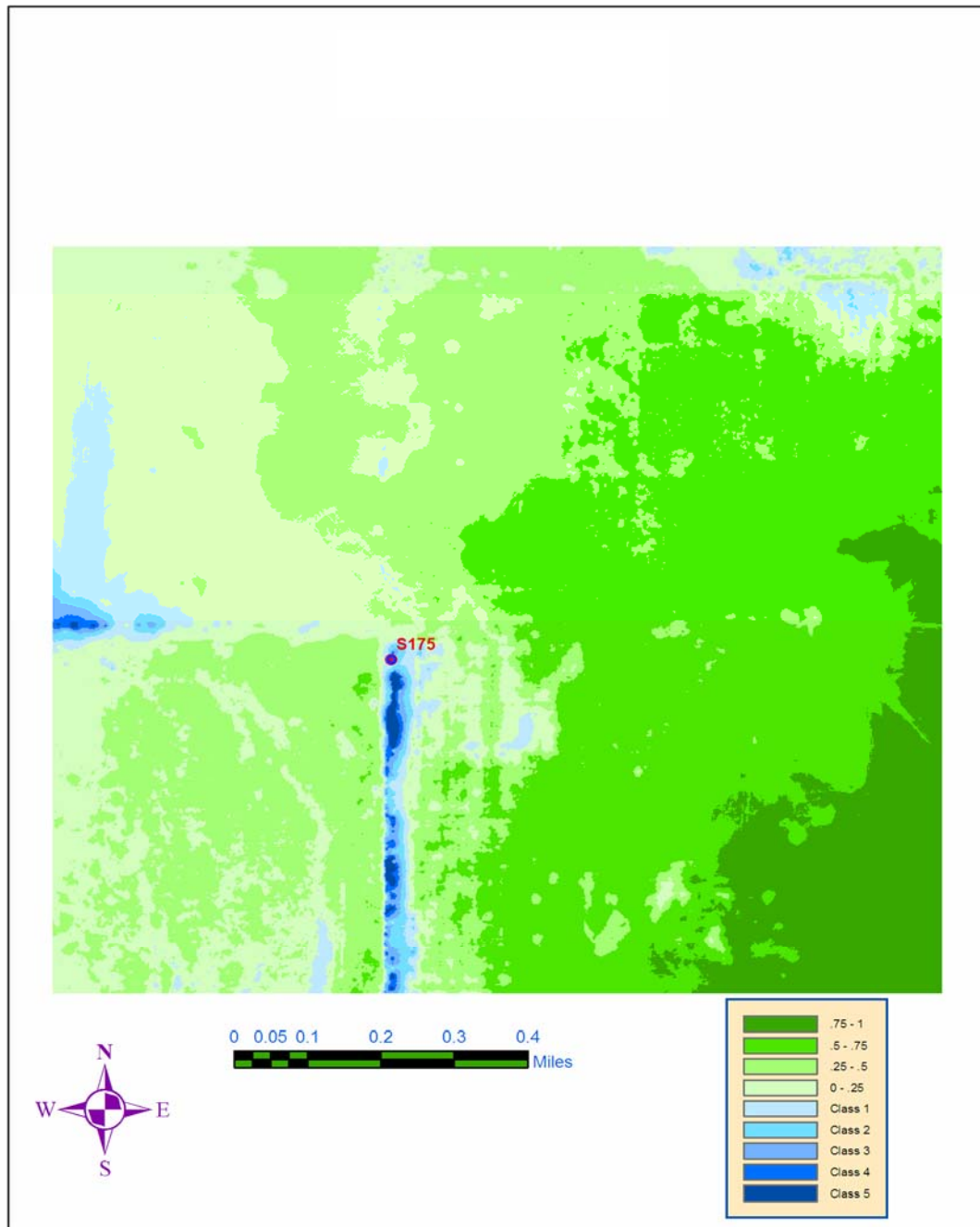


Figure 4.10(A) SWIM October 12, 1999. (B) SWIM October 13, 1999. (C) SWIM October 14, 1999. (D) SWIM October 15, 1999. (E) SWIM October 16, 1999. (F) SWIM October 17, 1999. (G) SWIM October 18, 1999. (H) SWIM October 19, 1999. (I) SWIM October 20, 1999. (J) SWIM October 21, 1999. (K) SWIM October 22, 1999. Numerical values are in feet.

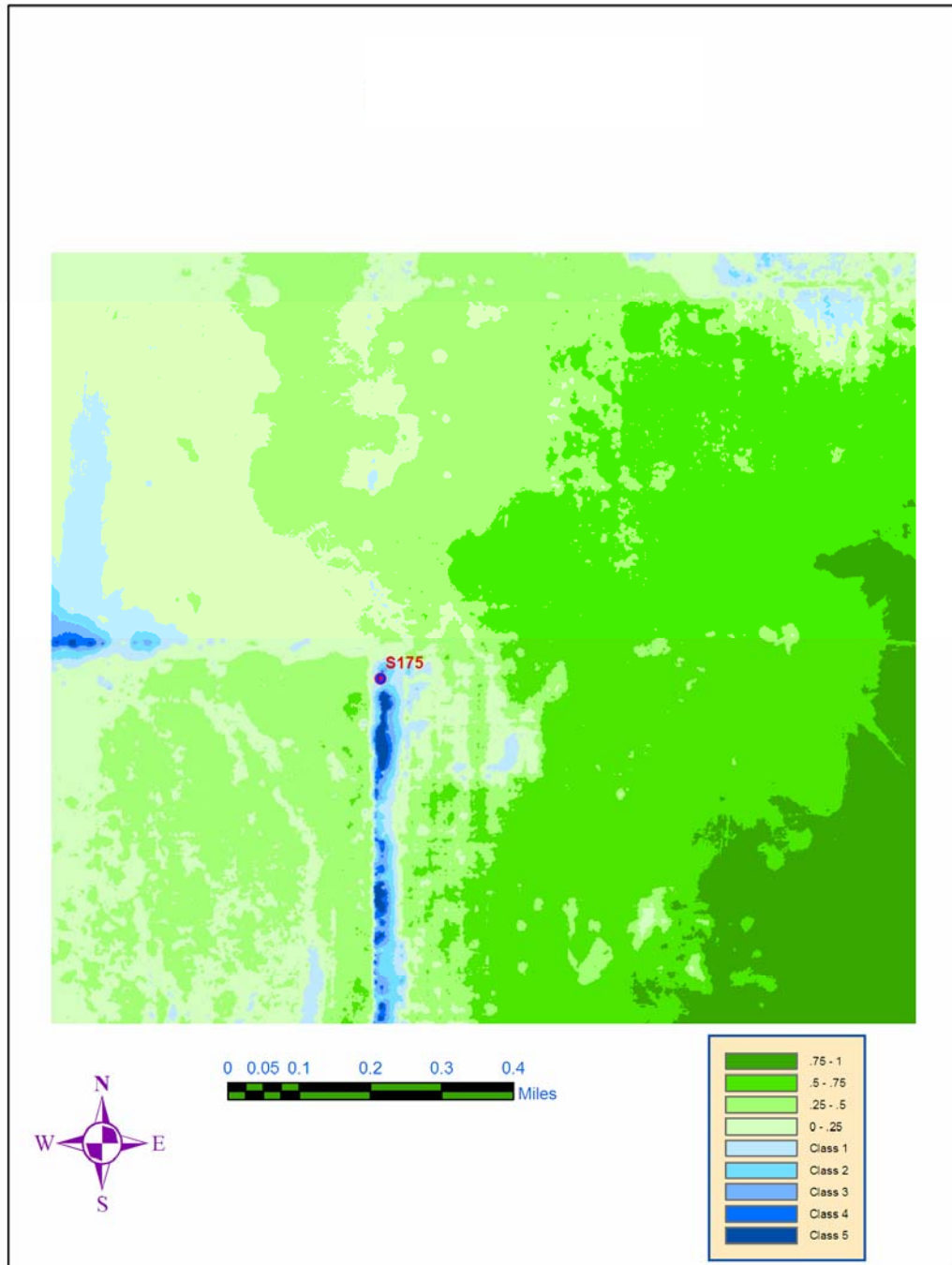


Figure 4.10

B

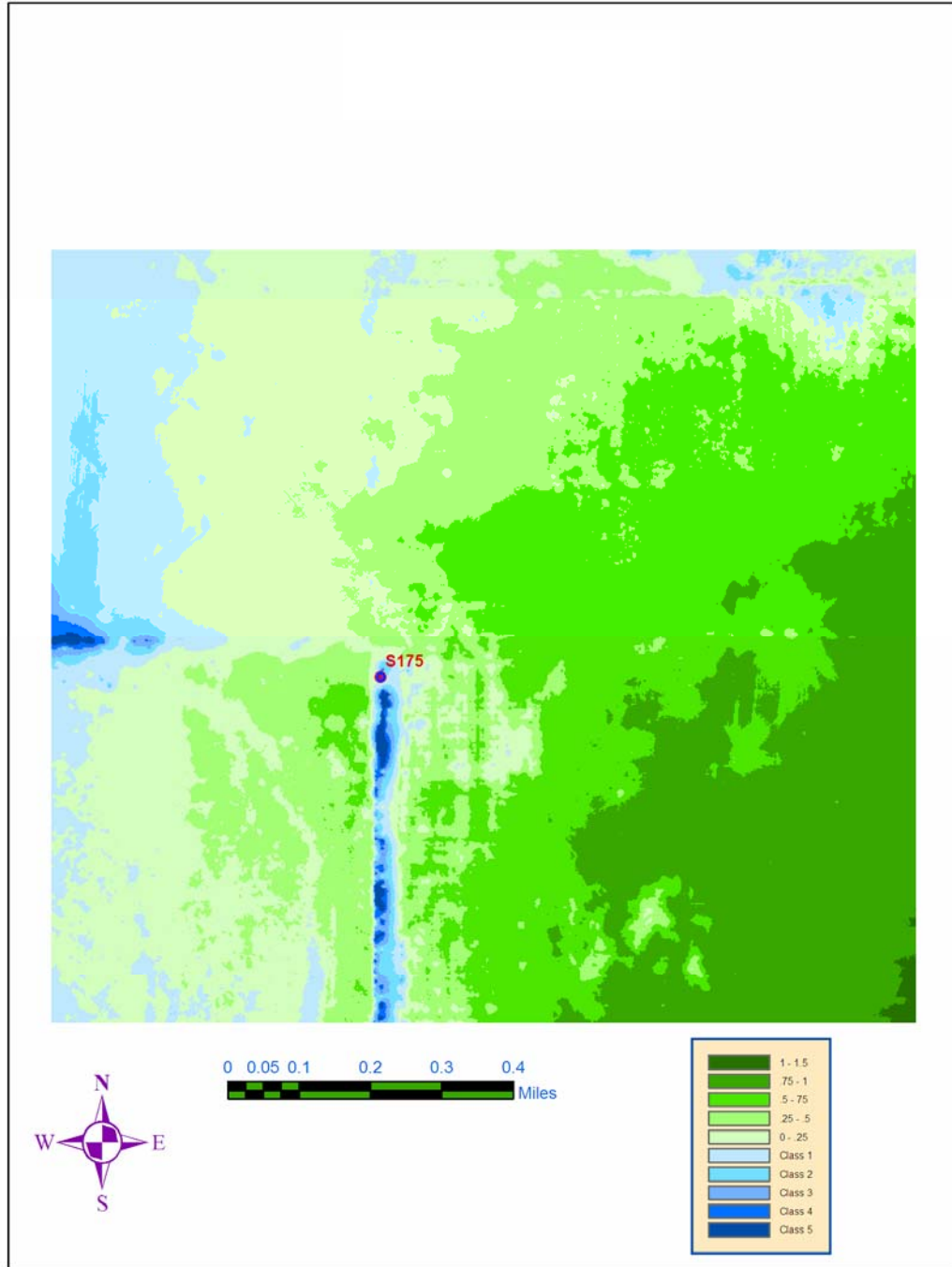


Figure 4.10

C

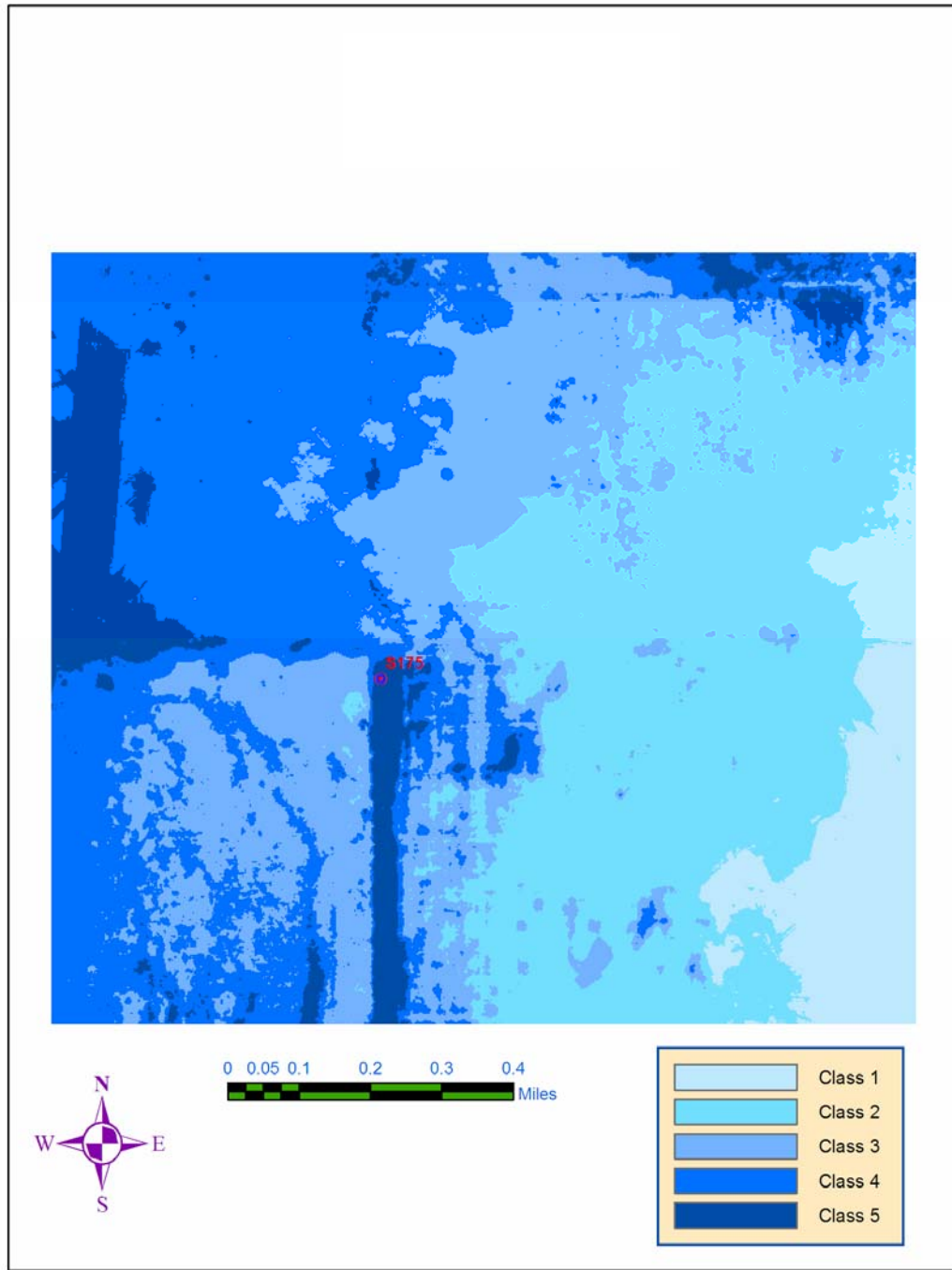


Figure 4.10

D

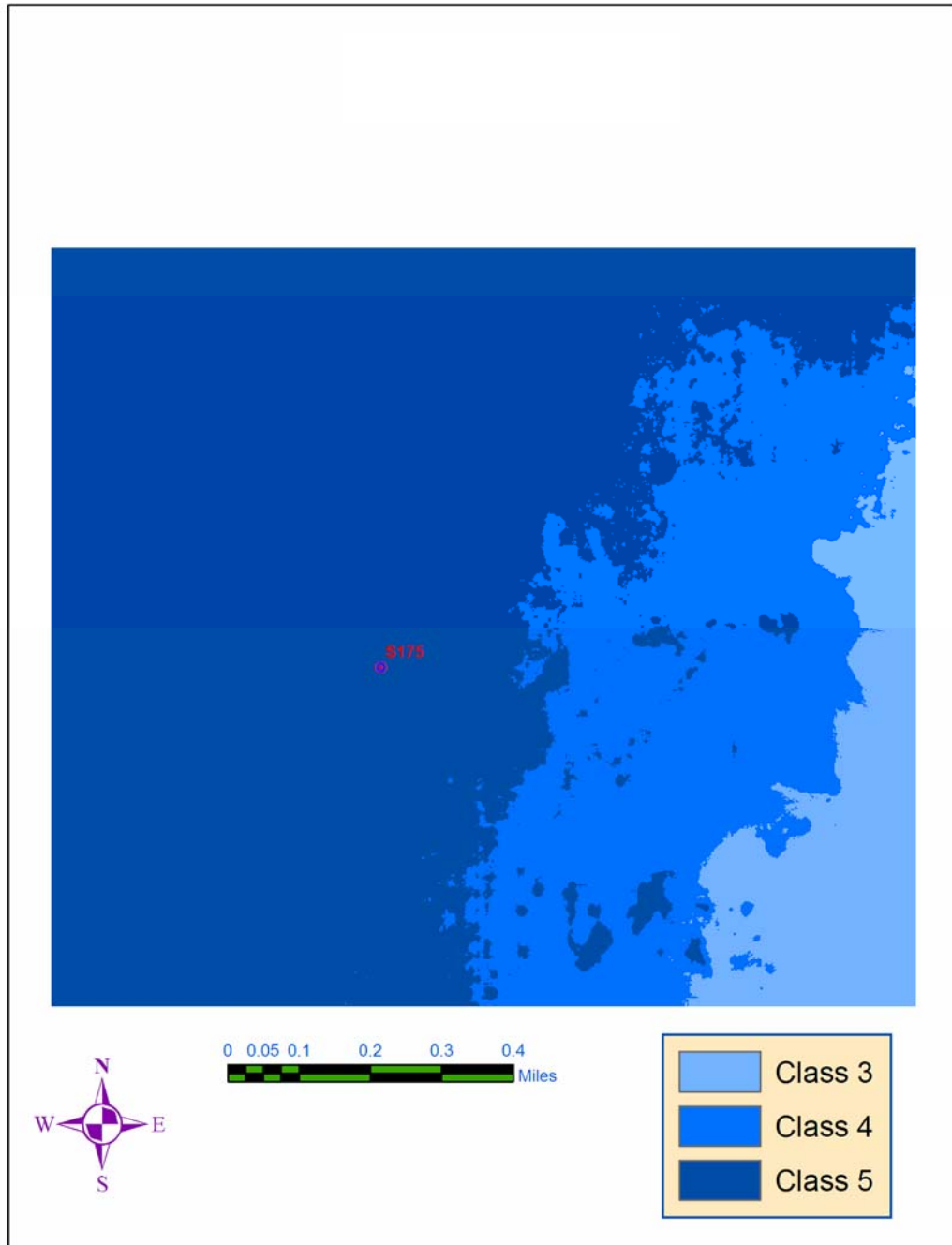


Figure 4.10

E

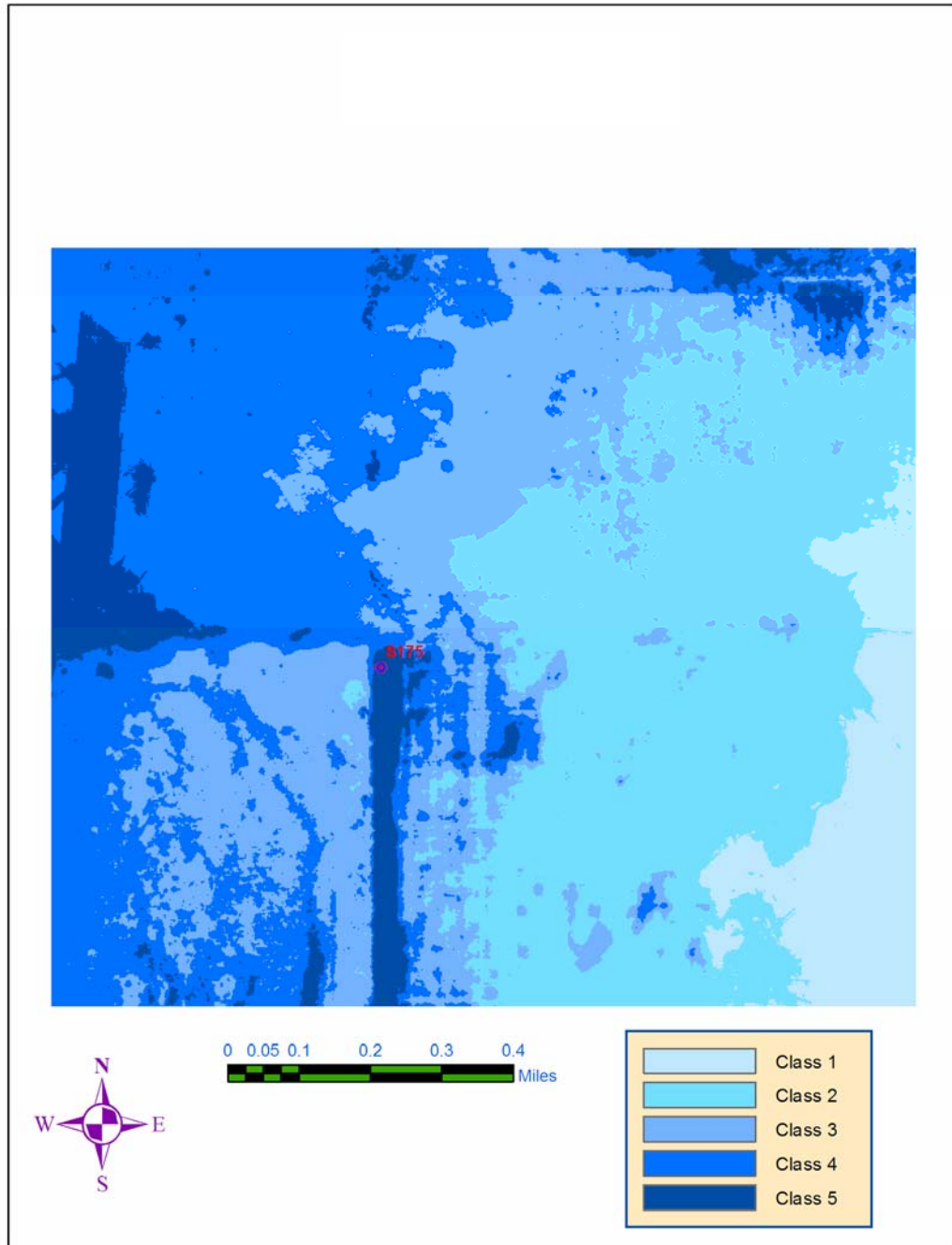


Figure 4.10

F

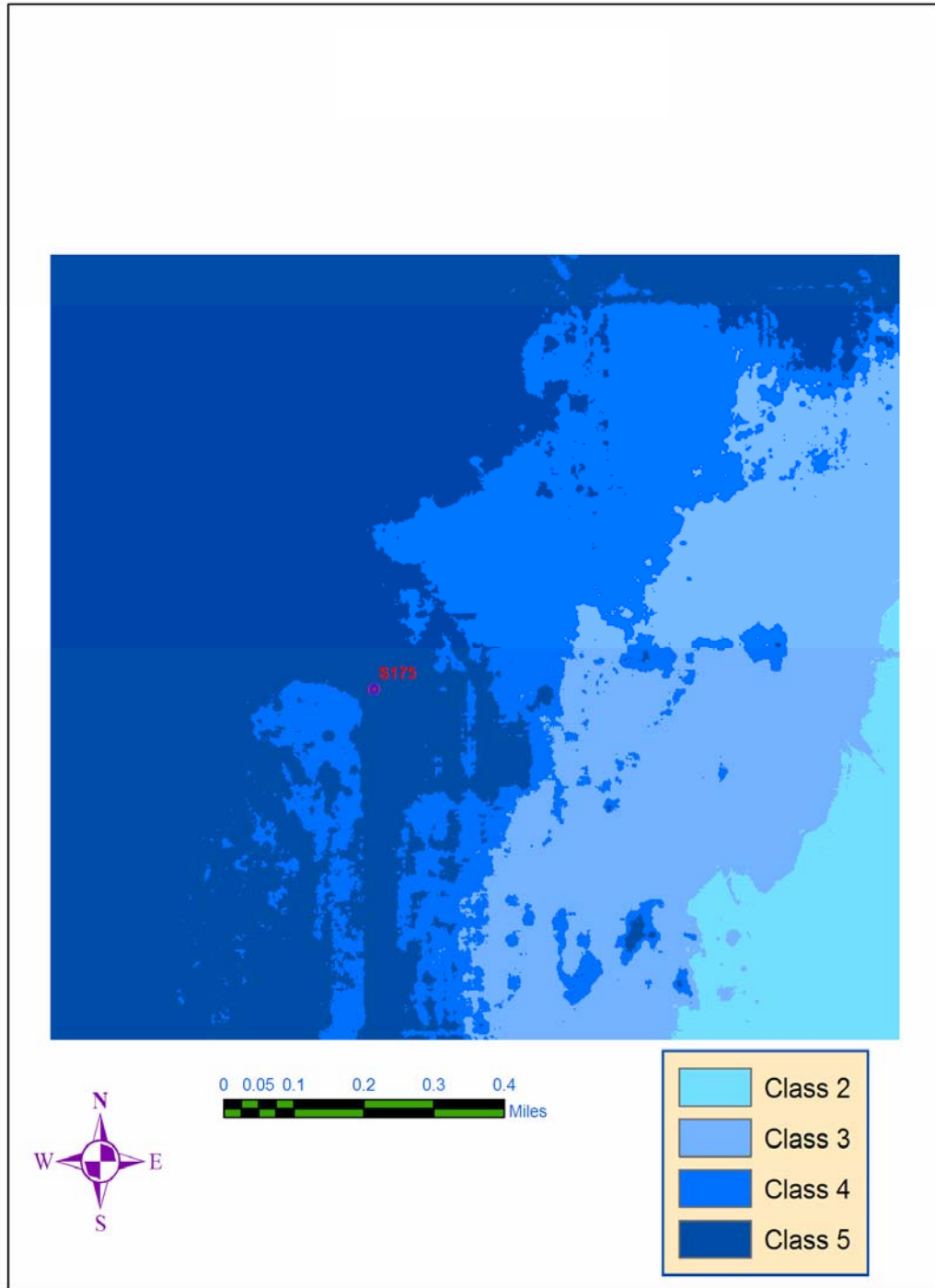


Figure 4.10

G

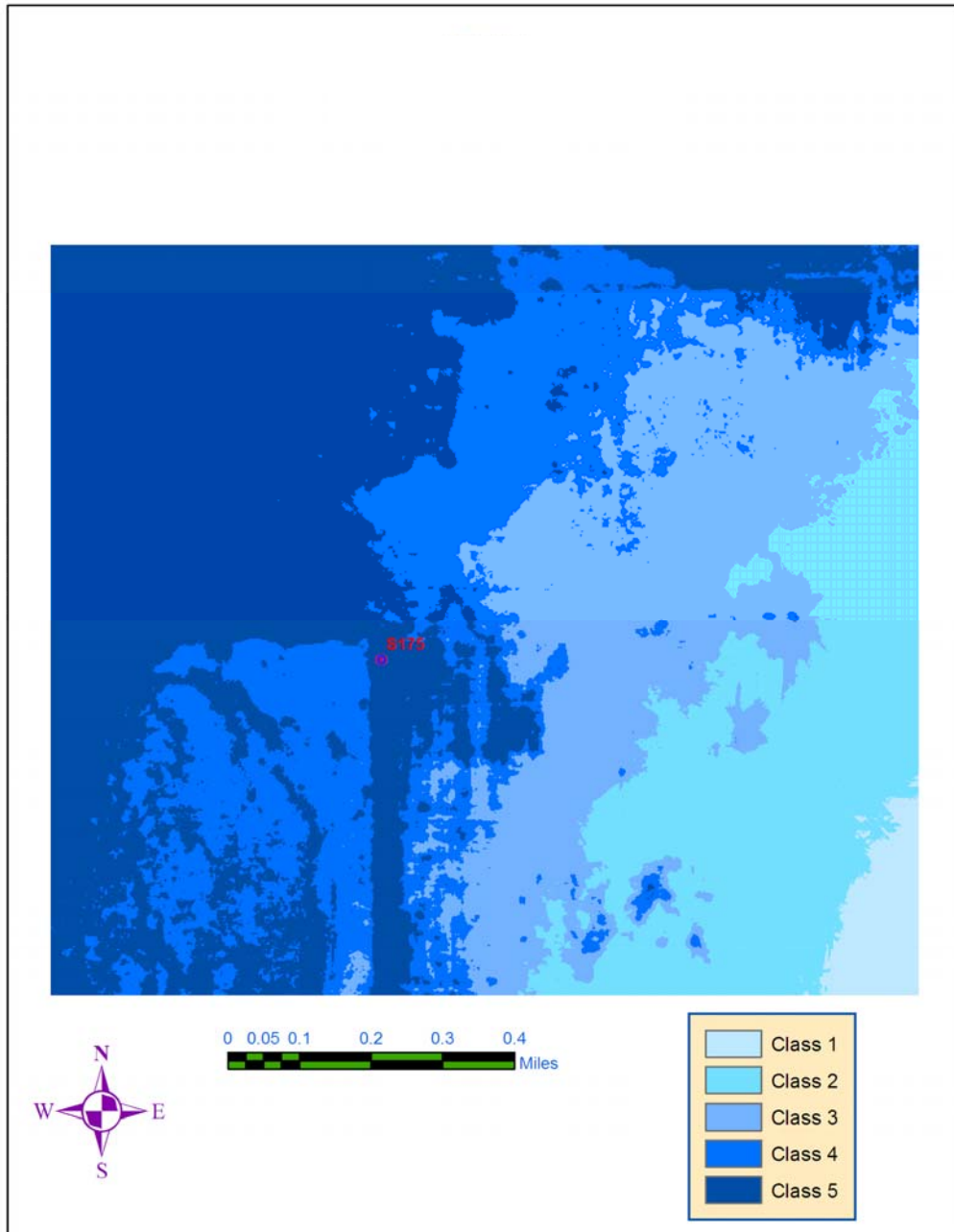


Figure 4.10

H

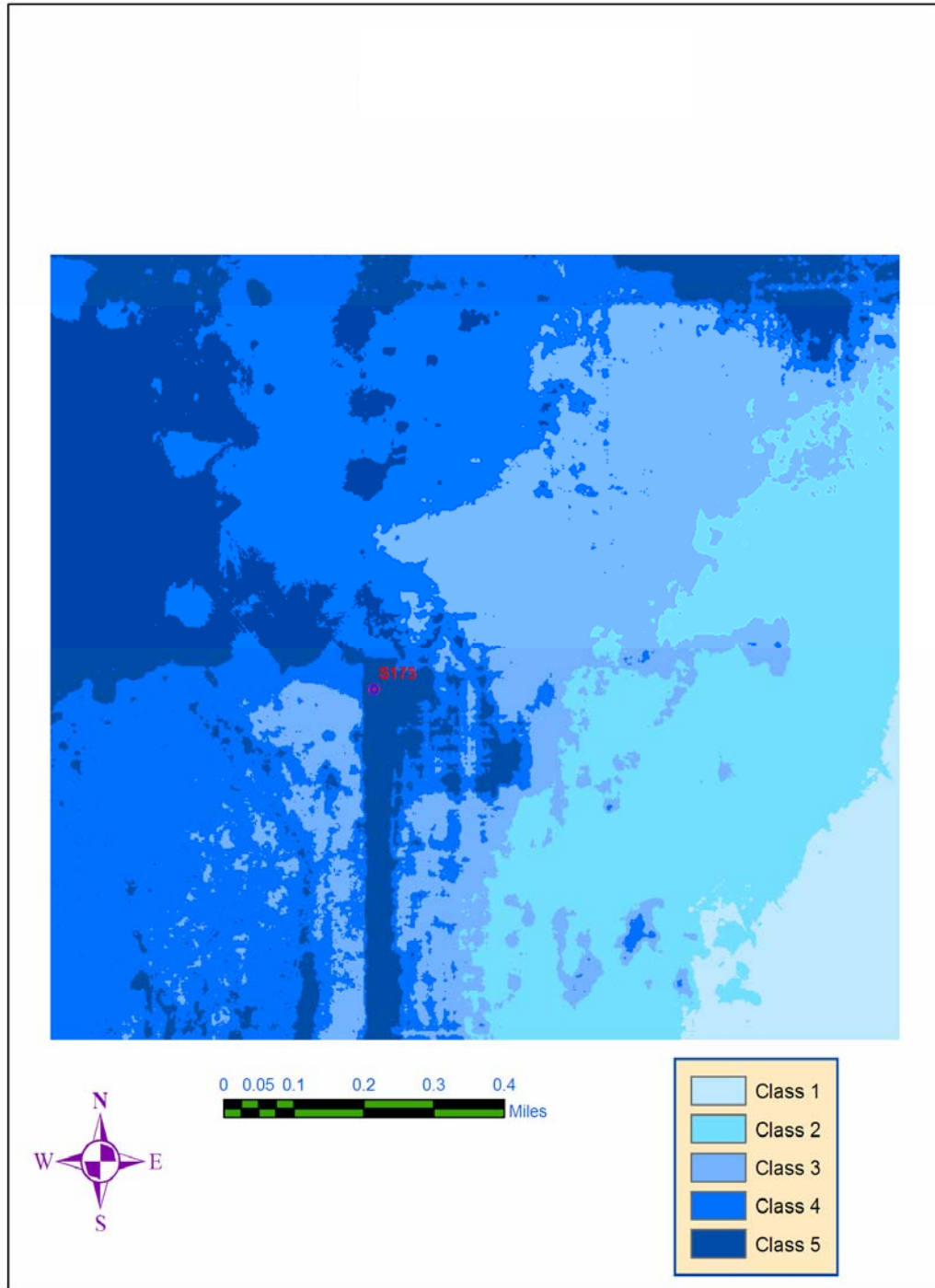


Figure 4.10

I

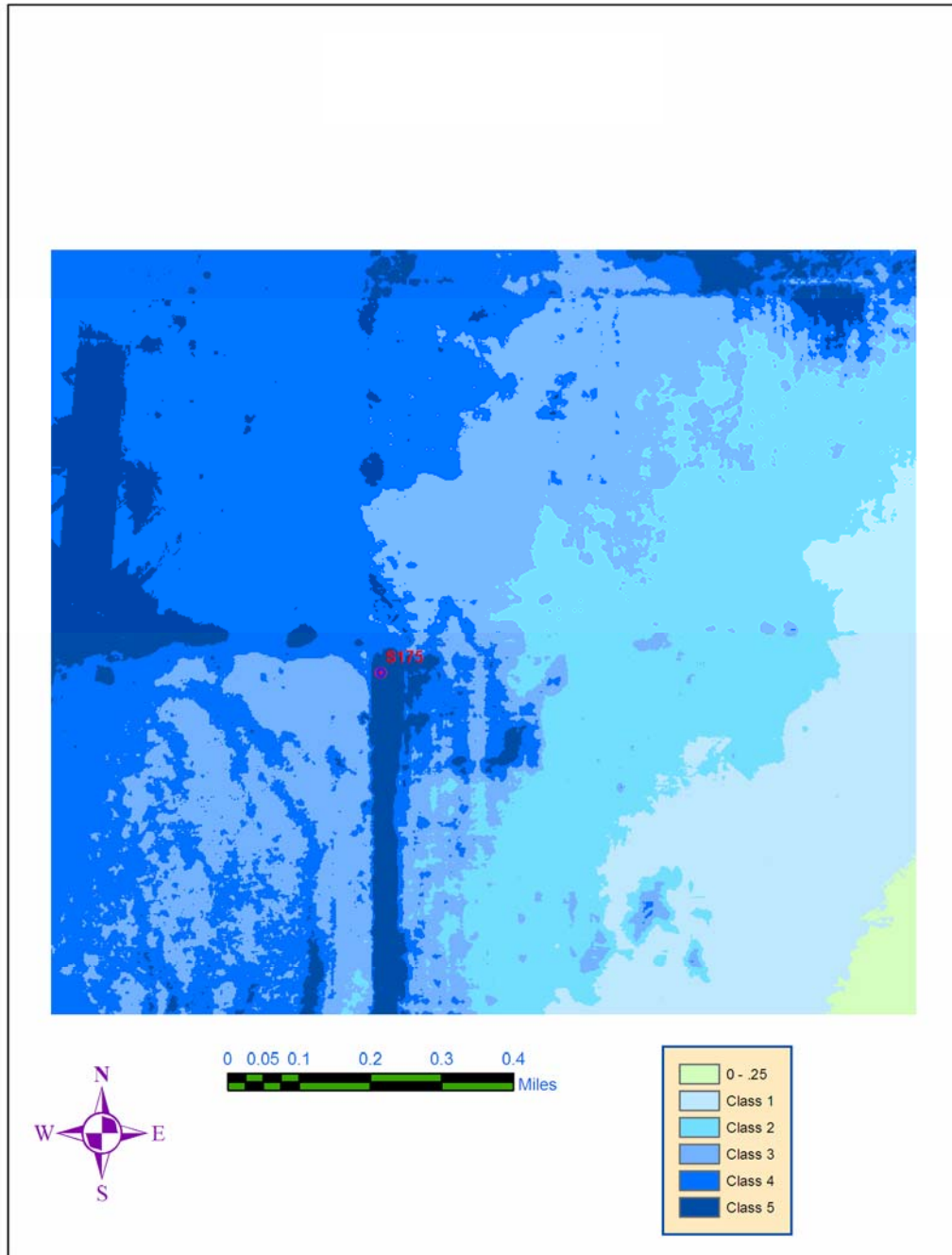


Figure 4.10

J

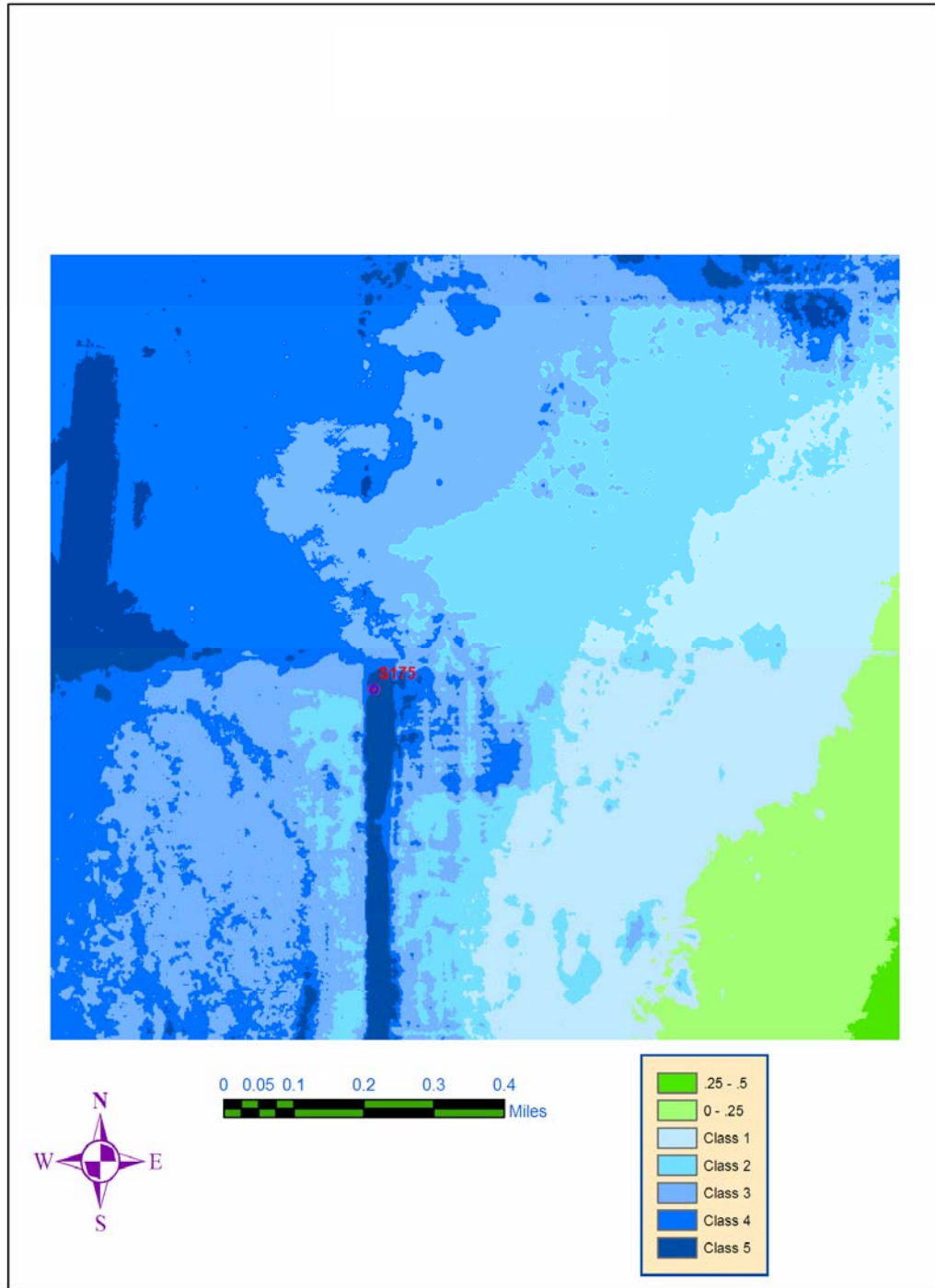


Figure 4.10

K

Table 4.1 Radial based functions statistics for topography.

Test Id	Mean Error	Root Mean Square Error
1	-0.000441	0.1352
2	-0.000826	0.1360
3	-0.000431	0.1351
4	-0.000415	0.1352
5	-0.000419	0.1352
6	-0.000451	0.1353
7	-0.000472	0.1352
8	-0.001378	0.1373
9	-0.001378	0.1373
10	-0.000451	0.1352
11	-0.000468	0.1353
12	-0.000409	0.1351
13	-0.000403	0.1351
14	-0.000464	0.1353
15	-0.000432	0.1351
16	-0.001378	0.1373
17	-0.000737	0.1374
18	-0.001111	0.1376
19	-0.001252	0.1384
20	-0.001165	0.1914

Table 4.2 Inverse distance weighting statistics for topography.

Test Id	Mean Error	Root Mean Square Error
1	-0.001844	0.141
2	-0.001688	0.1418
3	-0.002222	0.1395
4	-0.001682	0.1417
5	-0.001571	0.1443
6	-0.001563	0.1443
7	-0.002222	0.1395
8	-0.001694	0.1416
9	-0.001675	0.1418
10	-0.002222	0.1395
11	-0.001677	0.1417
12	-0.001695	0.1418
13	-0.001803	0.1427
14	-0.002136	0.1406
15	-0.002068	0.1405
16	-0.002074	0.1405

Continued Table 4.2.

Test Id	Mean Error	Root Mean Square Error
17	-0.002134	0.1408
18	-0.002132	0.1408
19	-0.002074	0.1405
20	-0.00207	0.1405
21	-0.002136	0.1406
22	-0.002136	0.1406
23	-0.002076	0.1404
24	-0.002071	0.1405
25	-0.002129	0.1408
26	-0.002134	0.1408
27	-0.002069	0.1405
28	-0.002079	0.1404
29	-0.002136	0.1406
30	-0.002136	0.1406
31	-0.002088	0.1405
32	-0.00207	0.1405
33	-0.002137	0.1408
34	-0.002134	0.1408
35	-0.002074	0.1405
36	-0.002071	0.1405
37	-0.002136	0.1406

Table 4.3 Global polynomial statistics for topography.

Global	Mean Error	Root Mean Square Error
2	6.22E-07	0.2234
2	1.07E-06	0.2161

Table 4.4 Local polynomial statistics for topography.

Test Id	Mean Error	Root Mean Square Error
1	0.0001813	0.1813
2	0.0001305	0.1665
3	0.0001559	0.1474
4	-0.0001782	0.1489
5	-0.000265	0.1507
6	0.0002789	0.1827
7	-0.0004779	0.1722
8	-0.0005851	0.1621
9	-0.0000333	0.1577
10	0.00007704	0.1610

Table 4.5 Kriging statistics for topography. ME is the mean error, RMSE is the root mean square error, MSE is the mean standardized error and RMSSE is the root mean square standard error.

Type	ME	RMSE	ASE	MSE	RMSSE
OK	0.0004726	0.1458000	0.2068000	0.0022880	0.7046000
SK	0.0003122	0.1433000	0.1637000	0.0020840	0.8732000
UK	0.0005407	0.1462000	0.1170000	0.0046110	1.2490000
DK	0.0024980	0.1439000	0.1524000	0.0165800	0.9417000

Table 4.6 Universal Kriging statistics for SWEM. ME is the mean error, RMSE is the root mean square error, MSE is the mean standardized error and RMSSE is the root mean square standard error.

Test Id	ME	RMSE	ASE	MSE	RMSSE
1	0.0316	0.6499	0.1377	0.0110	4.4710
2	0.0577	0.6723	0.1377	0.2104	4.6320
3	0.1904	0.6005	0.1742	0.9627	3.2320
4	0.0892	0.6624	0.1716	0.3053	3.5910
5	0.0422	0.6288	0.1727	0.0638	3.4250
6	0.0434	0.6308	0.1528	0.0747	3.8730
7	0.0560	0.6321	0.1528	0.1614	3.8830
8	0.0723	0.5466	0.1954	0.1525	2.4730
9	0.0944	0.4942	0.2202	0.2057	1.8820
10	0.1275	0.5013	0.2185	0.3262	1.9100
11	0.1399	0.4778	0.2505	0.3217	1.5530
12	0.1087	0.4709	0.3000	0.1902	1.2840
13	0.1085	0.4705	0.3516	0.1621	1.0950
14	0.1085	0.4705	0.4045	0.1409	0.9517
15	0.1084	0.4701	0.4560	0.1249	0.8438

Table 4.7 Universal kriging statistics for SWEM, 10/12-22/1999. ME is the mean error, RMSE is the root mean square error, MSE is the mean standardized error and RMSSE is the root mean square standard error.

Day	ME	RMSE	ASE	MSE	RMSSE	Regression
10/12	-0.0536	0.7424	0.6619	-0.0694700	1.1140	.206x + 2.224
10/13	-0.0549	0.7493	0.6699	-0.0710300	1.1130	.191x + 2.234
10/14	-0.0007	0.6126	0.5520	0.0006252	1.0740	.499x + 1.569
10/15	0.0601	0.6005	0.5183	0.0516000	1.0380	.624x + 1.427
10/16	0.1084	0.4701	0.4558	0.1250000	0.8442	.685x + 1.325
10/17	0.0891	0.3556	0.4208	0.0915000	0.7339	.732x + 1.127
10/18	0.0842	0.2994	0.4049	0.1014000	0.6990	.758x + 1.000
10/19	0.0647	0.3202	0.4267	0.0586000	0.7260	.760x + .955
10/20	0.0642	0.4841	0.4975	0.0554000	1.0070	.639x + 1.33
10/21	0.0625	0.5155	0.5231	0.0524000	1.0340	.642x + 1.273
10/22	0.0653	0.5153	0.5263	0.0631000	1.0610	.691x + 1.108

Table 4.8 Simple kriging statistics for SWEM, 10/12-22/1999. ME is the mean error, RMSE is the root mean square error, MSE is the mean standardized error and RMSSE is the root mean square standard error.

Test Id	ME	RMSE	ASE	MSE	RMSSE
1	0.23820	0.7930	0.89760	0.21760	0.80370
2	0.24260	0.7845	0.89620	0.22300	0.79450
3	0.24330	0.7878	0.89620	0.22370	0.79770
4	0.24220	0.7846	0.89610	0.22260	0.79460
5	0.23820	0.7930	0.89760	0.21760	0.80370
6	0.24260	0.7845	0.89620	0.22300	0.79450
7	0.24330	0.7878	0.89620	0.22370	0.79770
8	0.24220	0.7846	0.89610	0.22260	0.79460
9	0.23480	0.7932	0.89710	0.21350	0.80410
10	0.24230	0.7844	0.89620	0.22270	0.79440
11	0.24340	0.7879	0.89620	0.22370	0.79780
12	0.24200	0.7845	0.89610	0.22240	0.79460
13	0.23480	0.7932	0.89710	0.21350	0.80410
14	0.24210	0.7844	0.89620	0.22240	0.79440
15	0.24250	0.7885	0.89620	0.22270	0.79860
16	0.24200	0.7845	0.89610	0.22240	0.79460
17	0.23480	0.7932	0.89710	0.21350	0.80410
18	0.24230	0.7844	0.89620	0.22270	0.79440
19	0.24340	0.7879	0.89620	0.22370	0.79780
20	0.24190	0.7846	0.89610	0.22220	0.79470
21	0.23820	0.7930	0.89760	0.21760	0.80370
22	0.24250	0.7845	0.89620	0.22290	0.79450
23	0.24350	0.7878	0.89620	0.22390	0.79770
24	0.24210	0.7845	0.89610	0.22250	0.79450
25	0.23480	0.7932	0.89710	0.21350	0.80410
26	0.24230	0.7844	0.89620	0.22270	0.79440
27	0.24340	0.7879	0.89620	0.22370	0.79780
28	0.24200	0.7845	0.89610	0.22240	0.79460

Table 4.9 Ordinary kriging statistics for SWEM. ME is the mean error, RMSE is the root mean square error, MSE is the mean standardized error and RMSSE is the root mean square standard error.

Test Id	ME	RMSE	ASE	MSE	RMSSE
1	0.12450	0.4990	0.76020	0.09016	0.57330
2	0.11370	0.4765	0.75650	0.08454	0.51990
3	0.09540	0.4731	0.75680	0.05357	0.51600
4	0.09287	0.4758	0.75580	0.05081	0.52000
5	0.12450	0.4990	0.76020	0.09016	0.57330
6	0.11370	0.4765	0.75650	0.08454	0.51990

Table 4.9 Continued

Test Id	ME	RMSE	ASE	MSE	RMSSE
7	0.09540	0.4731	0.75680	0.05357	0.51600
8	0.09290	0.4758	0.75580	0.05088	0.51990
9	0.12450	0.4990	0.76020	0.09016	0.57330
10	0.11370	0.4765	0.75650	0.08454	0.51990
11	0.09540	0.4731	0.75680	0.05357	0.51600
12	0.09287	0.4758	0.75580	0.05081	0.52000
13	0.12620	0.4991	0.76000	0.09286	0.57350
14	0.13260	0.4763	0.74980	0.09687	0.51490
15	0.09444	0.4735	0.75680	0.05198	0.51720
16	0.11920	0.4793	0.74920	0.07421	0.52300
17	0.12620	0.4991	0.76000	0.09286	0.57350
18	0.13260	0.4763	0.74980	0.09687	0.51490
19	0.09444	0.4735	0.75680	0.05198	0.51720
20	0.11920	0.4793	0.74920	0.07421	0.52300
21	0.12620	0.4991	0.76000	0.09286	0.57350
22	0.13260	0.4763	0.74980	0.09687	0.51490
23	0.09444	0.4735	0.75680	0.05198	0.51720
24	0.11920	0.4793	0.74920	0.07421	0.52300
25	0.12450	0.4990	0.76020	0.09016	0.57330
26	0.09870	0.4745	0.75650	0.05988	0.52230
27	0.12990	0.4732	0.75000	0.09259	0.51050
28	0.11150	0.4735	0.74900	0.06382	0.51540
29	0.12450	0.4990	0.76020	0.09016	0.57330
30	0.11370	0.4765	0.75650	0.08454	0.51990
31	0.09540	0.4731	0.75680	0.05357	0.51600
32	0.09287	0.4758	0.75580	0.05081	0.52000
33	0.12450	0.4990	0.76020	0.09016	0.57330
34	0.11370	0.4765	0.75650	0.08454	0.51990
35	0.09540	0.4731	0.75680	0.05357	0.51600
36	0.09287	0.4758	0.75580	0.05081	0.52000
37	0.12450	0.4990	0.76020	0.09016	0.57330
38	0.11370	0.4765	0.75650	0.08454	0.51990
39	0.09540	0.4731	0.75680	0.05357	0.51600
40	0.09287	0.4758	0.75580	0.05081	0.52000
41	0.12450	0.4990	0.76020	0.09016	0.57330
42	0.11370	0.4765	0.75650	0.08454	0.51990
43	0.09540	0.4731	0.75680	0.05357	0.51600
44	0.09287	0.4758	0.75580	0.05081	0.52000
45	0.12620	0.4991	0.76000	0.09286	0.57350
46	0.14040	0.4795	0.74990	0.10870	0.52170
47	0.09004	0.4730	0.75620	0.04613	0.51630

Table 4.9 Continued

Test Id	ME	RMSE	ASE	MSE	RMSSE
48	0.11430	0.4790	0.7486	0.06760	0.52260
49	0.12620	0.4991	0.7600	0.09286	0.57350
50	0.14040	0.4795	0.7499	0.10870	0.52170
51	0.09004	0.4730	0.7562	0.04613	0.51630
52	0.11430	0.4790	0.7486	0.06760	0.52260

Table 4.10 Disjunctive Kriging statistics for SWEM. ME is the mean error, RMSE is the root mean square error, MSE is the mean standardized error and RMSSE is the root mean square standard error.

Test Id	ME	RMSE	ASE	MSE	RMSSE
1	0.31350	0.85500	0.59990	0.3775	1.15300
2	0.31330	0.85500	0.59990	0.3770	1.15300
3	0.29560	0.86910	0.60260	0.3436	1.17300
4	0.31280	0.85500	0.59990	0.3761	1.15300
5	0.31670	0.86340	0.60050	0.3798	1.16000
6	0.31670	0.86340	0.60050	0.3798	1.16000
7	0.31370	0.85500	0.59990	0.3778	1.15300
8	0.31350	0.85500	0.59990	0.3775	1.15300
9	0.31350	0.85500	0.59990	0.3775	1.15300
10	0.31370	0.85500	0.59990	0.3778	1.15300
11	0.31390	0.85500	0.59990	0.3781	1.15300
12	0.31350	0.85500	0.59990	0.3775	1.15300
13	0.28280	0.72070	0.59090	0.3065	0.92520
14	0.31280	0.85500	0.59990	0.3761	1.15300
15	0.29830	0.87000	0.60270	0.3487	1.17600
16	0.31050	0.84840	0.59980	0.3737	1.14500
17	0.30000	0.86820	0.60210	0.3521	1.17000
18	0.34190	0.87840	0.60600	0.4215	1.19300
19	0.29520	0.85940	0.60140	0.3466	1.16200
20	0.31370	0.85500	0.60000	0.3779	1.15300
21	0.30520	0.85440	0.60010	0.3643	1.15200
22	0.31370	0.85500	0.60000	0.3779	1.15300
23	0.31370	0.85500	0.60000	0.3779	1.15300
24	0.34220	0.87830	0.60600	0.4220	1.19200
25	0.30000	0.86820	0.60210	0.3521	1.17000
26	0.31270	0.85520	0.59990	0.3760	1.15300
27	0.31350	0.85500	0.59990	0.3775	1.15300
28	0.31280	0.85500	0.59990	0.3761	1.15300
29	0.29560	0.86910	0.60260	0.3436	1.17300

Table 4.10 Continued

Test Id	ME	RMSE	ASE	MSE	RMSSE
30	0.31330	0.85500	0.59990	0.3770	1.15300
31	0.31280	0.85500	0.59900	0.3761	1.15300
32	0.29520	0.85940	0.60140	0.3466	1.16200
33	0.31360	0.85510	0.59990	0.3776	1.15300
34	0.31370	0.85500	0.59990	0.3778	1.15300
35	0.29830	0.87000	0.60270	0.3487	1.17600
36	0.28970	0.85280	0.60040	0.3403	1.15400
37	0.31670	0.86340	0.60050	0.3798	1.16000
38	0.31050	0.84840	0.59980	0.3737	1.14500
39	0.30000	0.86820	0.60210	0.3521	1.17000
40	0.31270	0.85520	0.59990	0.3760	1.15300
41	0.31350	0.85500	0.59990	0.3775	1.15300
42	0.31280	0.85500	0.59990	0.3761	1.15300
43	0.29830	0.87000	0.60270	0.3487	1.17600
44	0.28970	0.85280	0.60040	0.3403	1.15400
45	0.31670	0.86340	0.60050	0.3798	1.16000
46	0.31050	0.84840	0.59980	0.3737	1.14500
47	0.31280	0.85500	0.59990	0.3761	1.15300
48	0.31350	0.85500	0.59900	0.3775	1.15300
49	0.31270	0.85520	0.59990	0.3760	1.15300
50	0.30000	0.86820	0.60210	0.3521	1.17000

Table 4.11 SWEM surface water values for October 12-22, 1999. Elevation values are in feet NGVD 88 and ST is the station description.

ST	12	13	14	15	16	17	18	19	20	21	22
S178	1.44	1.41	1.24	1.39	1.65	1.91	2.08	1.93	1.75	1.58	1.44
NP158	2.79	2.75	2.97	3.71	3.96	3.98	3.96	3.89	3.81	3.73	3.68
S175	2.43	2.40	2.60	3.68	4.30	4.22	4.11	3.98	3.85	3.73	3.62
S178	1.44	1.41	1.24	1.39	1.65	1.91	2.08	1.93	1.75	1.58	1.44
NP158	2.79	2.75	2.97	3.71	3.96	3.98	3.96	3.89	3.81	3.73	3.68
S175	2.43	2.40	2.60	3.68	4.30	4.22	4.11	3.98	3.85	3.73	3.62
FP1	3.29	3.22	3.41	3.99	4.19	4.19	4.19	4.19	4.19	4.19	4.17
FP2	2.39	2.33	2.86	4.13	4.43	4.43	4.39	4.29	4.08	3.87	3.70
S332	3.90	3.90	3.96	4.47	4.81	4.80	4.73	4.65	4.57	4.51	4.43
NP112	3.95	3.94	4.03	5.10	4.75	4.64	4.57	4.50	3.84	3.80	3.85
S177	1.61	1.60	1.86	3.26	3.53	3.34	3.10	2.88	2.67	2.48	2.31
FP	2.84	2.77	3.27	4.19	4.64	4.61	4.53	4.42	4.32	4.23	4.14
G3355	2.49	2.46	2.44	2.42	2.31	2.25	2.16	2.09	2.01	1.93	1.85

Table 4.12 Vulnerability index classes used for SWIM. Classes 1-5 represent the increase in inundation magnitude.

Class	Inundation Depth Interval in Feet
1	0.0 - 0.25
2	0.25 - 0.5
3	0.5 - 0.75
4	0.75 - 1.0
5	1.0 & Greater

Table 4.13 Calculated inundation statistics for the study area.

Day	2D Area ft. <sup>2</sup>	Surface Area ft. <sup>2</sup>	Volume	$\Delta$ Area ft. <sup>2</sup>	$\Delta$ Volume ft. <sup>3</sup>	$\Delta$ Volume %
12	1797974.14	1797975.00	42193.36	0.86	0.00	0.00%
13	1384624.66	1384625.48	37114.63	0.82	-5078.73	-12.04%
14	4746567.06	4746568.03	80282.80	0.97	43168.17	116.31%
15	36122841.00	36122843.49	2268912.29	2.49	2188629.49	2726.15%
16	36122841.00	36122843.49	4175404.91	2.49	1906492.62	84.03%
17	36122841.00	36122843.49	3916325.23	2.49	-259079.68	-6.20%
18	36122841.00	36122843.50	3523287.65	2.50	-393037.58	-10.04%
19	36122841.00	36122843.50	3062008.15	2.50	-461279.50	-13.09%
20	36122841.00	36122843.49	2653239.40	2.49	-408768.75	-13.35%
21	35687948.23	35687950.73	2269041.32	2.50	-384198.08	-14.48%
22	32926192.31	32926194.80	1895679.52	2.49	-373361.80	-16.45%

## CHAPTER 5 CONCLUSION

The objective of this research was to develop flood maps that use ALSM, Landsat 7 ETM+ and regional surface water elevation data. The combination of these data sources proved to be successful for mapping water produced by Hurricane Irene. Low elevation areas were found to be the most vulnerable to flooding, because of their high inundation magnitude and duration of flooding.

### **Image Analysis**

Landsat7 ETM+ was effective for mapping the flood impact of Hurricane Irene, and detecting dense clouds. NDVI was determined to be useful for mapping water for October 16, 1999, and April 9, 2000, Landsat 7 ETM+ scenes. Although unsupervised classified NDVI maps were useful for mapping water, several constraints were observed after the mapping process. Vegetation canopy and clouds were found to prevent the detection of water, and second, the 30 meter resolution was too coarse to detect water at a high resolution. The presence of excess water after Hurricane Irene produced more NDVI water classes than were observed with the April 9, 2000, NDVI map. Because of this condition, classes 1 and 2 in both NDVI maps were determined to be pure open water and severely inundated. It is important to note that this does not mean that higher NDVI class pixels were not flooded.

### **Bare Earth Modeling**

Bare earth topographic modeling was dependent on detecting vegetation patterns visible with color infrared images. The maximum elevation threshold filter used to

remove vegetation and artifact points was effective; however gaps in the NAD 83 DEM produced an increase in uncertainty for interpolated surfaces. The radial based function interpolator produced the lowest root mean square value and was used to create topographic grids. Topographic grids displayed a flat and low elevation surface that is characteristic of the C-111's topography.

### **SWEM**

The surface water elevation map was useful for displaying the change in surface water elevation before and after Hurricane Irene, and universal kriging was judged to be the best interpolator for surface water elevation grids. The maximum surface water elevation value for the S175 culvert occurred on October 16, 1999, and a gradual decrease in elevation was observed for the period following Hurricane Irene. SWEM maximum surface water values match reports from the SFWMD.

### **SWIM**

SWIM was shown to be successful for displaying a severe inundation condition produced by Hurricane Irene. SWIM may also be used to predict flooding for agricultural, environmental and urban areas inside the flight area. Agricultural operation managers in the C-111 and Frog Pond may use SWIM to predict areas that may experience the greatest damage, and water managers may also determine which areas would required the greatest flood protection. For example, if an area near a water control structure shows severe inundation, then managers may decide to increase the pumping or drainage capacity of that structure. Any flood assessment performed by FEMA requires the ability to accurately map the most vulnerable areas, and the project methodology provided a suitable guide for determining these areas in the C-111 Basin. The method for GIS flood mapping may also be expanded to include other ALSM areas sponsored by

FEMA; however these areas may not include satellite imagery that covers a specific event.

### **Conclusion**

To conclude, the evolution of 3D flood mapping depends on the ability to integrate and interpret multiple remotely sensed data; however combining elevation data from different vertical and horizontal datums is not recommended. Ideally, all elevation data should be in NAD 83 and NGVD 88, and any conversion to NAD 27 and NGVD 29 is dependent on the conversion of first order benchmarks by the National Geodetic Survey. The conversion value for vertical datums was 1.5125 ft.; however NAD 83 and NGVD 88 are measured differently than NAD 27 and NGVD 88, and no relationship exists between these sets of datums. Converting ALSM elevation data to NAD 27 and NGVD 29 for the purpose of matching surface water elevation data may reduce the accuracy of ALSM data. Additionally, the latitudinal and longitudinal coordinates of surface water sites in the study area were not measured with the same degree of accuracy as the ALSM data. ALSM clients should consider only using NAD 83 and NGVD 88 datums, because they are the only datums used for reference during ALSM data capture.

## CHAPTER 6 RECOMMENDATIONS FOR FUTURE STUDIES

SWIM and NDVI maps were shown to be useful for flood detection; however the study area consists of only a small portion of the ALSM flight area. For a complete flood analysis, SWIM and NDVI maps should be made of the entire flight area.

Combining the C-111 ALSM data with other Miami-Dade ALSM data will contribute to developing a comprehensive high resolution topographic DEM of Miami-Dade and eventually, all of south Florida. It is important to note that NAD 83 and NGVD 88 datums should only be used for 3D mapping since they are global datums derived from Differential Global Positioning Systems (DGPS).

SWIM methodology may be applied to ALSM coastal data sets acquired during 2001; however surface water data for all SFWMD, USGS and NPS hydrologic monitoring sites should be reviewed. The procedure for assimilating surface water data must consider anomalies that do not represent accurate surface water elevation values. For example, Robblee well was excluded, because it possessed surface water elevation measurements far below the expected range of values. Additionally, surface water site locations should be surveyed with DGPS to improve horizontal and vertical accuracy with NAD 83 and NGVD 88 datums. Integrating Synthetic Aperture Radar (SAR) with ALSM would assist in distinguishing water from soil. Furthermore, this will improve separating trees with water and trees over dry land, and crops from trees.

Future applications of SWIM for the flight area will require an improvement of bare earth models for other types of land cover. The bare earth procedure should involve

point removal and spatial modeling with multiple interpolators; however a more variable surface should be expected for the entire flight area.

The introduction of precipitation data will assist in the creation of high resolution water budgets. Precipitation values are provided by the SFWMD, USGS and NPS, and spatial modeling of precipitation will provide insight into the distribution of precipitation for Hurricane Irene. NEXRAD radar precipitation images measure hourly rainfall, and images are available for Hurricane Irene and other severe rain events. The primary limitation of NEXRAD is its coarse resolution and no definable coordinates are provided for GIS mapping applications.

Future efforts should investigate other methods of interpolation which may include inverse distance weighting, local and global functions, kriging and cokriging. Maximum surface water values for October 16, 1999, would be useful for cokriging because of the smooth surface that conforms to topographic relief. A variety of search parameters should be used to improve topographic and surface water prediction grids. Finally, all metadata for each processed geo-spatial data set must be carefully reviewed to verify the accuracy of listed datums and projections.

## LIST OF REFERENCES

- Adams, J.C. and J.H. Chandler. 2002. Evaluation of LIDAR and Medium Scale Photogrammetry for Detecting Soft-Cliff Coastal Change. *Photogrammetric Record* 1799: 405-18.
- Ball, M.H., R.W. Schaffranek. 2000. Interrelation of Everglades Hydrology and Florida Bay Dynamics to Ecosystem Processes and Restoration in South Florida: Regional Simulation of Inundation Patterns in the South Florida Everglades. Naples, FL: United States Geological Survey.
- Ball, M.H., R.W. Schaffranek. 2000. Water Surface Elevation and Water Depth Analyses Using a GIS Application. Naples, FL: United States Geological Survey,
- Brock, J.C., A.H. Sallenger, W.B. Krabill, R.N. Swift, C.W. Wright. 2001. Recognition of Fiducial Surfaces in Lidar Surveys of Coastal Topography. *Photogrammetric Engineering and Remote Sensing* 68: 1245-58.
- Bethel, J.L., W.F. Cheng. 1995. *The Civil Engineering Users Manual*. Boca Raton, FL: CRC Press.
- Daniels, R.C. 2000. Datum Conversion Issues with Lidar Spot Elevation Data. *Photogrammetric Engineering and Remote Sensing* 67: 735-40.
- Doren, R.F., K. Rutchey, R. Welch. 1998. The Everglades: A Perspective on the Requirements and Applications for Vegetation Map and Database Products. *Photogrammetric Engineering and Remote Sensing* 65: 155-61.
- Douchette, P., K. Beard. 1999. Exploring the Capability of Some GIS Surface Interpolators for DEM Gap Fill. *Photogrammetric Engineering and Remote Sensing* 66: 881-87.
- ESRI. 2001. *ArcGIS Geostatistical Analyst: Statistical Tools for Data Exploration, Modeling and Advanced Surface Generation*. Redlands, CA: ESRI.
- Evans, D.L., S.D. Roberts, J.W. McCombs, R.L. Harrington. 2000. Detection of Regularly Spaced Targets in Small Footprint LIDAR Data: Research Issues for Considerations. *Photogrammetric Engineering and Remote Sensing* 67: 1133-36.
- Fetter, C.W. 1998. *Applied Hydrogeology*. Oshkosh: University of Wisconsin.

Frazier, P.S., K.J. Page. 1999. Water Body Detection and Delineation with Landsat TM Data. *Photogrammetric Engineering and Remote Sensing* 66: 1461-67.

Graham, W.D., K.L. Campbell, J. Mossa, L.H. Motz, P.S.C. Rao, W.R. Wise. 1997. Water Management Issues Affecting the C-111 Basin, Dade County, Florida: Hydrologic Sciences Task Force Initial Assessment Report. Gainesville, FL: University of Florida.

Harris County Flood District. April 2006. <[www.hcfd.org/fsarp.asp](http://www.hcfd.org/fsarp.asp)>

Heinzer, T., Michael Sebat, Bruce Feinberg, Dale Kerper. 2002. The Use of GIS to Manage LIDAR Elevation Data and Facilitate Integration with the MIKE21 2-D Hydraulic Model in a Flood Inundation Decision Support System. April 2006. <<http://gis.esri.com/library/userconf/proc00/profesional/papers/PAP675/p675.htm>>

Hodgson, M.E., J.R. Jensen, J.A. Tullis, K.D. Riordan, C.M. Archer. 2003. Synergistic Use of Lidar and Color Aerial Photography for Mapping Urban Parcel Imperviousness. *Photogrammetric Engineering and Remote Sensing* 69: 973-980.

Hodgson, M.E., P. Bresnahan. 2004. Accuracy of Airborne Lidar Derived Elevation: Empirical Assessment and Error Budget. *Photogrammetric Engineering and Remote Sensing* 70: 331-339.

Hopkinson, C., M. Sitar, L. Chasmer, P. Treitz. 2003. Mapping Snowpack Depth Beneath Forest Canopies Using Airborne Lidar. *Photogrammetric Engineering and Remote Sensing* 70: 323-330.

Huising, E.J., L.M. Gomes Pereira. 1998. Errors and Accuracy Estimates of Laser Data Acquired by Various Laser Scanning Systems for Topographic Applications. *International Society of Photogrammetric Engineering and Remote Sensing* 53: 245-261.

Kampa, K., K.C. Slatton, 2004. An Adaptive Multiscale Filter for Segmenting Vegetation in ALSM Data. Gainesville, FL: University of Florida, Department of Civil and Coastal Engineering and Department of Computer Science Engineering.

Krabill, W.B., C.W. Wright, R.N. Swift, E.B. Fredrick, S.S. Manizade, J.K. Yungei, C.F. Martin, J.G. Sonntag, M. Duffy, W. Hulslander, J.C. Brock. 1999. Airborne Laser Mapping of Assateague National Seashore Beach. *Photogrammetric Engineering and Remote Sensing* 66: 65-71.

Kraus, K., N. Pfeifer. 1998. Determination of Terrain Models in Wooded Areas with Airborne Laser Scanner Data. *International Society of Photogrammetric Engineering and Remote Sensing* 53: 193-203.

Lowe, A.S., 2002. The Federal Emergency Management Agency's Multi-Hazard Flood Map Modernization and The National Map. *Photogrammetric Engineering and Remote Sensing* 69: 1133-35.

- Lunetta, R.S., M.E. Balogh. 1998. Application of Multi-Temporal Landsat 5 TM Imagery for Wetland Identification. *Photogrammetric Engineering and Remote Sensing* 65: 1303-10.
- Lyon, J.G., D Yuan, R.S. Lunetta, C.D. Elvidge. 1997. A Change Detection Experiment Using Vegetation Indices. *Photogrammetric Engineering and Remote Sensing* 64: 143-50.
- Madden, M., K. Marguerite, D. Jones, L. Vilchek. 1998. Photointerpretation Key for the Everglades Vegetation Classification System. *Photogrammetric Engineering and Remote Sensing* 65: 171-77.
- Maune, D.M. 2001. *The DEM Users Manual: Digital Elevation Model and Technology and Applications*. Arlington, VA: American Society of Photogrammetry and Remote Sensing.
- Melesse, A.M., J.D. Jordan. 2003. Spatially Distributed Watershed Mapping and Modeling: Thermal Maps and Vegetation Indices to Enhance Land Cover and Surface Microclimate Mapping: Part 1. *Journal of Spatial Hydrology* 3: 1-29.
- Okagawa, M. 2001. Algorithm of Multiple Filter to Extract DSM from LIDAR data. 2001. Presentation at ESRI International User Conference. 23-25 July. San Diego, California.
- Persson, A., J. Holmgren, U. Soderman. 2001. Detecting and Measuring Individual Trees Using an Airborne Laser Scanner. *Photogrammetric Engineering and Remote Sensing* 68: 925-32.
- Peters, A.J., E.A. Walter-Shea, L. Ji, A. Vina, M. Hayes, M.D. Svoboda. 2001. Drought Monitoring with NDVI-Based Standardized Vegetation Index. *Photogrammetric Engineering and Remote Sensing* 68: 71-5.
- Popescu, S.C., and R.H. Wynne. 2004. Seeing the trees in the forest: Using Lidar and Multispectral Data Fusion with Local Filtering and Variable Window Size for Estimating Tree Height. *Photogrammetric Engineering and Remote Sensing* 71: 589-604.
- Popescu, S.C., R.H. Wynne, and J.A. Scrivani. 2004. Fusion of Small-footprint Lidar and Multispectral Data to Estimate Plot-level Volume and Biomass in Deciduous and Pine Forests in Virginia, USA. *Forestry Science* 50: 551-65.
- Raber, G.T., J.R. Jensen, S.R. Schill, K. Schuckman. 2002. Creation of Digital Terrain Models Using an Adaptive Lidar Vegetation Point Removal Process. *Photogrammetric Engineering and Remote Sensing* 69: 1307-1315.
- Sheng, Y., Y. Su, Q. Xiao. 1998. Challenging the Cloud Contamination Problem in Flood Monitoring with NOAA/AVHRR Imagery. *Photogrammetric Engineering and Remote Sensing* 65: 191-98.

- Song, J., L. Duanjun, M.L. Wesely. 2002. A Simplified Atmospheric Correction Procedure for the Normalized Differential Vegetation Index. *Photogrammetric Engineering and Remote Sensing* 69: 521-528.
- Sorin, C.P., H.W. Randolph. 2003. Seeing the Trees in the Forest: Using Lidar and Multispectral Data Fusion with Local Filtering and Variable Window Size for Estimating Tree Height. *Photogrammetric Engineering and Remote Sensing* 70: 589-604.
- South Florida Water Management District. 2000. After Irene Assessment. West Palm Beach: South Florida Water Management District.
- Stow, D., L. Coulter, J. Kaiser, A. Hope, D. Service, K. Schutte, A. Walters. 2002. Irrigated Vegetation Assessment for Urban Environments. *Photogrammetric Engineering and Remote Sensing* 69: 381-390.
- Todd, S., R.M. Hoffer. 1997. Responses of Spectral Indices to Variations in Vegetation Cover and Soil Background. *Photogrammetric Engineering and Remote Sensing* 64: 915-21.
- United States Geological Survey. April 2006. <[www.usgs.gov](http://www.usgs.gov)>
- Welch, R., M. Madden, R.F. Doren. 1998. Mapping the Everglades. *Photogrammetric Engineering and Remote Sensing* 65: 163-170.
- Yodoyama, R., M. Shirasawa, R.J. Pike. 2001. Visualizing Topography by Openess: A New Application of Image Processing to Digital Elevation Models. *Photogrammetric Engineering and Remote Sensing* 68: 257-265.

## BIOGRAPHICAL SKETCH

William Webb is the son of Brenda Y. Webb and Frank R. Webb, and is the brother of Ron Webb, Ashleigh Webb and Hiliary Webb. The author graduated from the University of Florida in May 1999 with a bachelor's degree in Agricultural Operations Management. The author has completed the Hydrologic Sciences Academic Cluster and Remote Sensing and Geographic Information Systems Curriculum certificates.